

Doctoral Dissertations and Master's Theses

---

Spring 2024

## Mitigating Engine Unstart in Scramjets with Porous Bleeders

Ryan Lindley

Embry-Riddle Aeronautical University, lindler2@my.erau.edu

Follow this and additional works at: <https://commons.erau.edu/edt>



Part of the [Aerodynamics and Fluid Mechanics Commons](#), [Aeronautical Vehicles Commons](#), and the [Propulsion and Power Commons](#)

---

### Scholarly Commons Citation

Lindley, Ryan, "Mitigating Engine Unstart in Scramjets with Porous Bleeders" (2024). *Doctoral Dissertations and Master's Theses*. 813.

<https://commons.erau.edu/edt/813>

This Thesis - Open Access is brought to you for free and open access by Scholarly Commons. It has been accepted for inclusion in Doctoral Dissertations and Master's Theses by an authorized administrator of Scholarly Commons. For more information, please contact [commons@erau.edu](mailto:commons@erau.edu).

By

A Thesis Submitted to the Faculty of Embry-Riddle Aeronautical University

In Partial Fulfillment of the Requirements for the Degree of

Master of Science in Aerospace Engineering

Embry-Riddle Aeronautical University

Daytona Beach, Florida

By

THESIS COMMITTEE

---

---

---

Graduate Program Coordinator,  
Dr. Hever Moncayo

---

Date

---

Dean of the College of Engineering,  
Dr. James W. Gregory

---

Date

---

Associate Provost of Academic Support,  
Dr. Kelly Austin

---

Date

*To Kyle & Preston  
Maybe you'll find this interesting*

## **ACKNOWLEDGEMENTS**

I would like to extend my sincere thanks and gratitude to my advisor, Dr. Scott Martin, for the opportunity to conduct this research and for the support and immeasurable help provided to me throughout this process. I would also like to extend my gratitude to my thesis committee members, Dr. William Engblom and Dr. Eric Perrell, for providing me with the aid and resources to complete this research. I would like to thank my academic peers, Jacob Snider and Arjun Vedam for inspiring this research, as well as my personal peers, Paul Bayer for helping me start, and Cooper Davis for helping me finish.

Last, but not least, I would like to thank CDR Lance R Lindley for his support, and for funding everything for two decades leading up to this thesis, as well as Sachiko Matsuda Lindley, for never letting me settle for what I would deem less than as perfect as possible.

## **ABSTRACT**

Engine unstart, a critical issue in hypersonic propulsion, occurs when the airflow in the engine's inlet system abruptly stalls or reverses direction. This phenomenon disrupts combustion, leading to loss of thrust and potentially catastrophic failure. Unstart is particularly problematic in hypersonic flows due to the extreme aerodynamic conditions involved, where even minor disturbances can trigger destabilizing effects. Managing unstart is thus vital for ensuring the reliability and safety of hypersonic propulsion systems.

In this study, the effectiveness of porous bleeders in mitigating unstart phenomena and enhancing isolator effectiveness in a hypersonic scramjet was investigated. Through computational fluid dynamics simulations, the impact of porous bleeder design parameters such as pressure jump coefficient and bleeder size on isolator effectiveness and unstart prevention was evaluated. Results indicated that porous bleeders delayed flow separation and reduced adverse pressure gradients, thereby enhancing isolator performance. Additionally, porous bleeders demonstrated promising capabilities in preventing full unstart events and mitigating oscillatory unstart phenomena.

# TABLE OF CONTENTS

<b>ACKNOWLEDGEMENTS</b> .....	i
<b>ABSTRACT</b> .....	ii
<b>TABLE OF CONTENTS</b> .....	iii
<b>LIST OF FIGURES</b> .....	v
<b>LIST OF TABLES</b> .....	x
<b>1 Introduction</b> .....	1
1.1 What is a Scramjet.....	1
1.2 Why Scramjets .....	2
1.3 Scramjet Obstacles .....	5
1.4 Preventing Unstart.....	6
<b>2 Background &amp; Literature Review</b> .....	7
2.1 The Scramjet Design .....	7
2.2 The Unstart Phenomenon .....	11
2.3 The X-43A.....	21
2.4 The Porous Bleeder .....	26
2.5 The Objective .....	27
<b>3 Methodology &amp; Foundational Setup</b> .....	29
3.1 Base Structured Mesh Creation.....	29
3.2 Converge CFD Software .....	41

3.3 Improved Unstructured Mesh Creation.....	45
3.4 Ideal Lower Cowl Locations.....	52
<b>4 Porous Bleeder Implementation Results &amp; Discussion.....</b>	<b>56</b>
4.1 Porous Modeling.....	56
4.2 Isolator Airflow Examination.....	62
4.3 Porous Effectiveness Measurement.....	66
4.4 Unstart Prevention.....	73
<b>5 Conclusions and Recommendations.....</b>	<b>84</b>
<b>REFERENCES.....</b>	<b>86</b>
APPENDIX A – Additional Porous Bleed Cases.....	90
APPENDIX B – Porous Isolator Efficiency Derivation.....	94

## LIST OF FIGURES

Figure.....	Page
Figure 1.1 The J58 engine used for the SR-71, with its large bypass tubes visible [3].....	2
Figure 1.2 Rocket engines, although powerful, greatly fall behind air-breathing engines in terms of efficiency [4].....	3
Figure 1.3 Diagram showcasing flight trajectories of various vehicles. Hypersonic air-breathing scramjets could reach low Earth orbit while keeping the efficiency of air-breathing engines [5].	4
Figure 2.1 Sideview of a scramjet engine showing the (1) Inlet, (2) Isolator, (3) Combustor, and (4) Exhaust [4].	8
Figure 2.2 An isolator in (a) Scramjet mode, (b) Ramjet mode, and (c) Unstarted mode [5].	9
Figure 2.3 A diagram depicting a cavity flameholder design [7].	10
Figure 2.4 Dual-mode ramjet/scramjets are designs in which the combustor is capable of igniting fuel in both subsonic and supersonic incoming airflow [12].	10
Figure 2.5 (Left) A functioning inlet can compress incoming air. (Right) A supersonic unstarted inlet creating a normal shock and preventing any airflow into the engine. Results from the present work.	12
Figure 2.6 In a stable case, after the air-throttling is turned off, the blue dashed line measuring the pressure ratio at the inlet returns to close to 1 [14].	14
Figure 2.7 In an unstarted case, the blue dashed line representing the inlet pressure ratio does not return to close to 1 after air-throttling is turned off, as the inlet has unstarted and a high-pressure region has formed [14].	15
Figure 2.8 A mechanical throat can be employed to arbitrarily increase back pressure without the need for ignition or combustion modeling [12].	16
Figure 2.9 A more refined grid can capture an unstart where a coarser grid may fail to [15].	18
Figure 2.10 A sufficient amount of grid refinement is required to properly measure the amount of total pressure recovery [15].	19
Figure 2.11 Many flow features would not be properly captured without sufficient grid refinement [15].	20
Figure 2.12 The X-43A was a 12 foot long wedge-shaped hypersonic scramjet [4].	21
Figure 2.13 A modified Pegasus rocket booster was used to accelerate the X-43A after separation from the B-52 [16].	21

Figure 2.14 The Pegasus rocket booster carrying the X-43A separates from NASA's B-52B [11]. .....	22
Figure 2.15 Dimensions of the X-43A [4]. .....	23
Figure 2.16 Schematics of the design based on the X-43A geometry tested in the HAST facility [27]. .....	24
<i>Figure 2.17</i> A picture of the HAST facility used for Kotov et al.'s study [28]. .....	25
Figure 2.18 Shadow picture combination of all parts of the inlet model [27]. .....	25
Figure 2.19 Shadow picture of flow entering the isolator [27]. .....	26
Figure 3.1 The provided schematics were used in tandem with the overall dimensions to create a scaled to size mesh. ....	30
Figure 3.2 The structured mesh at the front of the X-43. The mesh becomes very dense near the wall surfaces. ....	30
Figure 3.3 Mach contour results at 0 degrees angle of attack for the Coarse (top), Fine (middle), and Very Fine (bottom) grid resolutions. ....	33
Figure 3.4 Mesh in front of the lower cowl at Coarse (top), Fine (middle), and Very Fine (bottom) grid resolutions. The effects of the grid adaptation are clearly visible. ....	35
Figure 3.5 Mach contour in the isolator for 0-8 degrees (top to bottom) angle of attack. ....	36
Figure 3.6 Static pressure distribution (in Pascals) on the lower isolator wall at 0 degrees angle of attack for all refinement cases. ....	37
Figure 3.7 Lower wall static pressure (in Pascals) for 2 (top-left), 4 (top-right), 6 (bottom-left), and 8 (bottom-right) degrees angle of attack. ....	38
Figure 3.8 Static pressure distribution (in Pascals) on the upper isolator wall at 0 degrees angle of attack for all refinement cases. ....	39
Figure 3.9 The mass flow rate through the isolator increases linearly with angle of attack. The MFR readings for all grid refinement cases are plotted but perfectly overlap each other. ....	40
Figure 3.10 Wall $y^+$ values for the lower (left) and upper (right) wall surfaces. ....	41
Figure 3.11 Converge CFD automatically generates a mesh and adapts it during runtime according to given instructions. Here, the many cells created near the wall to achieve a $y^+$ of one are visible. ....	42
Figure 3.12 While proper expansion is visible, this case does not have flow separation and the associated subsonic vortex. ....	43

Figure 3.13 Introducing viscous equations reintroduces flow separation but increases freestream temperature, lowering the freestream Mach number. Improperly formed oblique shocks are also visible.....	44
Figure 3.14 A closeup of the isolator section; the expansion fan is not properly formed at the top of the isolator, and the improperly formed oblique shocks have reached the lower cowl much farther forward than anticipated.....	44
Figure 3.15 Flow separation has occurred much earlier in this case and the bow shock has now moved so far forward that it missed the lower cowl entirely.....	45
Figure 3.16 Comparison between new (top) and old (bottom) Mach contours at 0 degrees angle of attack and fine refinement level.....	47
Figure 3.17 Unstructured mesh comparison in the isolator region for the Coarse (top), Fine (middle), and Very Fine (bottom) refinement levels. The very fine mesh did not introduce new cells in different locations; rather, it significantly increased the density of existing refined cells. ....	48
Figure 3.18 Wall $y^+$ values for the upper and lower isolator wall. The maximum $y^+$ is 2, which is still well within an acceptable range. ....	49
Figure 3.19 Mach contour and mesh comparison at the lower cowl leading edge for the Coarse (top), Fine (middle), and Very Fine (bottom) mesh refinement levels. The very fine refinement achieved shock resolution in the order of micrometers. While visually satisfying, it did not sufficiently change the actual data to justify having nearly eight times as many cells. ....	50
Figure 3.20 Lower isolator wall static pressure distribution comparison between the new and old mesh at the fine grid refinement level.....	51
Figure 3.21 Mach contour comparison of four lower cowl locations for 0 degree angle of attack. ....	53
Figure 3.22 Mach contour at 0 degrees angle of attack comparing the results of Transition SST (left) to $k-\omega$ SST (right). ....	54
Figure 3.23 Comparison of four different viscous solvers at 0 degrees angle of attack for the 2008 mm lower cowl location.....	55
Figure 4.1 Lower wall static pressure at all angles of attack. ....	59
Figure 4.2 The non-dimensionalized bleed rate always increases when angle of attack is increased. ....	62
Figure 4.3 Mach contour in the isolator at 0 degrees angle of attack for all porous cases. Shown are no bleed (top-left), C1000 (top-right), C500 (middle-left), C250 (middle-right), C100 (bottom-left), and C0 (bottom-right). The C values represent the porous bleeder pressure jump coefficient values, described in text.....	63

Figure 4.4 Static pressure distribution comparison along the upper (top) and lower (bottom) wall of the isolator at every pressure jump coefficient value for 0 degrees angle of attack. ....	65
Figure 4.5 The total pressure at both the isolator entrance and exit decrease with increasing angle of attack, but the ratio between the two increase. ....	68
Figure 4.6 The total pressure recovery across the isolator is higher with the addition of a porous bleeder for all cases. ....	70
Figure 4.7 Total pressure recovery across the isolator increases with angle of attack, and further increases with decreasing pressure jump coefficient. A notable exception to this pattern is the unimpeded porous bleeder, which did not yield the highest total pressure recovery. ....	71
Figure 4.8 Porous bleeder cases showed a higher effectiveness compared to the wall case. ....	72
Figure 4.9 The high pressure region starts along the upper wall of the isolator near the exit, but moves upstream as high pressure air builds up. ....	74
Figure 4.10 The high pressure unstarting flow has now reached the porous bleeder, which begins to remove the stagnant air. Some flow spillage is visible. ....	74
Figure 4.11 The static pressure distribution along the upper isolator wall at 8 degrees angle of attack and a pressure jump coefficient of 0. Displayed is an unstarted case caused by three-quarters blockage compared to the steady case. ....	76
Figure 4.12 Flow spillage has occurred and the inlet is in an unstarted state, but it can be alleviated with the help of a porous bleeder. ....	76
Figure 4.13 Mass flow rate through a porous bleeder during oscillatory unstart; the increase in mass flow due to high pressure air coming into contact with the porous bleeder are visible. ....	77
Figure 4.14 Oscillatory unstart persists for many iterations and has no indication of stabilizing once initiated. ....	78
Figure 4.15 Oscillatory period and magnitude for all cases in the three-quarter area blockage back pressure scenario. ....	80
Figure 4.16 Oscillatory period and magnitude for all cases in the two-thirds area blockage back pressure scenario. ....	82
Figure 4.17 Isolator effectiveness for all cases in the half-area blockage back pressure scenario. All cases are stable, except for the wall case at 8 degrees angle of attack. ....	83
Figure A.1 Mach contour in the isolator at 2 degrees angle of attack for all porous cases. Shown are no bleed (top-left), C1000 (top-right), C500 (middle-left), C250 (middle-right), C100 (bottom-left), and C0 (bottom-right). ....	90

Figure A.2 Mach contour in the isolator at 4 degrees angle of attack for all porous cases. Shown are no bleed (top-left), C1000 (top-right), C500 (middle-left), C250 (middle-right), C100 (bottom-left), and C0 (bottom-right)..... 91

Figure A.3 Mach contour in the isolator at 6 degrees angle of attack for all porous cases. Shown are no bleed (top-left), C1000 (top-right), C500 (middle-left), C250 (middle-right), C100 (bottom-left), and C0 (bottom-right)..... 92

Figure A.4 Mach contour in the isolator at 8 degrees angle of attack for all porous cases. Shown are no bleed (top-left), C1000 (top-right), C500 (middle-left), C250 (middle-right), C100 (bottom-left), and C0 (bottom-right)..... 93

## LIST OF TABLES

Table.....	Page
Table 3.1 CFD Settings used with ANSYS Fluent.....	31
Table 3.2 The mass flow rates into the isolator (referenced as the “Inlet” on the table) and out of the isolator (referenced as the “Outlet”) show good agreement with each other for every case. The mass flow rates for the fine and very fine grids display grid independence.....	39
Table 3.3 Lower cowl location for each angle of attack.....	52
Table 4.1 Mass flow rate readings for all cases tested with porous bleeders. ....	60
Table 4.2 Porous bleeder start and end locations for all angles of attack. ....	61

# 1 Introduction

The forefront of aerospace engineering is currently focused on advancements in the field of hypersonics. Substantial financial investments by the U.S. Government underscore the significance of ongoing scramjet research, further emphasizing its prominence in both scientific and public domains [1]. Revered as the 'Holy Grail' of propulsion, scramjets hold immense potential as an air-breathing alternative to hypersonic propulsion. However, the realization of their widespread application first requires overcoming a myriad of challenges.

## 1.1 What is a Scramjet

Combustion, at its core, necessitates three elements: compression, fuel, and oxidizer. In the context of propulsive combustion, the process typically involves compression, ignition, and expansion. A turbojet achieves this by using a compressor stage to draw in and compress air, which is then mixed with fuel and ignited. The resulting fuel/air mixture is expanded through a turbine that powers the compressor. In contrast, a ramjet relies on the forward momentum of the engine to compress air without the need for additional machinery. This compressed air is subsequently combusted, expanded, and transformed into thrust [2].

Similar to a ramjet, a scramjet (supersonic combustion ramjet) also employs the forward momentum of the air for compression but maintains the compressed air at supersonic speeds during the combustion stage. This difference enables the scramjet to operate at higher Mach numbers [2].

Each engine type possesses its own set of advantages and disadvantages. Notably, ramjets and scramjets cannot operate from a standstill; they must already be traveling at high speeds as they rely on the forward momentum of the freestream for self-compression. Consequently, an alternative form of propulsion is required to accelerate these engines to operational speeds.

A prime example is found in the J58 engines aboard the SR-71 aircraft, shown in Figure 1.1. These engines are afterburning turbo-ramjets, which use a jet engine for initial acceleration. Once reaching high speeds (typically around Mach 2), the J58 bypasses the turbojet stages and directs high-speed compressed air directly into the afterburner, effectively functioning as a ramjet [3]. This shows the necessity of combining multiple engine types or employing versatile designs, akin to the J58, to overcome the inherent limitations of the ramjet/scramjet. Many scramjet tests use rockets to attain high Mach numbers before being released to operate under their own power.

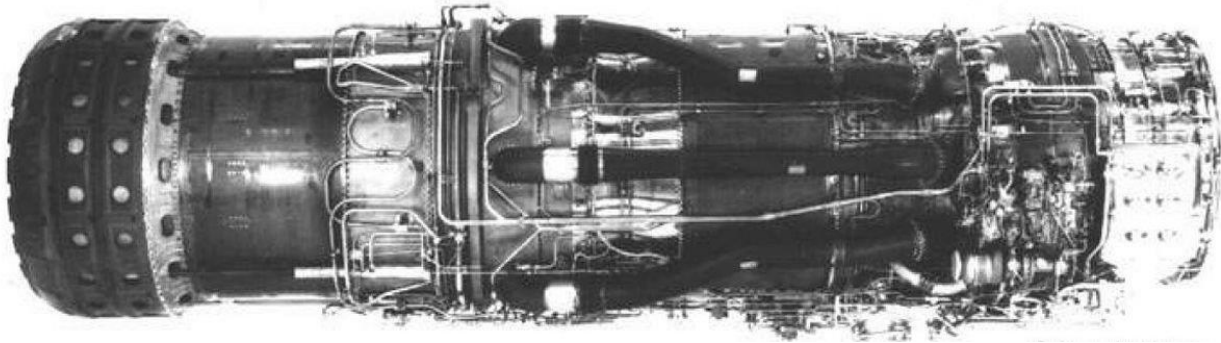


*Figure 1.1* The J58 engine used for the SR-71, with its large bypass tubes visible [3].

## **1.2 Why Scramjets**

The rationale behind embracing scramjets revolves around the pursuit of a balance between speed and fuel efficiency. While both conventional jet engines and ramjets typically outperform scramjets in terms of fuel efficiency, this expectation aligns with the increased power demands inherent in crafts traveling at higher speeds. Rockets, the current exclusive propulsion for achieving hypersonic and above velocities, possess certain advantages—such as functionality in space, an absence of an upper speed limit, robustness, and relative simplicity. However, their notable disadvantage lies in their inherent fuel inefficiency and their added weight cost.

Unlike air-breathing engines, rocket engines carry their own oxidizer to provide functionality in space, which adds significant weight. The mass of large rockets is dominated by propellant, constituting 90-95% of their total weight. The paradox of rockets lies in their low fuel efficiency, demanding large amounts of propellant for liftoff, which, in turn, necessitates more propellant to carry the extra weight. Scramjets present a compelling alternative for fuel-efficient hypersonic propulsion, shown in Figure 1.2.

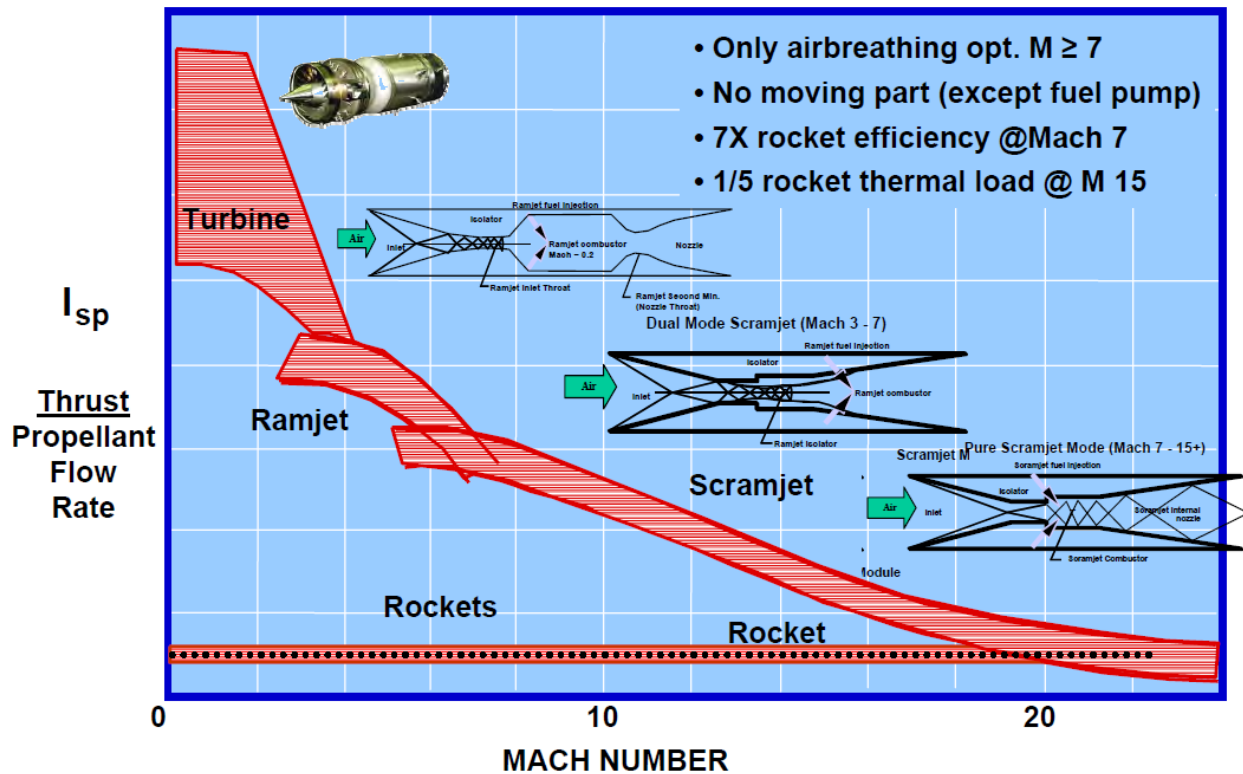


Figure 1.2 Rocket engines, although powerful, greatly fall behind air-breathing engines in terms of efficiency [4].

While rocket engines will persist for space applications, there lies potential in using scramjets to propel a rocket-powered craft to the edge of the atmosphere at hypersonic speeds, allowing the rocket to take over from there [1]. This design alleviates the necessity for a massive first stage, significantly reducing fuel consumption. Additionally, scramjets open avenues for practical hypersonic commercial applications, such as international same-day delivery and rapid personnel transfer, which is currently economically unfeasible with traditional rocket engines. Some theoretical trajectories are displayed in Figure 1.3.

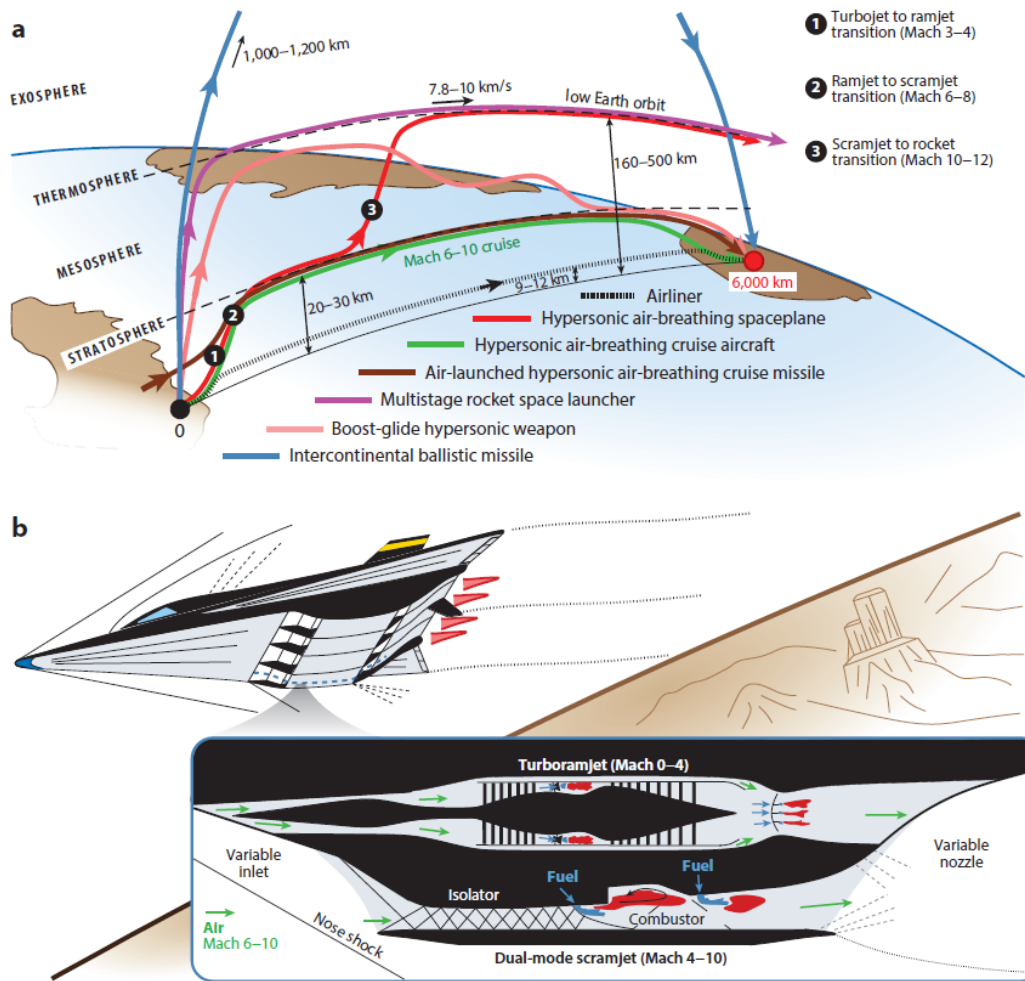


Figure 1.3 Diagram showcasing flight trajectories of various vehicles. Hypersonic air-breathing scramjets could reach low Earth orbit while keeping the efficiency of air-breathing engines [5].

### 1.3 Scramjet Obstacles

While scramjets offer a tantalizing glimpse of what the future could be, a plethora of obstacles must first be overcome. Foremost among these challenges is within the realm of structures and materials. Traveling at hypersonic Mach numbers subjects the craft to immense heat and pressure loads, leading to rapid material degradation. For example, the Apollo capsule faced temperatures as high as 11,000 K during its Mach 36 re-entry [1]. While smaller scramjet prototypes have successfully flown for short durations, the existence of large-scale scramjet craft remains improbable until this material-related issue is resolved.

Another significant hurdle is flameout, a complication likened to "lighting a match in a hurricane." However, this comparison underplays the true complexity of maintaining ignition. For context, a category five hurricane boasts wind speeds exceeding 157 miles per hour. The X-43A's final flight, still holding the record for the fastest air-breathing craft ever, reached a speed of Mach 9.6 (at 109,000 feet altitude), exceeding 6,850 miles per hour [4].

An obstacle of particular relevance to the current work is engine unstart. This phenomenon occurs when the incoming airflow is insufficient to overcome the internal pressure of the engine. Consider a conical paper cup with its smaller end cut off to create a tube, gradually decreasing in cross-sectional area. If one were to walk with this cup, keeping its larger area facing forward, air would flow through the tube with minimal impedance. However, holding the cup out of a car window while driving down a highway would attempt to push an excessive amount of air through the tube, rendering it physically incapable of accommodating the pressure. In this scenario, the air inside the cup would pressurize, forming a high-pressure bubble, which would then redirect the incoming freestream around the cup.

In the case of supersonic unstarts typical in scramjets, a large normal shock forms in front of the scramjet inlet. This highly pressurizes the air inside the inlet, making recovery challenging, causing the airflow to become subsonic, and preventing air from flowing through the engine leading to a loss of thrust, a potentially fatal combination if not promptly addressed [2].

Lastly, the extreme environment of hypersonic flight poses incredible challenges, rendering scramjets designed for very specific conditions and lacking robustness. When designing a scramjet engine, the intended altitude and Mach number, known as design conditions, are predetermined. Scramjets operating outside these conditions are highly susceptible to unstart. Additionally, scramjets with inward turning compression designs, while more efficient, also exhibit increased susceptibility to unstart and high spillage drag at off-design conditions [2].

#### **1.4 Preventing Unstart**

While the design of scramjets presents numerous challenges, the specific focus of this research is to enhance the robustness of scramjet performance. The primary objective is to prevent or postpone unstart under off-design conditions by implementing porous bleeders. The current work aims to achieve this by influencing the shock train within the isolator section through active air bleeding, maintaining manageable air levels entering the compressor.

It is important to note that the porous bleed method used for air extraction from the isolator is a 'black box' porous bleeder. In other words, the emphasis of this research lies in observing the effects of removing air at specific locations on the shock train, rather than achieving precise modeling of porous bleeders. Therefore, this research serves as a feasibility study on porous bleeders to assess their potential to influence the flow dynamics of the isolator. The investigation seeks to determine if porous bleeders can successfully be employed to affect isolator flow dynamics and if they can be helpful in preventing unstart in certain cases.

## **2 Background & Literature Review**

Due to the relative recency of the surge in serious scramjet development, coupled with the government's keen interest in scramjets for military applications, there is a scarcity of publicly available sources pertaining to scramjet research. Existing research primarily addresses topics such as fuel, methods of ignition, and combustion, with limited emphasis on airflow control to prevent unstart or the impact of introducing porous bleeders. Despite recent interest in porous bleeders, exemplified by events like NASA's 2023 PAW6 workshop, the predominant focus remains on creating accurate Computational Fluid Dynamics (CFD) models of porous bleeders that align with experimental data, rather than exploring the potential influence of these bleeders on airflow. Additionally, due to the recent occurrence of this workshop, neither the workshop itself nor any associated publications have been officially published at the time of the present work's writing.

### **2.1 The Scramjet Design**

Scramjets comprise four distinctive regions, shown in Figure 2.1 — the inlet, isolator, combustor, and exhaust. The inlet, similar to traditional engine inlets, is designed to collect and direct incoming air into the engine while raising its pressure. However, the scramjet inlet diverges from its conventional counterparts, demanding a specific design to generate a favorable leading oblique shock. This shock is pivotal for initiating the shock train at the designated Mach number, which further evolves in the isolator [2]. Positioned between the inlet and combustor, the isolator ensures an unobstructed transition for the flow and separates the combustor from the inlet. The inlet and isolator must function together seamlessly to optimize the flow of incoming air [2].

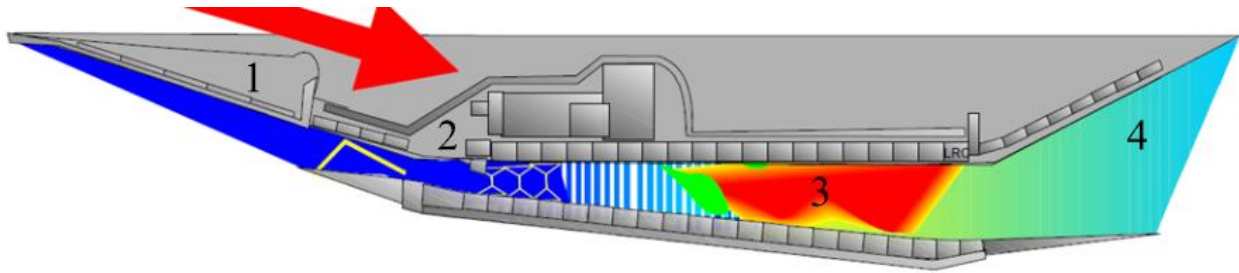


*Figure 2.1* Sideview of a scramjet engine showing the (1) Inlet, (2) Isolator, (3) Combustor, and (4) Exhaust [4].

The scramjet inlet stands out as the most visually distinct component of the scramjet and has undergone significant development over the past several decades. Evolving from the iconic wedge-shaped design, which prioritized robustness, modern three-dimensional inward-turning compression inlets and waveriders have taken center stage [2]. These designs aim to capture and compress air for the scramjet engine more efficiently. Waveriders, for instance, are not solely an inlet design but rather a design condition for the entire scramjet craft. They are specifically crafted to follow the curvature of the shockwave they generate, essentially existing within their high-pressure 'bubble' [6]. While these designs possess enhanced efficiency, their design is geared toward specific operating conditions, which when compounded by the inherent specificity of scramjet design, renders them more susceptible to unstart.

The isolator, shown in several modes in Figure 2.2, is a critical component within the scramjet that serves multiple crucial functions. It allows sufficient time for the shock train to develop and acts as a separator between the combustor and the inlet, ensuring that the shock train progresses without interference. Additionally, the isolator plays a pivotal role in converting airspeed into absolute pressure, aiming to slow down the incoming air to provide the combustor with additional time for fuel vaporization, mixing, and ignition. The ideal isolator achieves maximum total pressure recovery by maintaining the kinetic energy of the incoming air as total

pressure. While losses occur due to the formation of oblique shocks in the isolator, preventing an isentropic condition where total pressure is preserved, the isolator remains a key element in optimizing the performance of the scramjet.

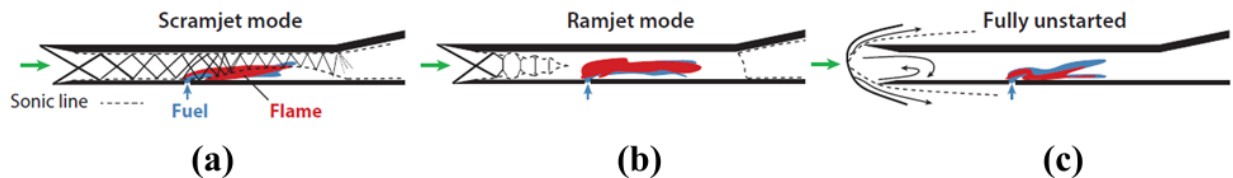


Figure 2.2 An isolator in (a) Scramjet mode, (b) Ramjet mode, and (c) Unstarted mode [5].

The combustor region is an area that holds immense research interest. The combustor's primary task is to ignite fuel in the incoming compressed supersonic stream of air provided by the inlet/isolator combination. This undertaking is arguably the most challenging aspect of creating a functional scramjet, explaining the plethora of studies conducted on the topic. At the speeds at which the air enters the combustor, the combustor has mere microseconds to mix and burn fuel into the incoming air. This is sometimes accomplished with the use of a cavity flameholder [7], shown in Figure 2.3, that recirculates air to simplify the process of fuel injection. Presently, there is significant interest in developing dual-mode ramjet/scramjets [8-12], depicted in Figure 2.4, relying heavily on the combustor's ability to successfully combust air in both subsonic and supersonic conditions.

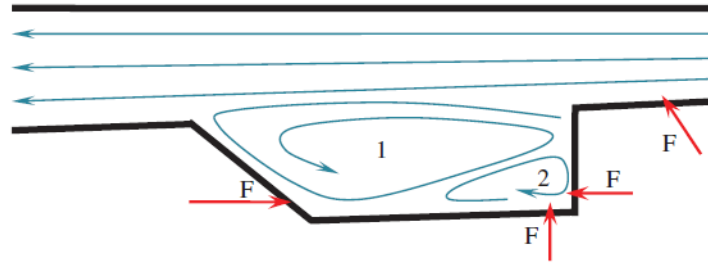


Figure 2.3 A diagram depicting a cavity flameholder design [7].

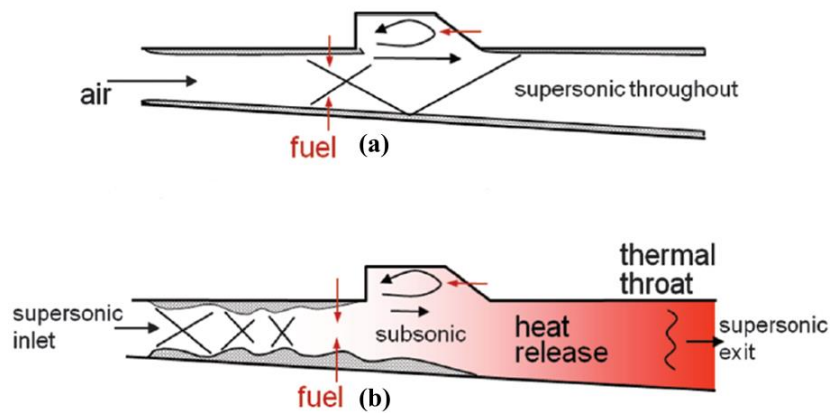


Figure 2.4 Dual-mode ramjet/scramjets are designs in which the combustor is capable of igniting fuel in both subsonic and supersonic incoming airflow [12].

Concluding the discussion of key components, attention turns to the exhaust region. While undeniably necessary for a scramjet to function, the exhaust poses a comparatively lower technical challenge than its preceding counterparts. The engineering community has a well-established foundation in the exhaust of supersonic propellants, with established methodologies that, while not yet perfected for scramjets, provide a robust starting point. While the intricacies of the exhaust process for scramjets may require further refinement, it is noteworthy that less active research is currently directed towards this region. This relative sparsity of research attention could be attributed to the perceived challenges inherent in the preceding components, emphasizing the complexities of the inlet, isolator, and combustor.

## 2.2 The Unstart Phenomenon

At its core, unstart refers to the disruption of the stable shock train within the isolator region, leading to a sudden loss of thrust and a deviation from normal combustion processes. It is noteworthy that unstart is a comprehensive term encompassing both the disruption of the shock train and flow spillage, the catastrophic condition akin to compressor surge, where airflow reverses within the isolator and impedes any further air passage [13]. The consequences of unstart can range from a momentary loss of performance to severe damage to engine components.

The unstart phenomenon in scramjet engines is primarily caused by an inadequate total pressure through the isolator to overcome the pressure in the combustor region [2]. This condition sets the stage for potential disruptions in the shock train, leading to a cascade of consequences. Several factors can contribute to the occurrence of unstart.

One significant factor is variations in the incoming airflow, influenced by changes in flight conditions, alterations in the operating environment, or fluctuations in the engine's operational parameters. Inconsistencies in the incoming air can disturb the delicate balance required for a stable shock train, triggering the onset of unstart. Dynamic changes in the engine's operating regime, including alterations in the angle of attack or Mach number, introduce additional challenges in maintaining the necessary pressure differentials for a stable shock train, making the engine more prone to unstart under certain flight scenarios [13].

Fuel ignition in the combustor represents another critical element. As fuel ignites in the compressed supersonic stream of air provided by the inlet/isolator combination, it leads to a rapid increase in pressure within the combustor region. This surge in pressure, coupled with the phenomenon of Rayleigh flow, significantly impacts the stability of the shock train. Adding heat to the flow not only elevates the pressure but also tends to drive the flow toward sonic conditions

(Mach 1). In scenarios where the incoming flow is already supersonic, continuous heating causes the supersonic air passing through the isolator to decelerate. This deceleration disrupts the equilibrium necessary for maintaining a stable shock train, creating conditions conducive to unstart events.

Catastrophic inlet unstarts that lead to flow spillage can result in the formation of normal shocks in front of the inlet, obstructing airflow from entering like observed in Figure 2.5. Reversing this condition can be exceptionally challenging. In their experiment using air throttling to induce an unstart state, the results of which are shown in Figure 2.6 and Figure 2.7, Bao et al. [14] demonstrated that the pressure in the isolator “does not return to the undisturbed state ... and the airflow at the combustor entrance remains subsonic.”

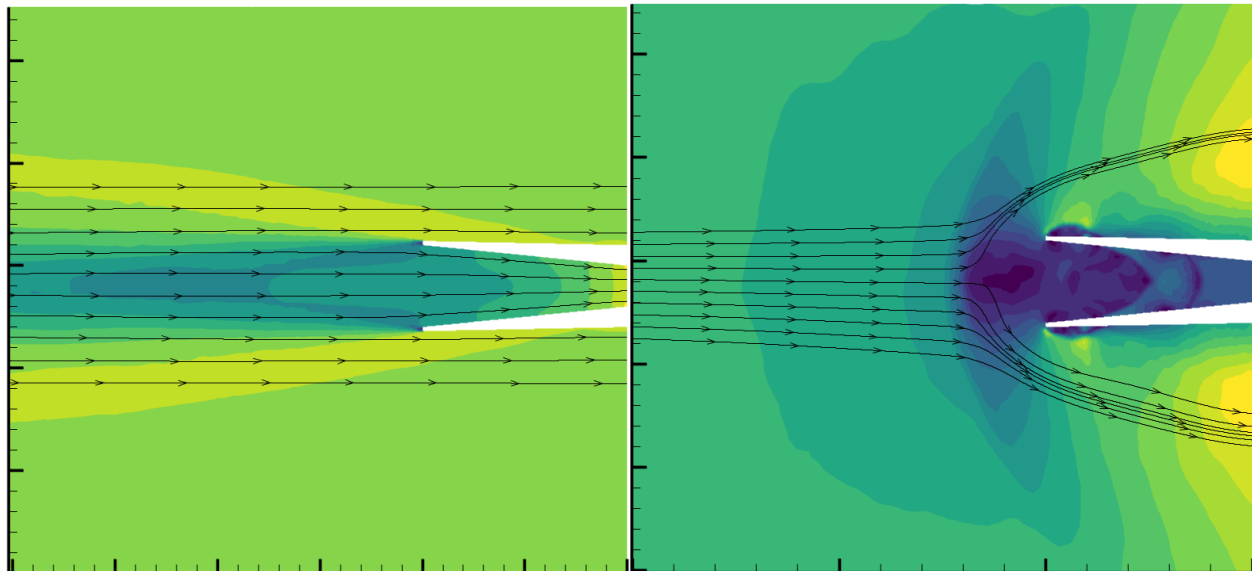


*Figure 2.5* (Left) A functioning inlet can compress incoming air. (Right) A supersonic unstarted inlet creating a normal shock and preventing any airflow into the engine. Results from the present work.

In the stable scenario illustrated in Figure 2.6 (a), there is a notable surge in pressure ratios across the model following the activation of air throttling at  $t = 8$  seconds. Upon deactivation of the throttling at  $t = 9.2$  seconds, the pressure ratio at the inlet, marked by the blue dashed line, promptly reverts to a level slightly above 1. This behavior signifies a slight compression of incoming air at the inlet, resulting in the anticipated increase in pressure.

Conversely, in the unstarted scenario depicted in Figure 2.7 (a), upon the deactivation of air throttling at  $t = 8.7$  seconds, the inlet pressure ratio fails to return to 1, instead persisting at a magnitude of 4. This persistence indicates the development of a normal shock preceding the inlet, leading to a significant elevation in static pressure. In the absence of active adjustments to the engine, the inlet tends to persist in an unstart state.

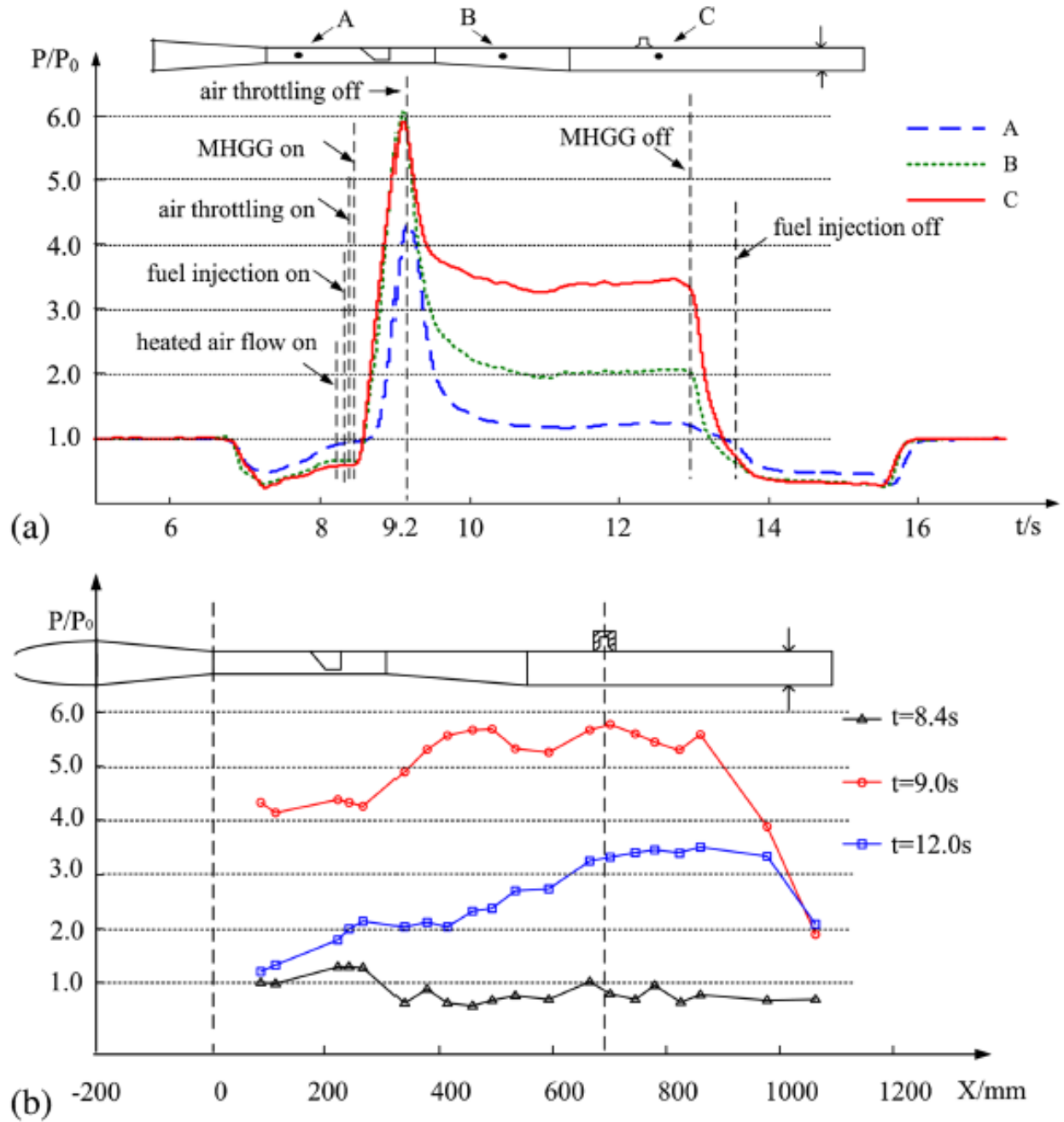


Figure 2.6 In a stable case, after the air-throttling is turned off, the blue dashed line measuring the pressure ratio at the inlet returns to close to 1 [14].

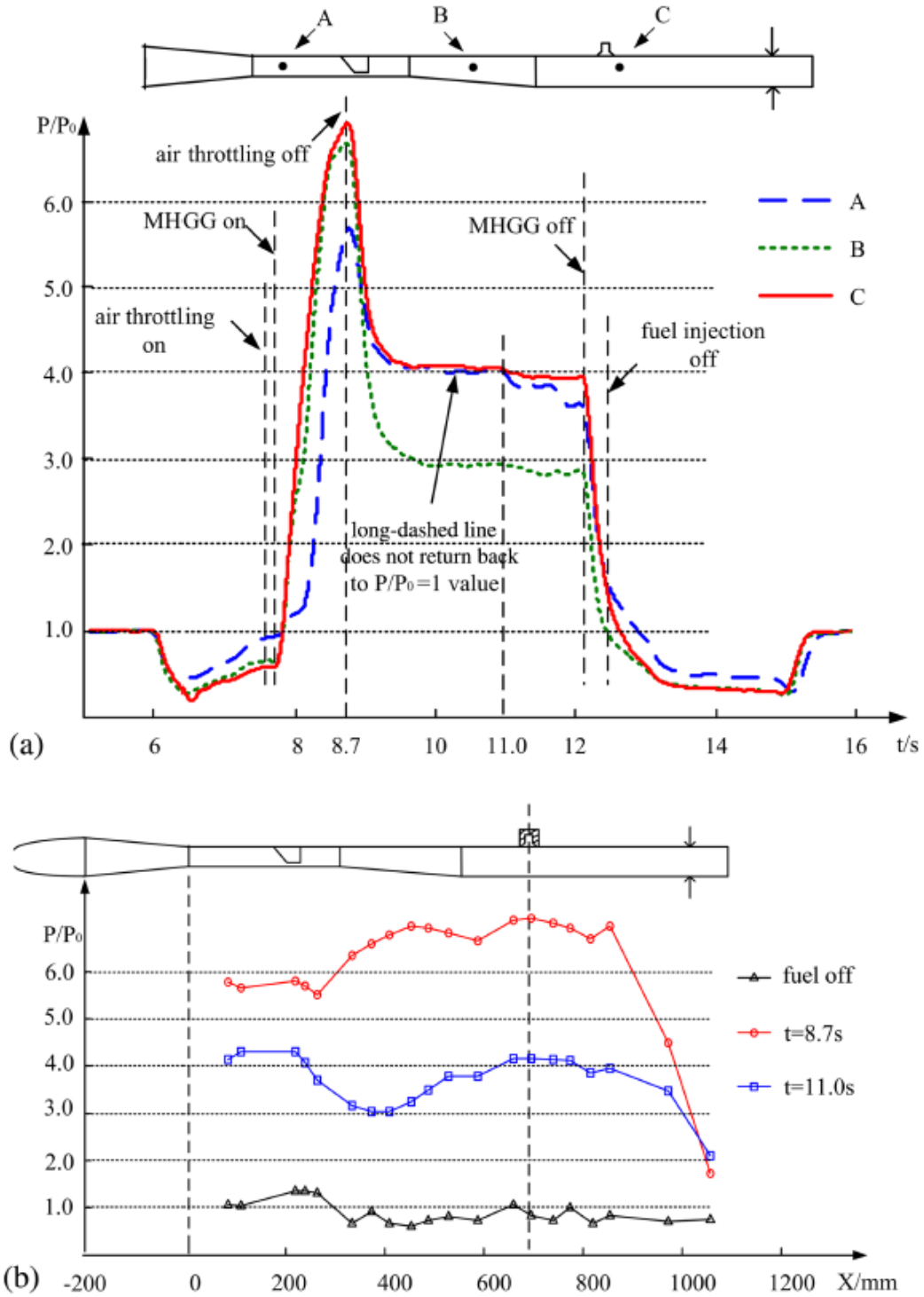
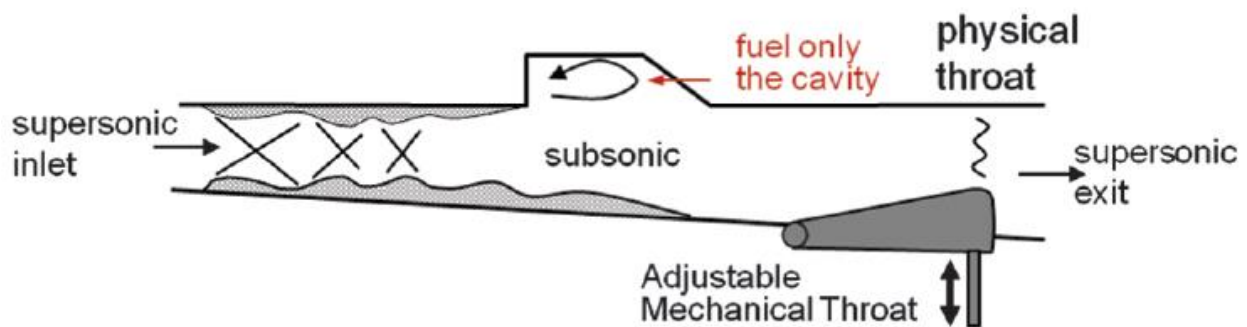


Figure 2.7 In an unstarted case, the blue dashed line representing the inlet pressure ratio does not return to close to 1 after air-throttling is turned off, as the inlet has unstarted and a high-pressure region has formed [14].

While the most realistic cause of unstart induced by back pressure is excessive ignition within the combustor, it is noteworthy that other factors can contribute to an increase in back pressure. Studies conducted by both Donohue [12] and Im and Do [13] employed mechanical blockages, depicted in Figure 2.8, to simulate internal flow choking. While flow choking itself may lead to ramjet-like flow structures and not necessarily cause unstart, it can generate sufficiently high back pressures to trigger unstart. The primary advantage of using a mechanical blockage lies in its ability to replicate heat addition by elevating back pressure without the need to model the complex phenomenon of combustion.



*Figure 2.8* A mechanical throat can be employed to arbitrarily increase back pressure without the need for ignition or combustion modeling [12].

Furthermore, the manipulation of the blockage allows for variations in the imposed back pressure. In Donohue's study [12], “Three different mechanical throttle positions allow[ed] three different backpressure levels, providing three P ratio values and shock train positions in the upstream duct.” This approach to controlling back pressure proves particularly advantageous in CFD applications, as modifying the mesh geometry to accommodate the mechanical blockage is relatively straightforward. In contrast, accurately modeling combustion can be intricate, time-consuming, and, most importantly, prone to inaccuracies.

While inclusion of an intentional mechanical blockage is not a design consideration for a functional scramjet, a phenomenon resembling mechanical blockage can manifest during scramjet operations. According to Im and Do [13], “It is well-known that subsonic regions exist within boundary layers in supersonic internal flows, and the intensive combustion and shockwave impingements can induce a local subsonic area.” Under specific parameters, this subsonic region has the potential to expand, acting as a blockage that diminishes the throat area. This effect is illustrated in Figure 2.2 (a) where, “The increased pressure extends the subsonic portion, and under a certain range of conditions, the virtual area of the choked throat decreases” [13].

Researching unstart dynamics is complicated by the inherent unsteadiness of the incoming air flow. Before reaching a full unstart state where no flow can enter the isolator, Donohue [12] notes the flow dynamics become unsteady “due to the presence of the shock train. In previous studies with all subsonic flow and all supersonic core flow, this level of unsteadiness at the flameholder was not reported.” Im and Do [13] emphasize the unsteady and transient nature of unstating flows throughout their paper, noting that “numerical approaches could interpret the complex unsteady flow behavior that cannot be observed in experiments.” However, such approaches would require detailed transient CFD simulations. Steady-state approaches, while sufficient to detect full unstart cases, would not be able to accurately assess the rapidly time-varying nature of the unsteady unstart phenomenon.

On the topic of CFD, Snider et al. [15] used CFD to assess the truncated Busemann inlet, an axisymmetric 3D compression inlet, and its susceptibility to unstart under off-design conditions. In this study, Snider et al. demonstrated the necessity for a sufficiently refined grid to properly capture whether a case would unstart, as shown in Figure 2.9. The study found that “Although not every case that eventually unstated began with a started solution on the baseline grid, only after

adaptation could it be determined definitively that a case would not unstart” [15]. The authors hypothesized that the “reason for the unstart after grid adaptation is the increased resolution of the shock-boundary layer interaction in the throat area” and also mentioned “a mesh fine enough to capture intricate shock-shock and shock-boundary layer interactions in an initial grid is unlikely to be computationally efficient as a whole” [15].

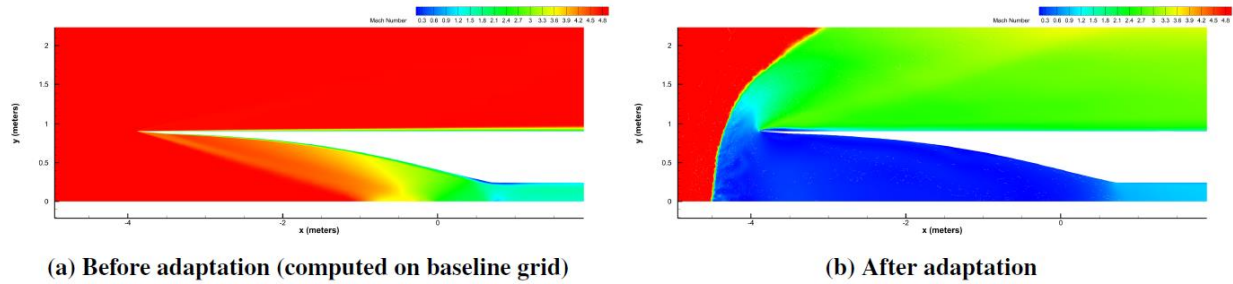
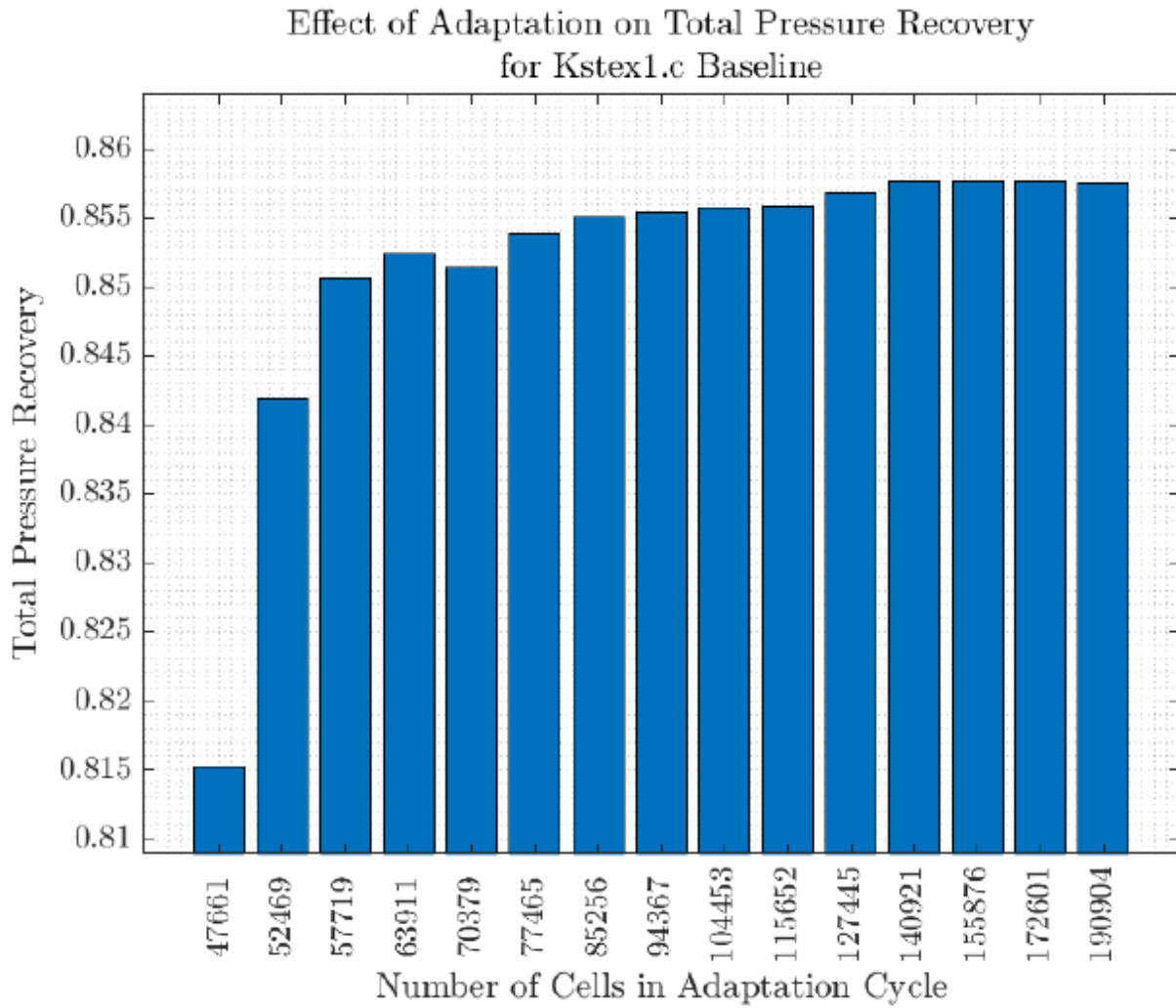


Figure 2.9 A more refined grid can capture an unstart where a coarser grid may fail to [15].

Furthermore, the study conducted by Snider et al. revealed that measurements such as total pressure recovery were dependent on cell count until grid independence was achieved, visualized in Figure 2.10. Additionally, without grid refinement, some oblique shocks and shock impingements were not accurately captured, as illustrated in Figure 2.11. Initiating simulations with a mesh containing an ample number of cells to accurately capture these interactions would demand a considerable amount of computational resources, emphasizing the need for active grid adaptation in these CFD simulations.



*Figure 2.10* A sufficient amount of grid refinement is required to properly measure the amount of total pressure recovery [15].

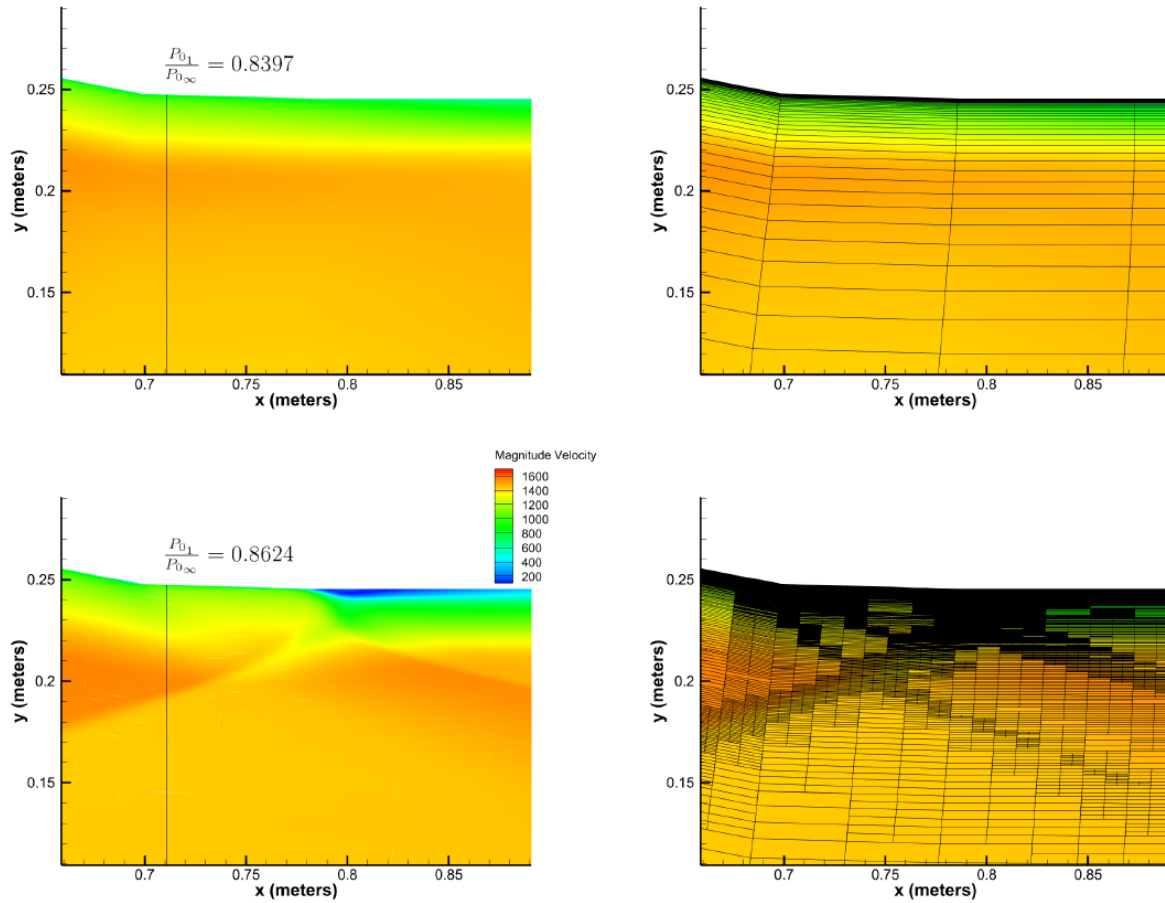


Figure 2.11 Many flow features would not be properly captured without sufficient grid refinement [15].

Finally, the investigation by Snider et al. [15] revealed that “Even when all other variables were kept constant—grid, inlet conditions, turbulence settings, flow initialization—decreasing the Courant number could prevent a case from unstating.” This discovery suggests that while grid independence is necessary to resolve unstated cases, unstart may also be a path-dependent phenomenon. Fortunately, the study conducted transient time-accurate cases and found similar results, indicating that steady-state local time stepping is appropriate for these cases. However, this applicability appears to be suitable only for fully unstated cases and does not encompass unsteady unstart scenarios.

### 2.3 The X-43A

The Hyper-X program, initiated in the mid-1990s as a successor to the canceled National Aerospace Plane (NASP) program, aimed to advance hypersonic flight and scramjet propulsion. It outlined three proposed vehicles: the X-43A, shown in Figure 2.12, the X-43B, and the X-43C. The X-43A, the sole realization of the program, was initially designed for hypersonic speeds up to Mach 7 and used a modified Pegasus rocket booster, shown in Figure 2.13, launched from NASA's B-52B for takeoff.



*Figure 2.12* The X-43A was a 12 foot long wedge-shaped hypersonic scramjet [4].



*Figure 2.13* A modified Pegasus rocket booster was used to accelerate the X-43A after separation from the B-52 [16].

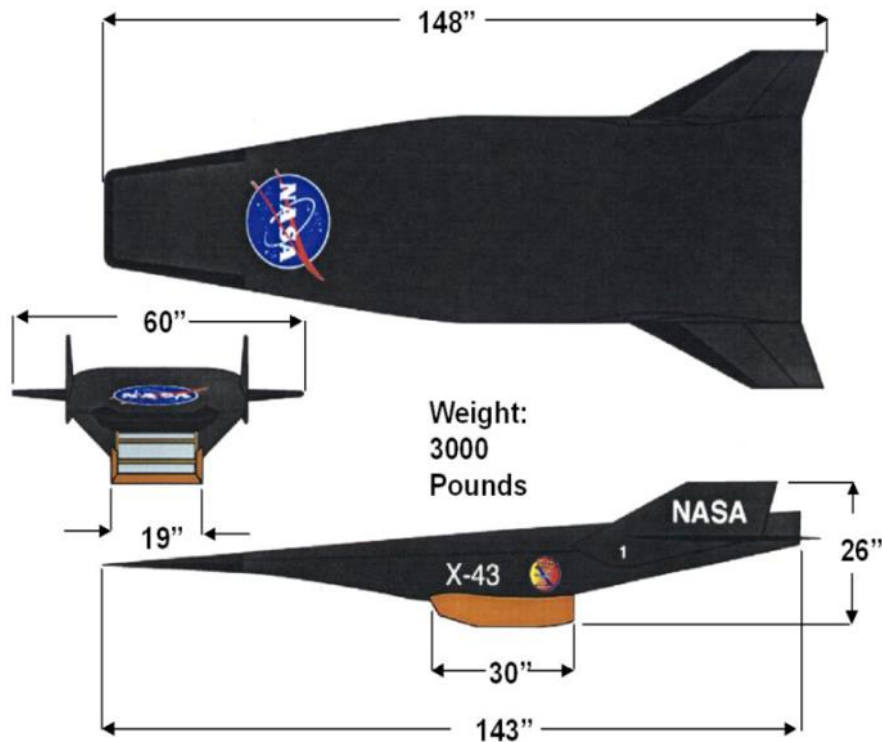
The program's maiden flight on June 2, 2001, encountered challenges, resulting in the loss of the X-43A. The booster lost control, deviating the X-43A off course and leading to its destruction as a safety precaution. The subsequent investigation revealed that the first launch, at approximately 20,000 feet, subjected the booster to dynamic pressures at transonic conditions twice that of a standard Pegasus flight. To mitigate this, 3,350 lbs of propellant were removed from the booster [17]. In subsequent launches, the B-52B, shown in Figure 2.14, ascended to the standard launching altitude of approximately 40,000 feet. During the second flight on March 27<sup>th</sup>, 2004, the Pegasus booster carried the X-43A up to 95,000 feet before separation, enabling the X-43A to reach Mach 6.83 [4, 17, 18] under its own power. The third flight, on November 16, 2004, followed a similar trajectory. However, this time the Pegasus rocket booster took the X-43A to 110,000 feet, setting the record at Mach 9.68 [4, 17, 18] and solidifying its position as the fastest air-breathing vehicle ever made.



*Figure 2.14* The Pegasus rocket booster carrying the X-43A separates from NASA's B-52B [11].

The proposed X-43B and X-43C were canceled in 2006 and replaced by the X-51. The success and record-setting nature of the X-43A's third flight have contributed to a plethora of papers discussing or referencing the X-43A [4, 9-11, 16-27]. The groundbreaking achievements during this flight have spurred extensive research and analysis, making the X-43A a focal point in the discourse surrounding hypersonic flight, and is also the reason why the base X-43A geometry was used as the inspiration for this research.

Despite the success and fame of the X-43A, specific details about its design are challenging to locate. While not classified, the X-43A's design is proprietary, and therefore, detailed schematics are not publicly available. However, two key resources have aided this research. The first is the overall dimensions of the X-43A, shown in Figure 2.15, provided by NASA [4].



The second resource is an independent study conducted by Kotov et al. [27] in 2018, in which a model based on the X-43A geometry was tested in a Mach 7 hypersonic wind tunnel. Although not an exact replica of the X-43A, this study proved invaluable as it provided schematics for the model tested and experimental visual data for comparison with CFD simulations. The Hyper-X team, in their conclusions, highlighted that flight data validated wind tunnel testing data, affirming the relevance of wind tunnel testing for scramjets [4, 17, 18].

The schematics of the X-43 model variant tested at Mach 7 conditions in Kotov et al.'s wind tunnel tests are illustrated in Figure 2.16. The tests were performed using the Hypersonic Aerodynamic Shock Tube (HAST) facility. This facility, depicted in Figure 2.17, is capable of Mach 4.5 and Mach 7 airspeeds and has an overall length ranging from 14.5 to 22 meters, depending on the desired flow characteristics [28]. CFD tests performed by Kotov et al. [28] to validate the data used a freestream pressure of 9,977 Pa, a freestream temperature of 100 K, and a velocity of 1,402 m/s. Further technical details about the HAST facility can be found in [28]. The resulting shadow graph of the wind tunnel test is presented in Figure 2.18.

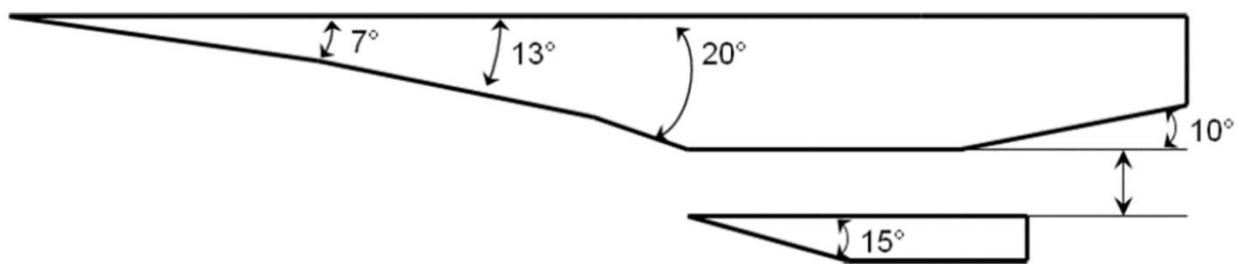


*Figure 2.16* Schematics of the design based on the X-43A geometry tested in the HAST facility [27].



*Figure 2.17* A picture of the HAST facility used for Kotov et al.'s study [28].



*Figure 2.18* Shadow picture combination of all parts of the inlet model [27].

Figure 2.19 provides a detailed view of the isolator section. At the lower cowl, the leading oblique shock and the second oblique shock converge at point 1, coinciding with the formation of the shock from the lower cowl. The third oblique shock reaches the lower cowl at point 2, where it is “reflected” (technically it is more likely to be a boundary layer induced shock, but the exact flow phenomena occurring at this point are complex and it looks and acts as a reflected shock so it will be referred to as such). As the upper wall of the isolator begins, the flow initially expands

but then becomes detached, interacting with the reflected shock from point 2 at point 3, resulting in the creation of another oblique shock denoted as point 5.

Continuing through the isolator, the reflected shock from point 2 persists until it reaches the top of the isolator, reflecting again off of the upper wall at point 4 and generating another oblique shock. Finally, at point 6, the flow expands out of the isolator. This experimental data was instrumental in validating the results obtained from CFD simulations.

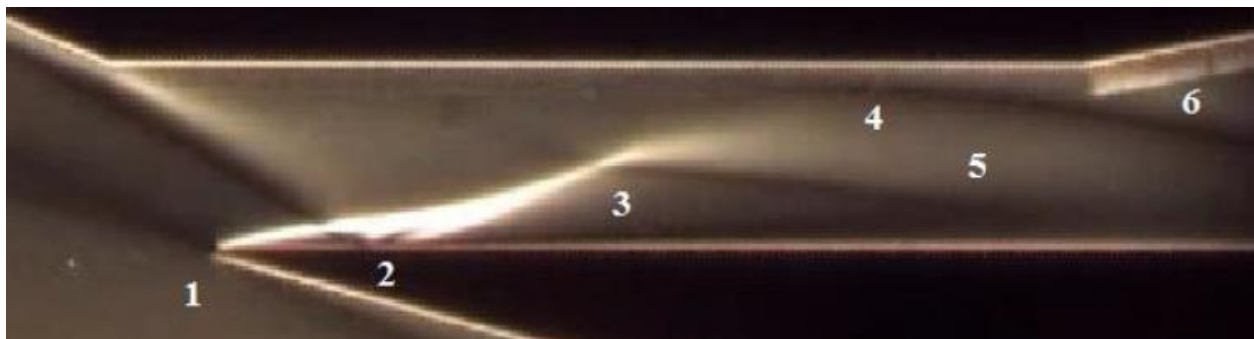


*Figure 2.19* Shadow picture of flow entering the isolator [27].

## **2.4 The Porous Bleeder**

While scramjet technology has a history of research and development spanning several decades, certain concepts, such as porous bleeders, have recently gained renewed attention within the last decade. The idea of employing porous materials to manage boundary layer conditions and enhance scramjet performance has re-emerged in hypersonic propulsion research. References to porous bleeders can be traced back to earlier discussions, with a notable example dating back to Slater's 2009 study [29]. However, it is the recent advancements and the resurgence of interest in porous bleeders that have brought this concept back into the forefront of hypersonic propulsion research.

The current work is primarily focused on investigating the effects of removing high-pressure air from the airflow within the isolator and understanding its impact on flow dynamics. Rather than delving into the intricacies of the method used for air removal, this research employs a 'black box' approach, using porous bleeders to remove air by any effective means. However, some (admittedly limited) background into the field of porous modeling research is warranted.

Slater's aforementioned 2009 study [29] conducted porous modeling research using 90-degree bleed holes. The study demonstrated good agreement with experimental data by employing a table of empirically based sonic flow coefficients and scaling that data. The scaling technique effectively collapsed the sonic flow coefficient data into a trend that could be fitted with a quadratic polynomial, showcasing the potential of this method for CFD modeling of porous bleeders.

More recently, in 2023, Slater played a role in the creation of NASA's 6th Propulsion Aerodynamics Workshop (PAW6). The objective for that year was predominantly for researchers to create CFD models of a porous bleeder and compare it with NASA's Mach 3 experimental data acquired from NASA's 1507 Inlet Case. However, this workshop, and all publications created for and pertaining to this workshop, have not yet been officially published and cannot be cited.

## **2.5 The Objective**

This research performs a feasibility study aimed at determining the effectiveness of incorporating a porous wall in the inlet or isolator section of a scramjet engine to actively control internal flow dynamics and prevent or delay engine unstart. The underlying theory relies on the principle that air with lower velocity possesses higher static pressure, and regions of stagnant airflow or subsonic vortices inherently exhibit elevated static pressure. By strategically introducing porous bleeders at these locations, the stagnant high-pressure air can be extracted, resulting in less impeded airflow in the isolator and yielding a higher total pressure.

To investigate the effects of porous bleeders on isolator flow dynamics, the angle of attack of the scramjet will be varied from 0 to 8 degrees in 2-degree increments. Each angle of attack will include a case without porous bleeding for comparison, along with five cases featuring different bleed amounts to analyze the impact of air removal on flow dynamics. Although the mass flow rate into the combustor will decrease, the primary focus of this study is to determine whether unstart can be mitigated by restricting the amount of air reaching the combustor and whether the remaining airflow exhibits a higher total pressure recovery compared to scenarios without porous bleeders.

After completing these baseline cases, additional tests will be conducted with increased back pressure using the mechanical blockage method previously referenced. This approach ensures a sufficiently accurate representation of the pressure caused by combustion without the need for the complex modeling associated with combustion. Multiple cases with variations in throat area will test the effectiveness of porous bleeders at different angles of attack and back pressures.

The effectiveness of porous bleeders will be assessed through both qualitative and quantitative measures. First, a qualitative visual examination will determine whether the airflow through the isolator experiences fewer impediments by incorporating porous bleeders. This inspection will also assess whether the inclusion of a porous bleeder can prevent unstart in cases where unstart would have occurred without one. A quantitative method for determining the effectiveness of isolators with porous bleeders will also be developed to facilitate comparisons between different porous configurations.

### **3 Methodology & Foundational Setup**

To initiate porous bleeder experimentation, the creation and validation of a case where they can be implemented and tested is essential. This process involved establishing a base case, validating it against experimental data to ensure accurate representation and alignment with reality, demonstrating grid independence to eliminate mesh-induced alterations, enhancing the mesh by incorporating insights from the base case, and collecting data for comparisons with porous bleeder cases. Additionally, achieving optimal CFD settings for computational efficiency is desired, but doing so without compromising realism is crucial. This section outlines the steps taken to establish the groundwork and foundational basis on which the porous bleeder experiments will be conducted.

#### **3.1 Base Structured Mesh Creation**

The initial mesh for testing the X-43 geometry was generated by first creating an outline of the schematic provided in Figure 2.16 using Autodesk Inventor [30]. The dimensions of the X-43, as illustrated in Figure 2.15, were then overlaid on the drawn schematic to scale it appropriately. This process is visualized in Figure 3.1. The resulting geometry was exported to Fidelity Pointwise [31], where it was meshed into a CAE file suitable for conducting CFD simulations using ANSYS Fluent [32].

In Pointwise, the mesh was designed to have orthogonal structured cells extruded from the cell walls with the target wall  $y^+$  values set to one to ensure the proper capture of boundary layer flow. Overpredicting a velocity over the wall at the freestream velocity of Mach 7, this led to an initial wall spacing of  $8.2 \times 10^{-6}$  m. However, as will be discussed in 3.3 Improved Unstructured Mesh Creation, this fine wall spacing eventually posed challenges.

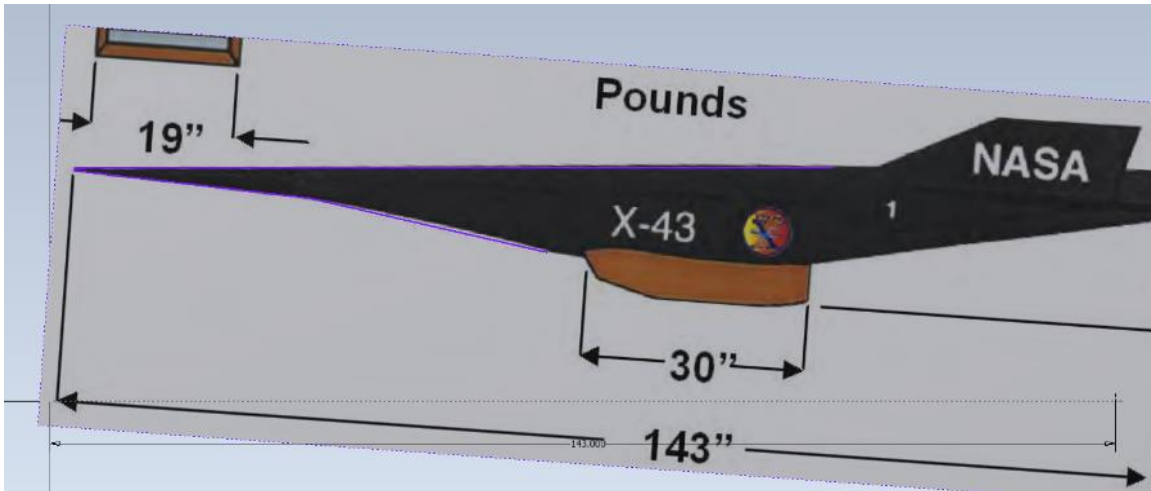


Figure 3.1 The provided schematics were used in tandem with the overall dimensions to create a scaled to size mesh.

The remaining portions of the grid were populated with an unstructured domain to adequately capture the freestream. The outcome of the initial base grid, consisting of approximately 700,000 cells, is depicted in Figure 3.2.

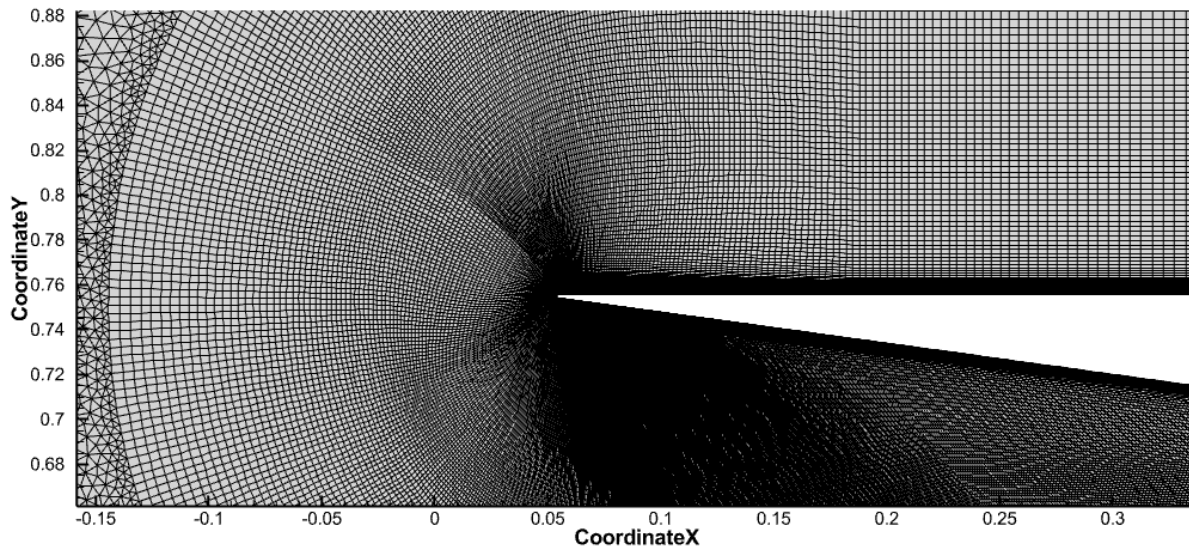


Figure 3.2 The structured mesh at the front of the X-43. The mesh becomes very dense near the wall surfaces.

The current work conducted the base non-bleed control cases under the same conditions as the X-43's inaugural successful launch, operating at Mach 7 and 95,000 feet altitude. The atmospheric pressure and temperature at this altitude are 1,437 Pa and 225 K. A pressure far-field (PFF) condition was imposed on all external boundaries, except for the combustor outlet, which had a pressure outlet condition applied to it. The initial runs to evaluate the base cases were carried out using the settings outlined in Table 3.1.

*Table 3.1* CFD Settings used with ANSYS Fluent

<b>SETTING</b>	
ATMOSPHERIC CONDITIONS	1,437 Pa   225 K
AIR PROPERTIES	Density: Ideal Gas Cp: NASA-9 piecewise polynomial Thermal Conductivity: Kinetic Theory Viscosity: Sutherland's
PRESSURE FAR-FIELD	Mach: 7 Intermittency: 1 Intensity: 0.1% Length Scale: 0.018 m
VISCOUS MODEL	Transitional SST (Default Settings)
METHOD	Implicit   AUSM   Second Order Discretization
CONTROLS	Courant #: 1

As was mentioned in Section 2.2 The Unstart Phenomenon, grid adaptation will be necessary to fully capture the flow dynamics and produce accurate results, but the extent of grid adaptation required for this specific case to achieve grid independence must be determined. To address this, the unmodified 'Coarse' grid was solved for 100,000 iterations. Then, refinement was applied based on pressure and density criteria, resulting in an adapted 'Fine' grid. This refined grid was then solved for an additional 100,000 iterations, adapted once more to a 'Very Fine' grid using the same criteria, and finally solved for an extra 100,000 iterations, totaling 300,000 iterations. The selected iteration count is intentionally high for an abundance of caution and exceeded the necessary iterations for reaching a steady-state solution.

This grid independence assessment was repeated for all angles of attack to ensure consistency across variations of the grid. In each case, five parameters were recorded to evaluate grid independence. The first parameter was the Mach contour through the isolator, serving for visual inspection and shown in Figure 3.3. For quantitative analysis, the static pressure distribution on the upper and lower wall surfaces of the isolator, along with the mass flow rate into and out of the isolator, were measured.

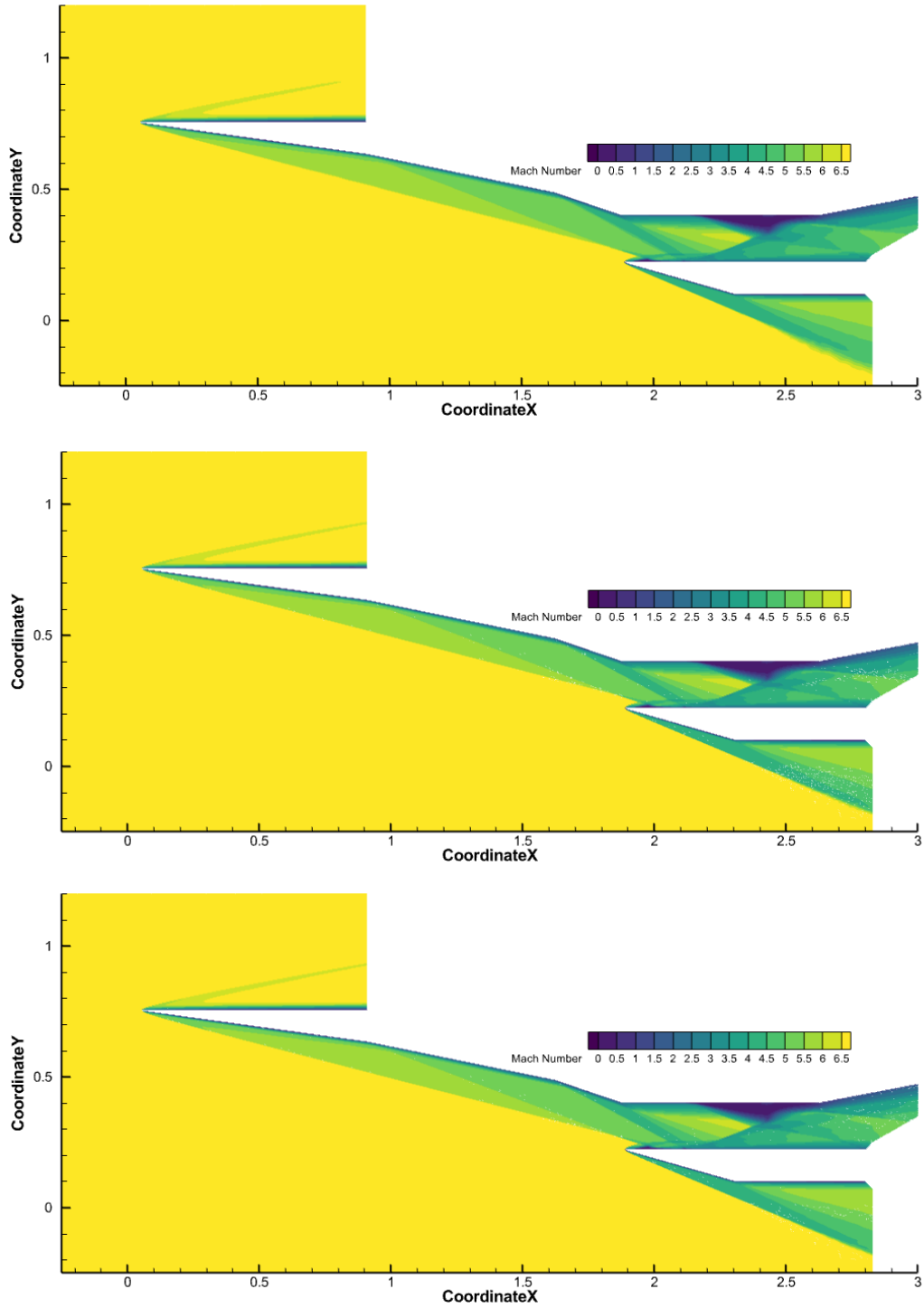
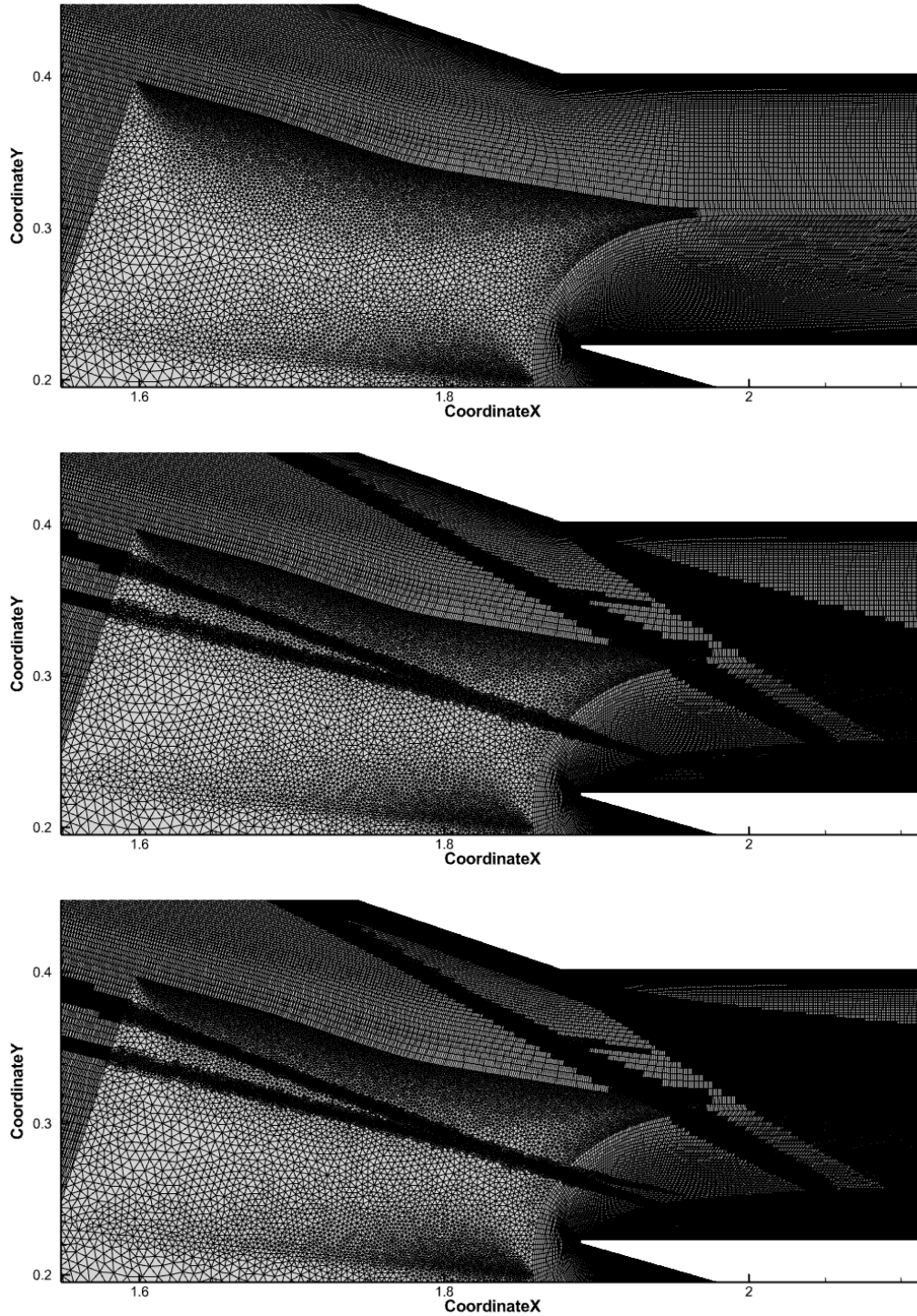


Figure 3.3 Mach contour results at 0 degrees angle of attack for the Coarse (top), Fine (middle), and Very Fine (bottom) grid resolutions.

As illustrated in Figure 3.3, the CFD results exhibit excellent agreement with the experimental data from Kotov et al. [27]. Each point identified in Figure 2.19 is clearly discernible in the CFD results, though a slight adjustment was made to the isolator length to conserve computational resources. Notably, the CFD results now distinctly reveal the flow separation and the subsonic recirculating vortex induced by the separation, as mentioned in the discussion of Figure 2.19. Removing or mitigating this vortex may prove instrumental in increasing total pressure recovery across the isolator.

Returning to the grid independence discussion, the coarse grid accurately portrays the resulting flow dynamics but lacks in shock resolution, a shortcoming addressed by the fine grid. This enhancement aligns with expectations, considering the fine grid, averaging 1.2 to 1.5 million cells, doubles the cell count of the coarse grid. The additional cells primarily contribute to improved shock resolution, evident in Figure 3.4. While subtle in Figure 3.3, the fine grid sharpens the oblique shocks and slightly adjusts their locations. In contrast, the very fine grid shows no significant deviation from the fine grid. Establishing grid independence with the fine grid would be advantageous for the current work, as the very fine grid ranges from 2.5 to 3 million cells depending on the case.

Figure 3.5 illustrates the flow comparison within the isolator at varying angles of attack. With an increasing angle of attack, the flow components remain intact but shift towards the front of the isolator while losing velocity. This trend is further quantified in the following analysis of the static pressure distribution along the upper and lower walls of the isolator.



*Figure 3.4* Mesh in front of the lower cowl at Coarse (top), Fine (middle), and Very Fine (bottom) grid resolutions. The effects of the grid adaptation are clearly visible.

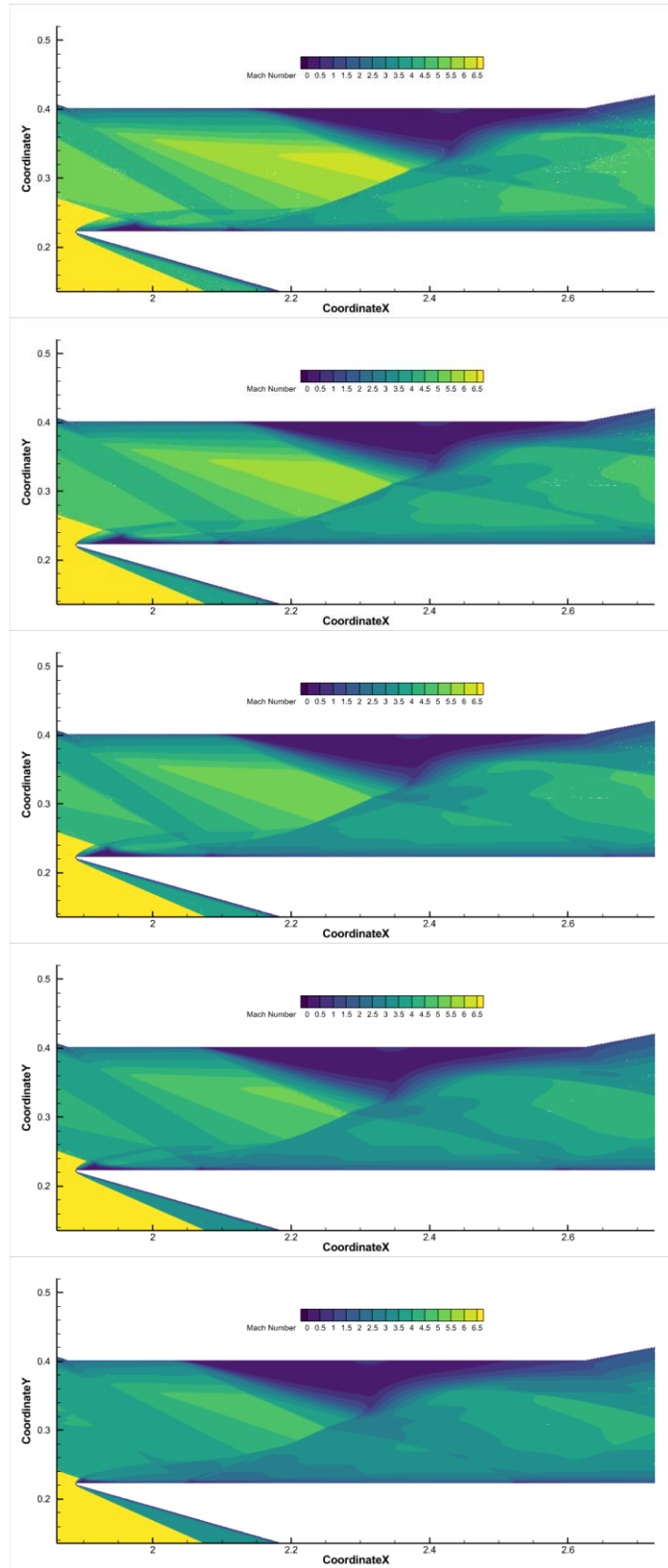


Figure 3.5 Mach contour in the isolator for 0-8 degrees (top to bottom) angle of attack.

Figure 3.6 demonstrates a marginal disparity in static pressure between the coarse and fine grid, while displaying a nearly identical alignment between the fine and very fine grid. This reaffirms grid independence at the fine grid refinement level. Notably, the increased static pressure region on the lower wall, attributed to the first shock reflection, is visible. This region, exhibiting the highest static pressure in the isolator, serves as an optimal candidate for the porous bleeder location.

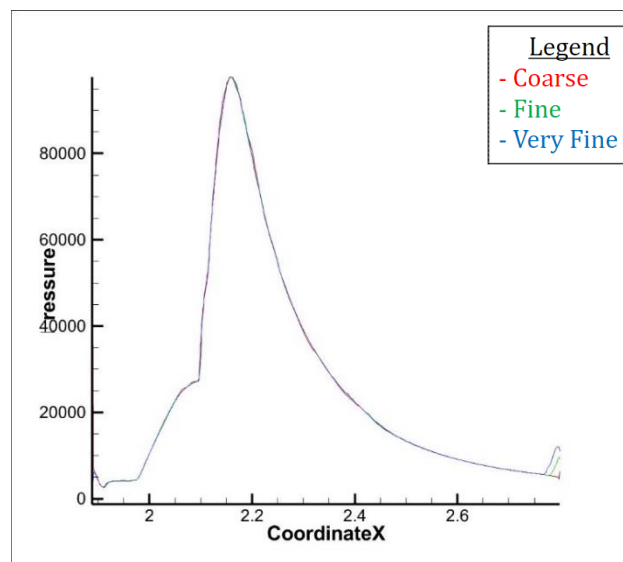


Figure 3.6 Static pressure distribution (in Pascals) on the lower isolator wall at 0 degrees angle of attack for all refinement cases.

Additionally, Figure 3.7 illustrates that with an increasing angle of attack, the high-pressure region resulting from the first reflected shock expands in size, amplitude, and moves closer towards the front of the isolator. This observation aligns with the trends identified in the Mach contours of Figure 3.5, where the reflected shock shifts forward, and the diminished velocity induces a rise in static pressure along the wall. The movement of flow components towards the front of the isolator is influenced by the inlet's increased angle of attack, effectively increasing the theta angle of the inlet wall. This in turn amplifies the beta angle of the oblique shocks generated

by the inlet wall, prompting the shock train to form earlier in the isolator. Additionally, the third reflected shock can also be seen increasing in amplitude as the angle of attack increases.

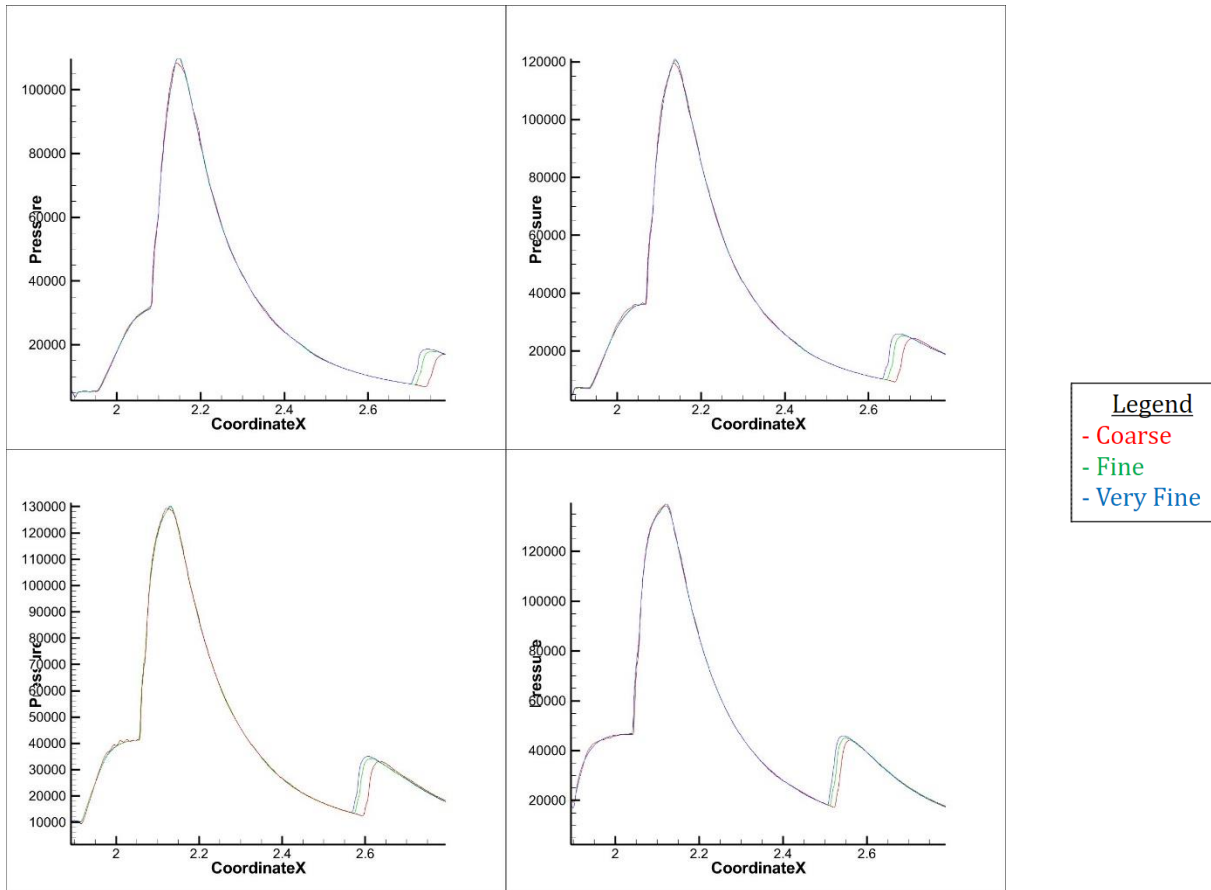


Figure 3.7 Lower wall static pressure (in Pascals) for 2 (top-left), 4 (top-right), 6 (bottom-left), and 8 (bottom-right) degrees angle of attack.

Moving on to the upper wall, Figure 3.8 once again shows a good agreement between the fine and very fine mesh. The locations of the first and second shock can be seen clearly, along with the reduction in static pressure attributed to flow separation at the isolator's onset and the resurgence of high static pressure induced by the subsonic vortex region. While this area is also a potential candidate for a porous boundary, the static pressure at this location remains considerably lower than the first reflected shock on the lower wall.

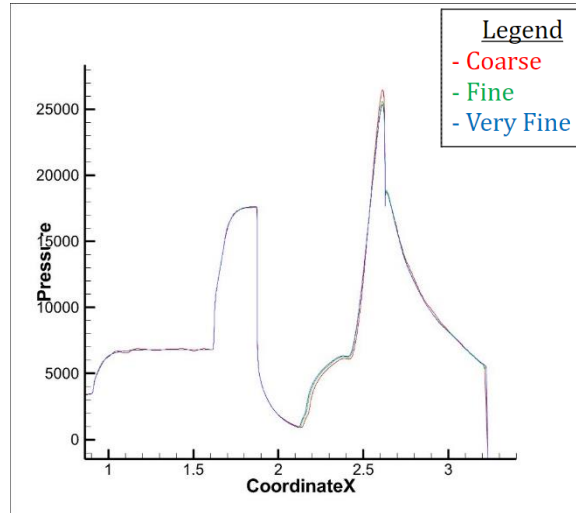


Figure 3.8 Static pressure distribution (in Pascals) on the upper isolator wall at 0 degrees angle of attack for all refinement cases.

Next, the mass flow rates (per unit meter depth) into and out of the isolator are a good indicator of mesh quality and convergence. As Table 3.2 shows, the difference between the mass flow into and out of the isolator registers in the hundredths of a percent, showing clear convergence for all cases and angles of attack. Furthermore, the difference in average mass flow rates between fine and very fine grids is in the thousandths of a percent, demonstrating grid independence at the fine grid refinement level.

Table 3.2 The mass flow rates into the isolator (referenced as the “Inlet” on the table) and out of the isolator (referenced as the “Outlet”) show good agreement with each other for every case. The mass flow rates for the fine and very fine grids display grid independence.

AoA	Coarse				Fine				Very Fine				Fine/Very Fine %Diff
	Inlet	Outlet	Average	%Diff	Inlet	Outlet	Average	%Diff	Inlet	Outlet	Average	%Diff	
0	24.97216	24.98232	24.97724	0.040677	24.97701	24.97107	24.97404	0.023785	24.97665	24.97244	24.97455	0.016857	0.002022059
2	27.97605	27.96576	27.97091	0.036788	27.96380	27.96193	27.96287	0.006687	27.96201	27.96140	27.96171	0.002182	0.004148531
4	30.93940	30.93254	30.93597	0.022175	30.92076	30.91609	30.91843	0.015104	30.91887	30.91297	30.91592	0.019084	0.008102622
6	33.84929	33.83079	33.84004	0.054669	33.83297	33.83154	33.83226	0.004227	33.83512	33.82854	33.83183	0.019449	0.001256213
8	36.71132	36.69499	36.70316	0.044492	36.70721	36.70455	36.70588	0.007247	36.70703	36.70319	36.70511	0.010462	0.002097801

These mass flow rate readings reveal an intriguing pattern: a nearly linear increase in mass flow rate with angle of attack, as depicted more vividly in Figure 3.9.

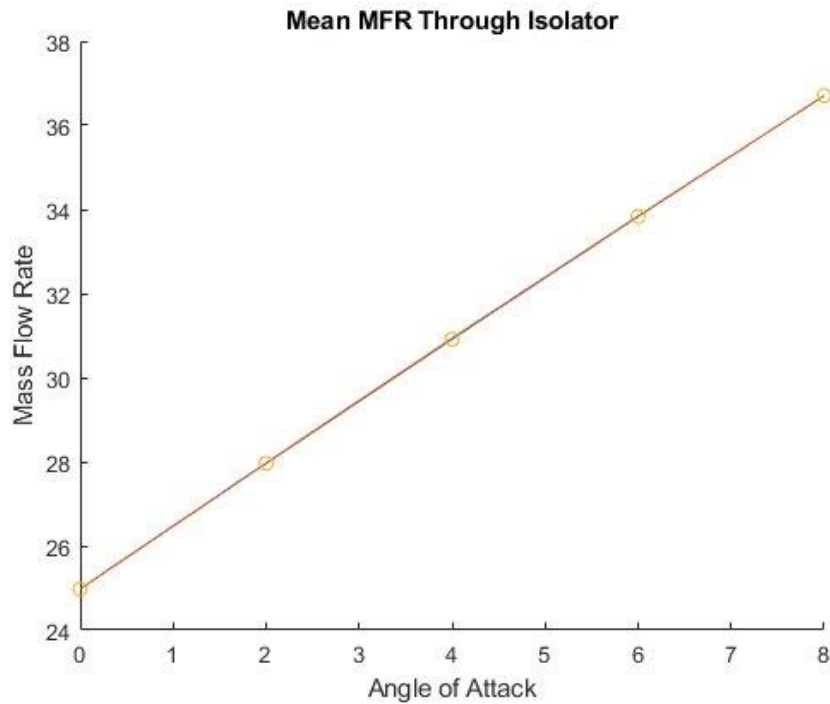


*Figure 3.9* The mass flow rate through the isolator increases linearly with angle of attack. The MFR readings for all grid refinement cases are plotted but perfectly overlap each other.

This pattern emerges because the increased angle of attack expands the effective area of the inlet. As long as the leading oblique shock intersects the lower cowl within the isolator, the mass flow rate into the scramjet rises with the expanding effective area. The area expands proportionally to the sine of the angle of attack, which, under the small angle approximation rule, is roughly equivalent to the angle of attack itself. Consequently, a linear increase in angle of attack from 0 to 8 degrees should correspond to a linear increase in mass flow rate.

Finally, the wall  $y^+$  values along the upper and lower wall surfaces, shown in Figure 3.10, consistently registered below one for all angles of attack. In certain instances, particularly along

the upper wall,  $y^+$  was significantly below one, indicating that the Mach 7 freestream velocity used for wall spacing calculations was overly conservative and could be adjusted. However, to achieve an optimized grid, grid adaptation for  $y^+$  is necessary. The substantial range of  $y^+$  values along both upper and lower isolator surfaces implies that a universal solution would be computationally inefficient.

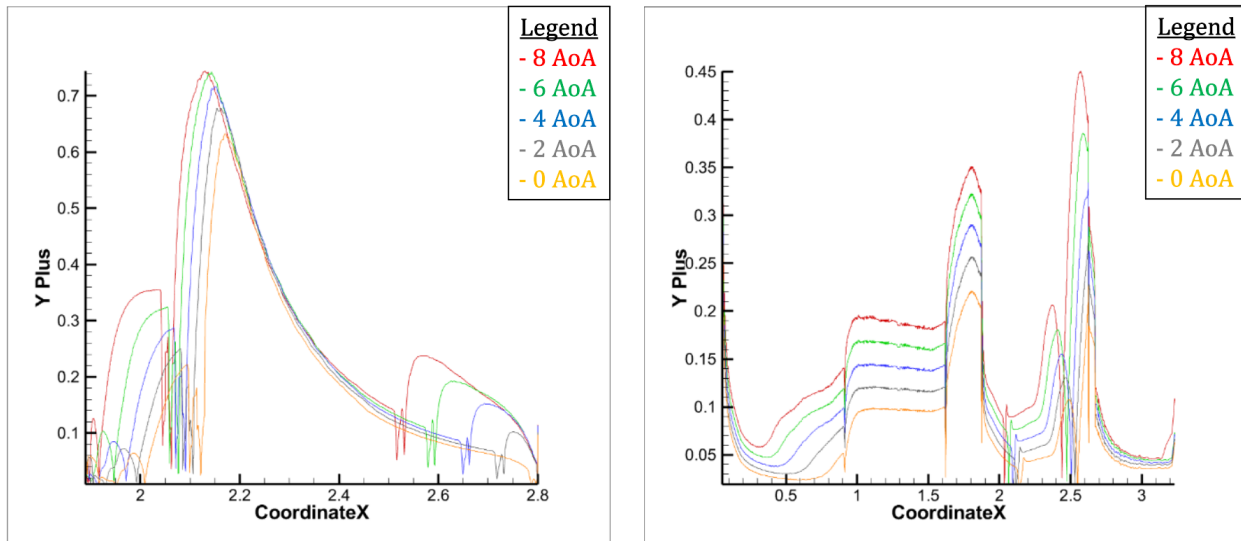
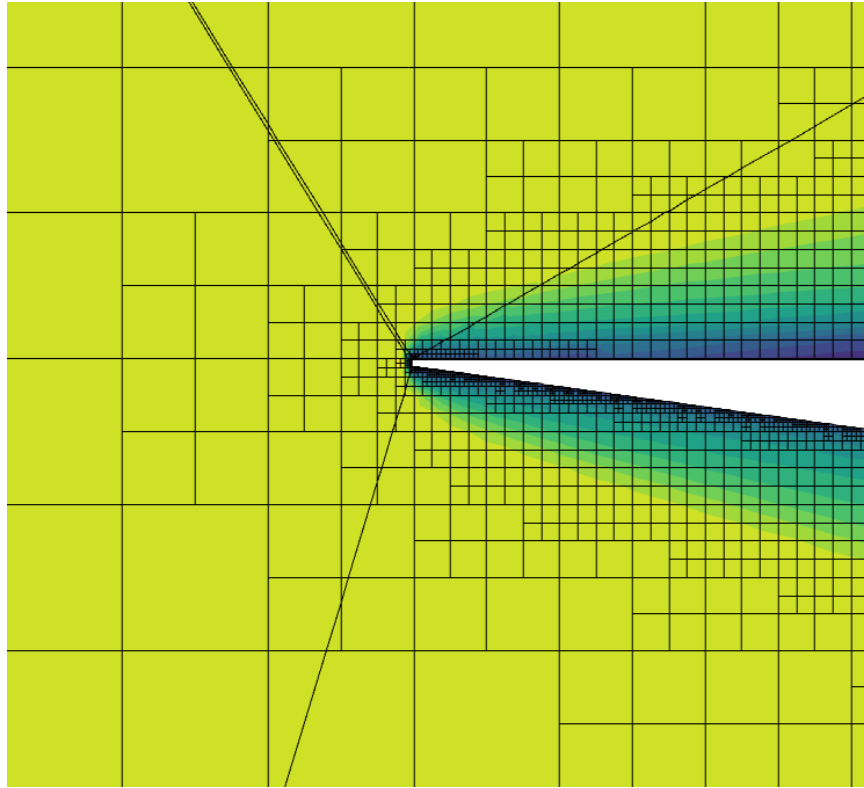


Figure 3.10 Wall  $y^+$  values for the lower (left) and upper (right) wall surfaces.

### 3.2 Converge CFD Software

Despite the excellent matching of CFD results obtained with Fluent to experimental data, it would be beneficial to cross-verify these results using another CFD program. Converge CFD [33] was chosen for this purpose due to its unique ability to dynamically generate meshes during runtime based on given boundary conditions. This feature simplifies case setup and execution, as it requires less time for mesh creation. Instead of manually designing a mesh, as shown in Figure 3.11 Converge is provided with settings to generate its mesh dynamically, using active mesh adaptation to meet specified requirements, making it an ideal candidate for this study.



*Figure 3.11* Converge CFD automatically generates a mesh and adapts it during runtime according to given instructions. Here, the many cells created near the wall to achieve a  $y^+$  of one are visible.

Unfortunately, issues were immediately encountered with cases tested in Converge. Steady-state cases proved unrunnable, despite multiple adjustments to settings. Resorting to a transient solver allowed the case to run, but with a substantial increase in the time required to reach a solution. Additionally, this case lacked a viscous solver and assumed inviscid flow, producing an unrealistic solution which saw the lack of any flow separation, displayed in Figure 3.12.

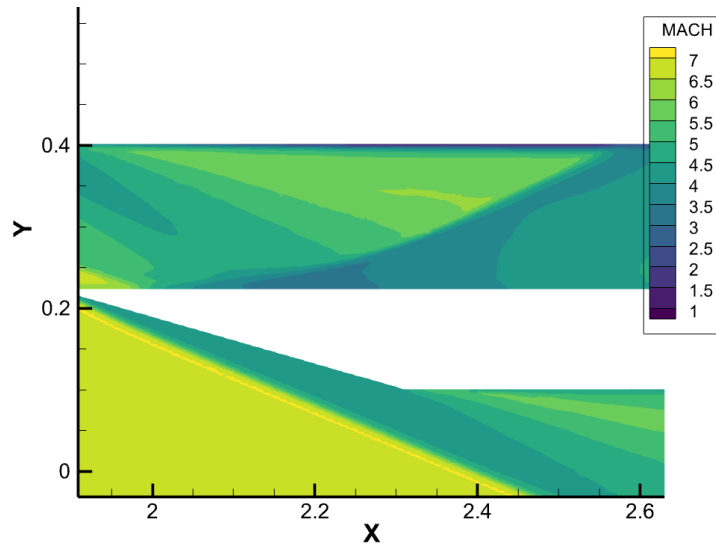


*Figure 3.12* While proper expansion is visible, this case does not have flow separation and the associated subsonic vortex.

Upon introducing a viscous model with the transient solver, the subsonic vortex caused by flow separation reappeared. However, despite numerous cases tested with varying settings, each case exhibited its unique shortcomings. Examples of these issues are illustrated in Figure 3.13, Figure 3.14, and Figure 3.15. Furthermore, when viscous equations were introduced, the freestream temperature would inexplicably increase by a range of anywhere from 2 K, which was undesirable, to 40 K, which was catastrophic. This temperature increase in the freestream would lower the Mach number, leading to different results.

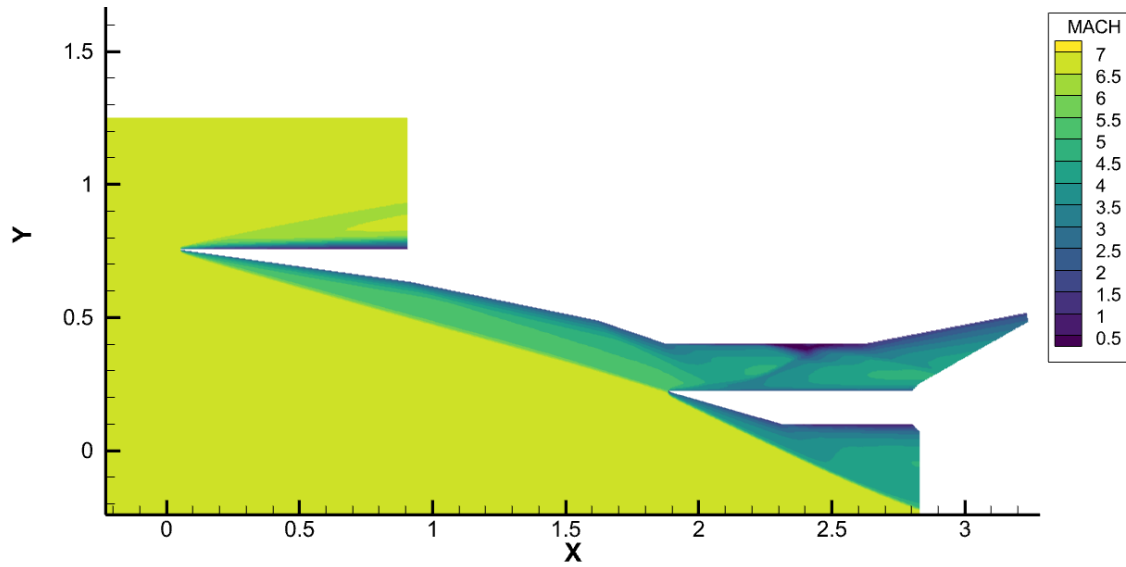


Figure 3.13 Introducing viscous equations reintroduces flow separation but increases freestream temperature, lowering the freestream Mach number. Improperly formed oblique shocks are also visible.

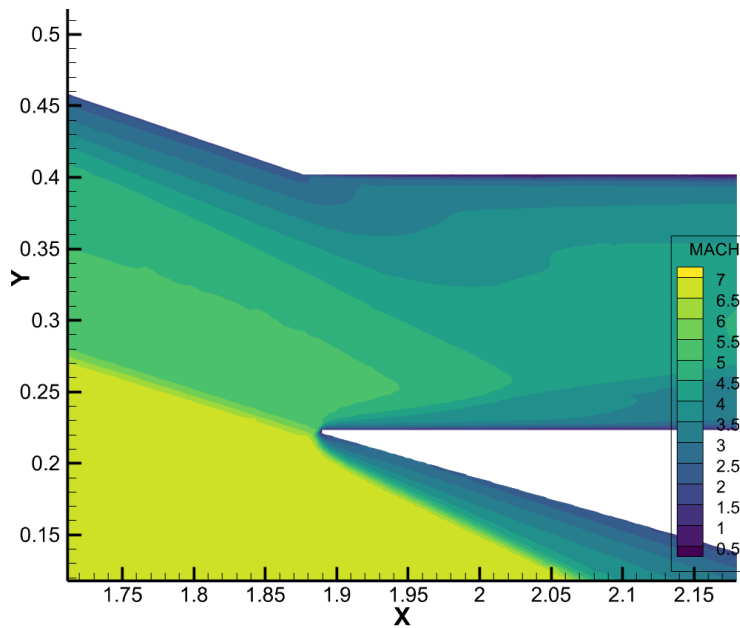
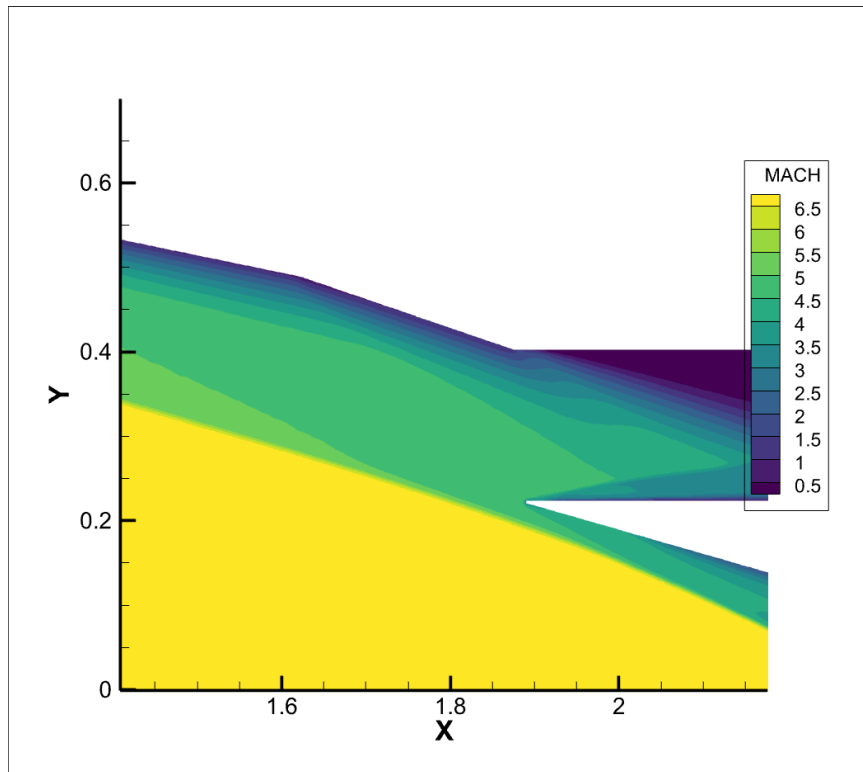


Figure 3.14 A closeup of the isolator section; the expansion fan is not properly formed at the top of the isolator, and the improperly formed oblique shocks have reached the lower cowl much farther forward than anticipated.



*Figure 3.15* Flow separation has occurred much earlier in this case and the bow shock has now moved so far forward that it missed the lower cowl entirely.

While Converge's automatic mesh adaptation demonstrated its capability in meeting various requirements, such as achieving a wall  $y^+$  of one throughout the isolator, it was hypothesized that the failure of the Converge test cases stemmed from its solvers. The available solvers, a modified simple and PISO scheme, were pressure-based and known to lose accuracy beyond Mach 0.3 when air becomes compressible. Despite the modifications made to the solvers, this issue proved to be too big of an obstacle for this Mach 7 case.

### **3.3 Improved Unstructured Mesh Creation**

Despite the setback with Converge, it was evident that a new mesh was necessary for further progress. The primary concern with the initial Fluent mesh was the excessively small wall spacing implemented to achieve a wall  $y^+$  of less than one for a Mach 7 case. This minute wall

spacing resulted in horizontally skewed cells along the wall, which would extend into vertically skewed cells as they moved away from the wall. The vertical skew was relatively inconsequential, with a maximum aspect ratio of about 1.5 to 1. However, the horizontal skew reached a maximum aspect ratio of 2,000 to 1. While this high aspect ratio did not hinder the case from running and producing good results, it proved problematic during attempts at mesh refinement in these cells.

Initially, attempts were made to refine the mesh based on density, pressure, and temperature parameters. However, temperature-driven refinement predominantly impacted the highly skewed cells along the wall, leading to consistent run failures. To address this, the temperature parameter was removed from the refinement criteria, and specific region conditions were implemented to prevent adaptation of cells along the wall. This approach was deemed unacceptable for a case involving a future porous boundary condition that would require refinement along a wall.

The solution involved generating an unstructured mesh and using Fluent's automatic adaptation for optimal mesh creation, similar to the Converge approach. Freed from structured mesh constraints, this method provided greater control over spacing and connectors, allowing strategic cell placement in crucial regions. Fluent's automatic adaptation then added cells along shocks and the wall to achieve a  $y^+$  of one. This approach demonstrated enhanced robustness and efficiency, with a starting grid of only 157,000 cells (less than a quarter of the initial mesh's coarse grid).

The improved grid underwent testing at a 0 degree angle of attack case, following a similar process to the initial grid refinement. Notably, during the fine and very fine grid stages, the mesh underwent active adaptation every 100 iterations, as opposed to a single refinement. The fine grid ultimately comprised 1.36 million cells, aligning with the initial mesh's fine grid despite starting

from different coarse grid cell counts. However, the very fine grid culminated in an excessive 10 million cells—a considerable increase in cell count. A comparison between the new and old meshes at the fine refinement level is depicted in Figure 3.16, and Figure 3.17 illustrates the comparison between the three grid refinement levels of the unstructured mesh in the isolator.

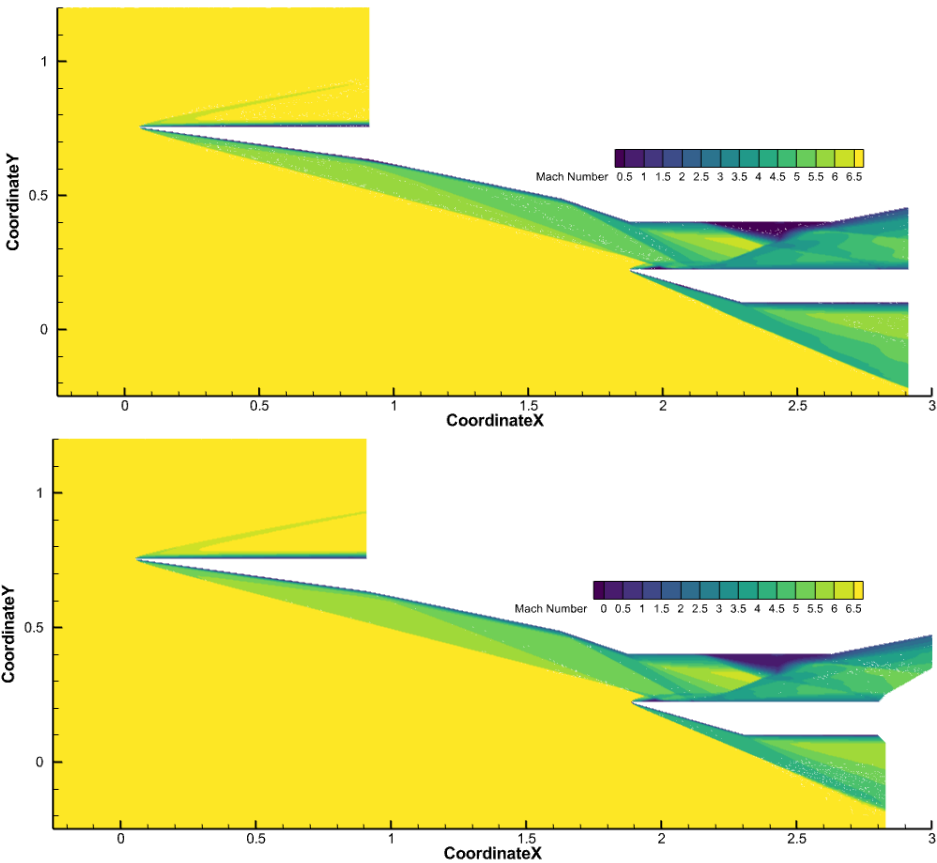


Figure 3.16 Comparison between new (top) and old (bottom) Mach contours at 0 degrees angle of attack and fine refinement level.

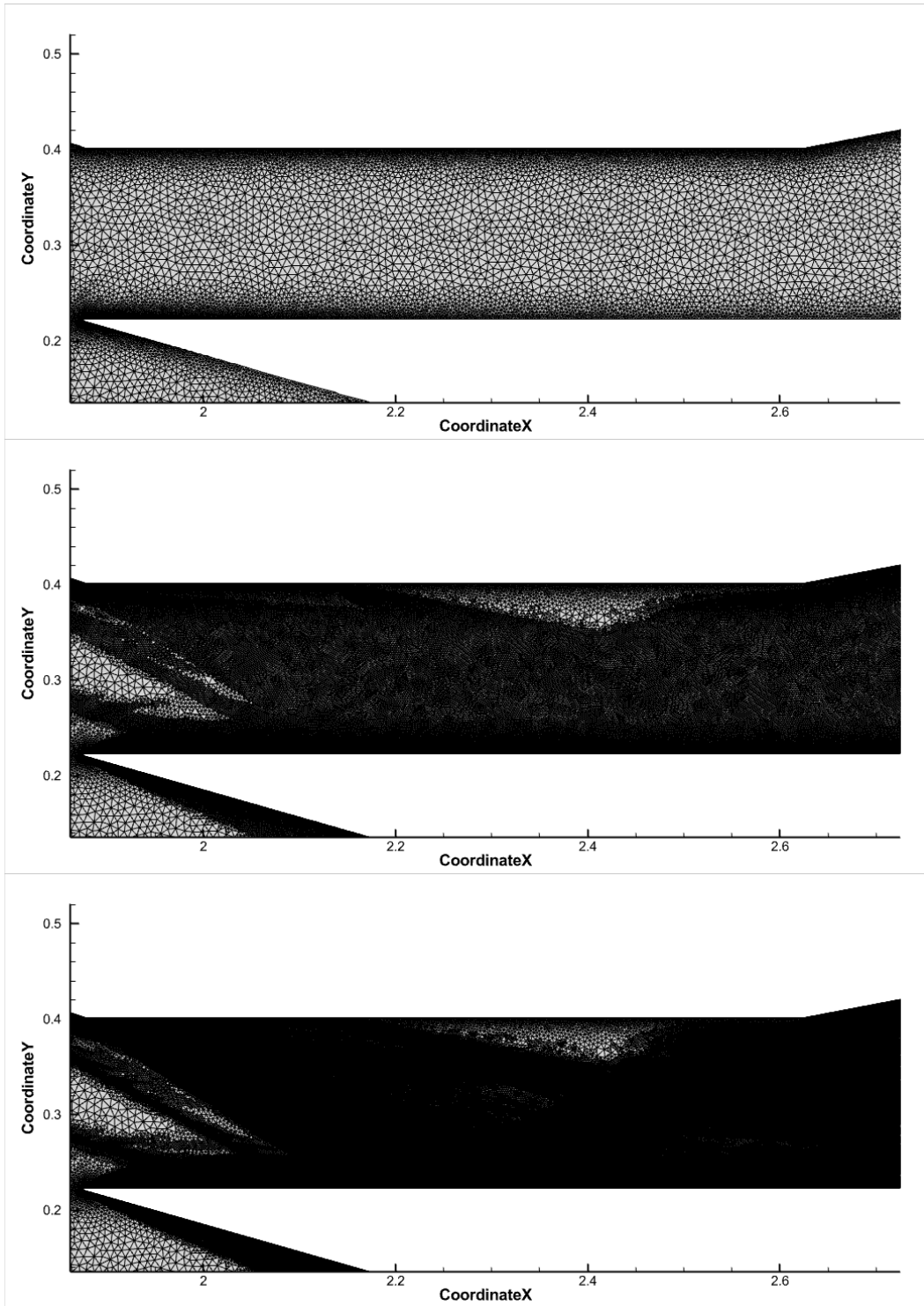
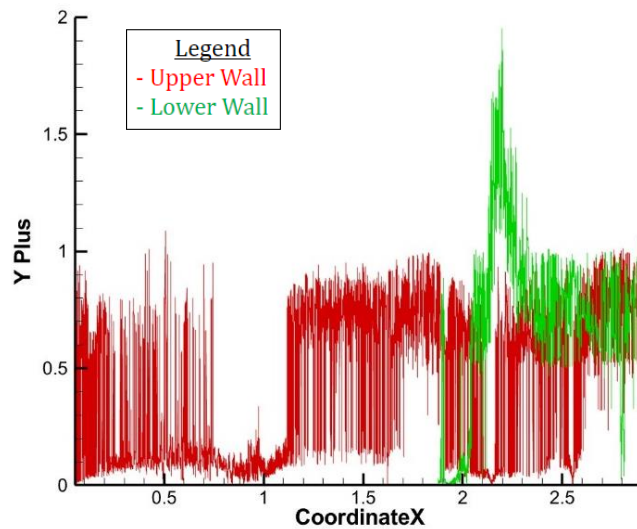


Figure 3.17 Unstructured mesh comparison in the isolator region for the Coarse (top), Fine (middle), and Very Fine (bottom) refinement levels. The very fine mesh did not introduce new cells in different locations; rather, it significantly increased the density of existing refined cells.

The fine mesh strategically added cells to accurately capture shocks and varying density, while also incorporating more cells along the wall to satisfy the wall  $y^+$  requirement of one. A notable difference in Figure 3.16 is the presence of improperly formed oblique shocks below the lower cowl on the new mesh. This result stems from the absence of  $y^+$  adaptation, a deliberate choice to conserve computational resources in an area deemed unimportant for this study. Nonetheless, this emphasizes the need for successful achievement of a low  $y^+$  value within the isolator, as evidenced in Figure 3.18.



*Figure 3.18* Wall  $y^+$  values for the upper and lower isolator wall. The maximum  $y^+$  is 2, which is still well within an acceptable range.

Additional improvements made include flattening the end of the mesh by lengthening the isolator portion as well as rounding the tips of the leading edges of the lower cowl and bow, which were previously cut flat. This specific improvement is detailed in Figure 3.19, depicting the comparison of lower cowl shock formations at different grid refinement levels.

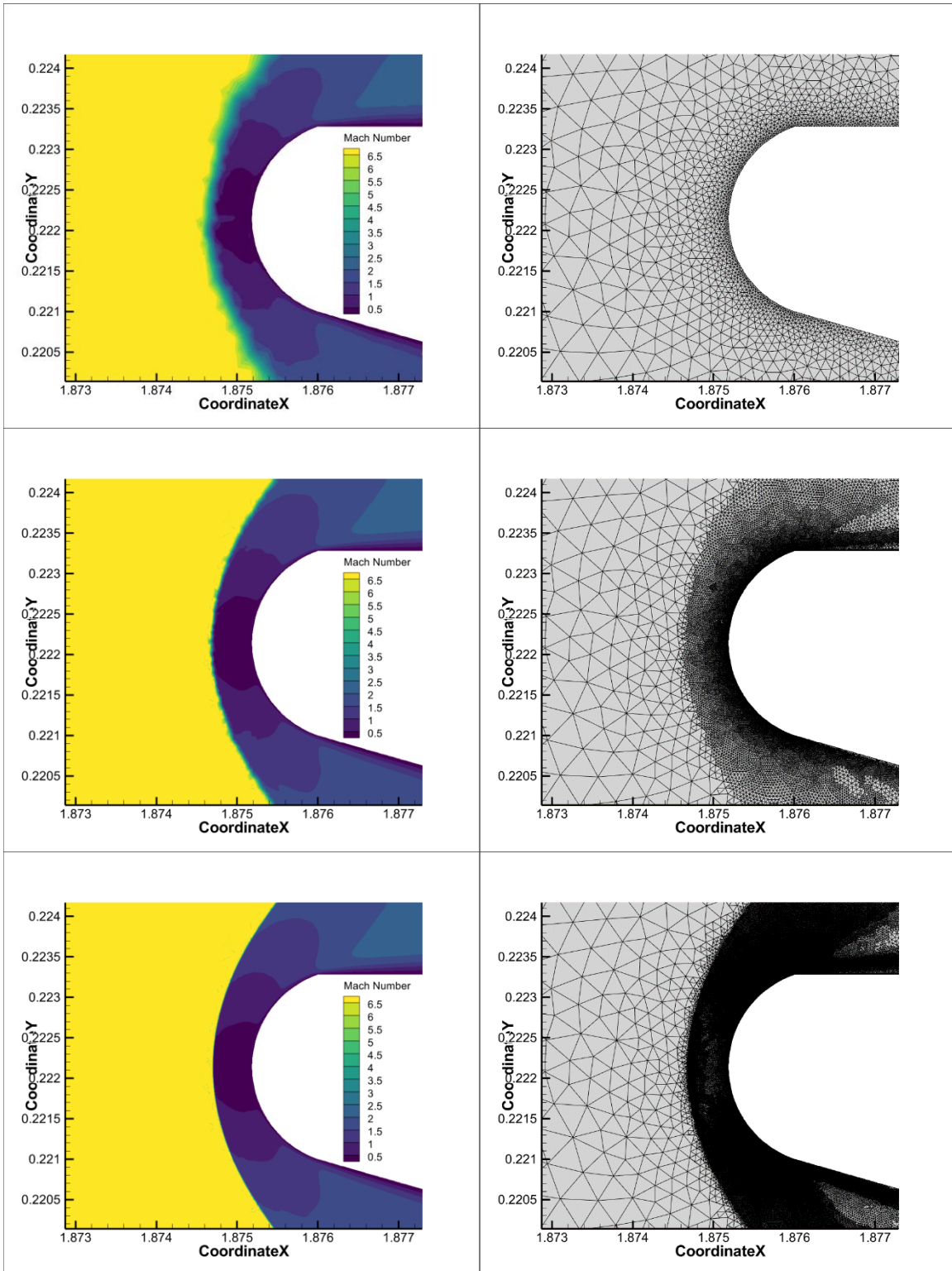
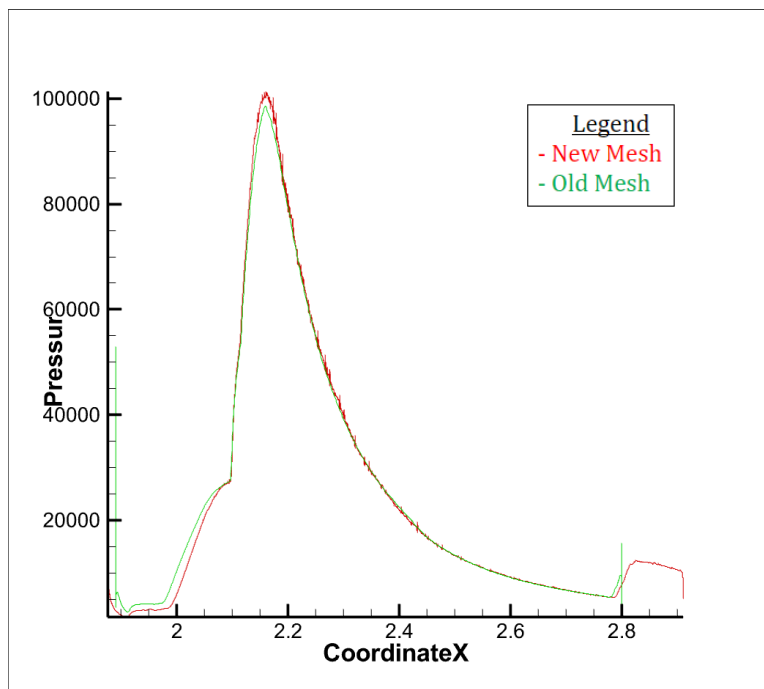


Figure 3.19 Mach contour and mesh comparison at the lower cowl leading edge for the Coarse (top), Fine (middle), and Very Fine (bottom) mesh refinement levels. The very fine refinement achieved shock resolution in the order of micrometers. While visually satisfying, it did not sufficiently change the actual data to justify having nearly eight times as many cells.

Lastly, the mass flow rate through the new isolator closely matched that of the old mesh, with a deviation of only 0.1%, and the difference in mass flow rate between the fine and very fine mesh once again measured in the hundredths of a percent. The static pressure distribution for the fine refinement level for the new and old mesh is shown below in Figure 3.20. It shows a near identical pressure distribution, with a slight variation at the very front of the isolator attributed to the more proper formation of the shock resulting from the improved rounding of the leading edge of the lower cowl. This fix is also the likely reason for the slightly higher maximum static pressure on the new mesh compared to the old mesh.



*Figure 3.20* Lower isolator wall static pressure distribution comparison between the new and old mesh at the fine grid refinement level.

### 3.4 Ideal Lower Cowl Locations

The schematics given in Figure 2.16 depict a lower cowl edge that aligns vertically with the beginning of the isolator. However, as observed in the experimental results of Figure 2.18, this alignment does not correspond to the optimal position for the lower cowl in reality. The lower cowl's placement should vary with the angle of attack, ensuring that the bow shock meets just above the leading edge of the lower cowl. This arrangement ensures that all the captured inlet flow enters the isolator while preventing excess freestream from impacting flow dynamics. At higher angles of attack, an improperly positioned lower cowl could potentially induce flow separation at the lower wall and increase drag.

Now that an adequate mesh has been created and validated, the ideal lower cowl location for each angle of attack can be determined. This was achieved by using the base cases to estimate where the bow shock would intersect with the lower cowl at each angle of attack, then testing four lower cowl locations for each angle of attack to identify the optimal position. Table 3.3 presents the ideal lower cowl location for each angle of attack obtained through this method, and Figure 3.21 illustrates an example of the four lower cowl locations tested at 0 degrees angle of attack.

*Table 3.3* Lower cowl location for each angle of attack.

AoA	Lower Cowl X Coordinate (mm)
0	2008
2	1996
4	1970
6	1942
8	1918

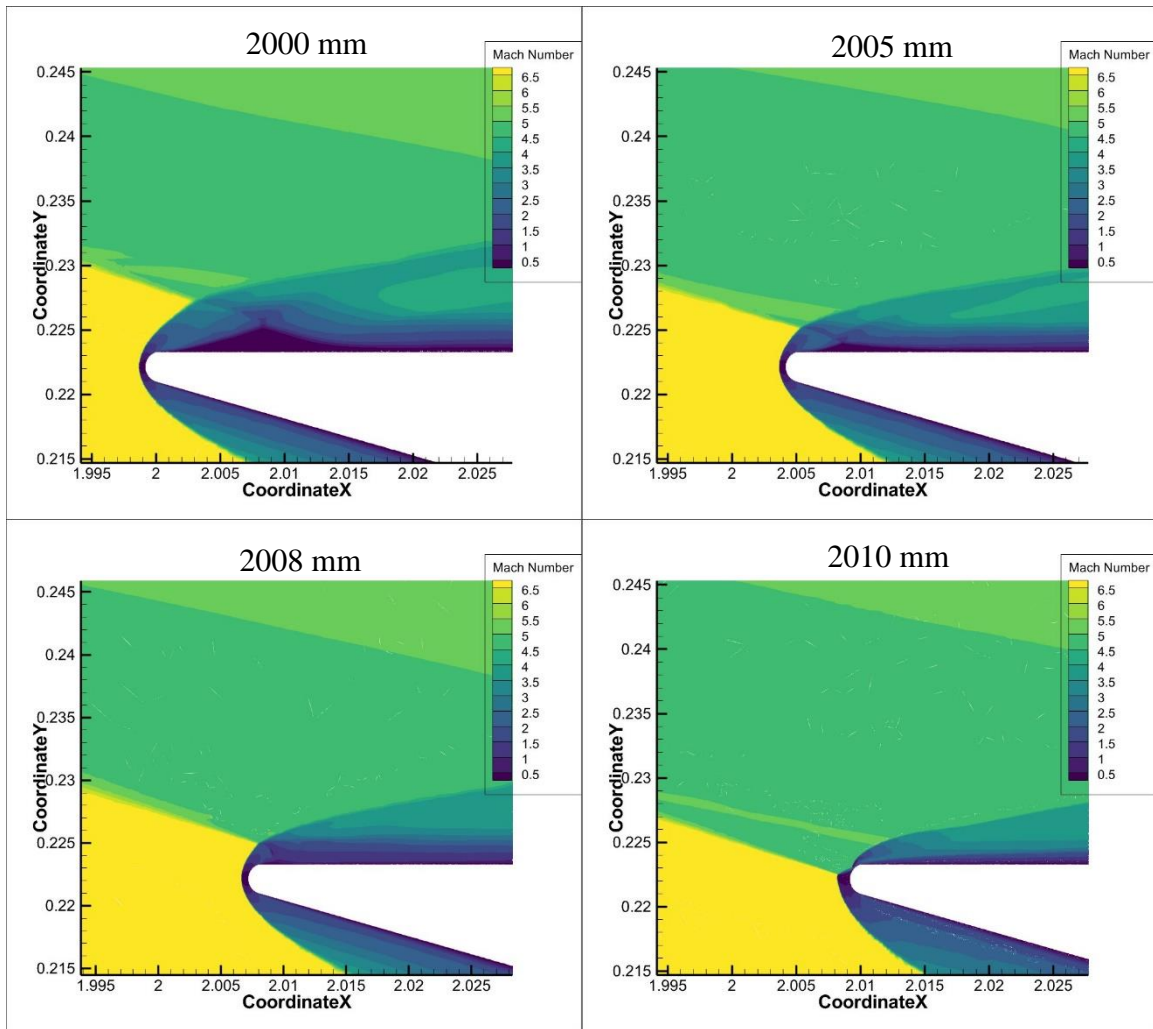


Figure 3.21 Mach contour comparison of four lower cowl locations for 0 degree angle of attack.

In the 0 degree angle of attack case shown in Figure 3.21, the optimal location for the lower cowl was determined to be at 2008 mm. The 2010 mm case showed the bow shock narrowly missing the top of the lower cowl and interfering with the shock formed by the lower cowl's leading edge. An additional scenario was explored with the 2010 mm location, this time using the standard  $k-\omega$  SST model for the viscous solver. Despite the anticipation of minimal alterations due to the high Reynolds number associated with this case, unexpected changes were observed, as depicted in Figure 3.22.

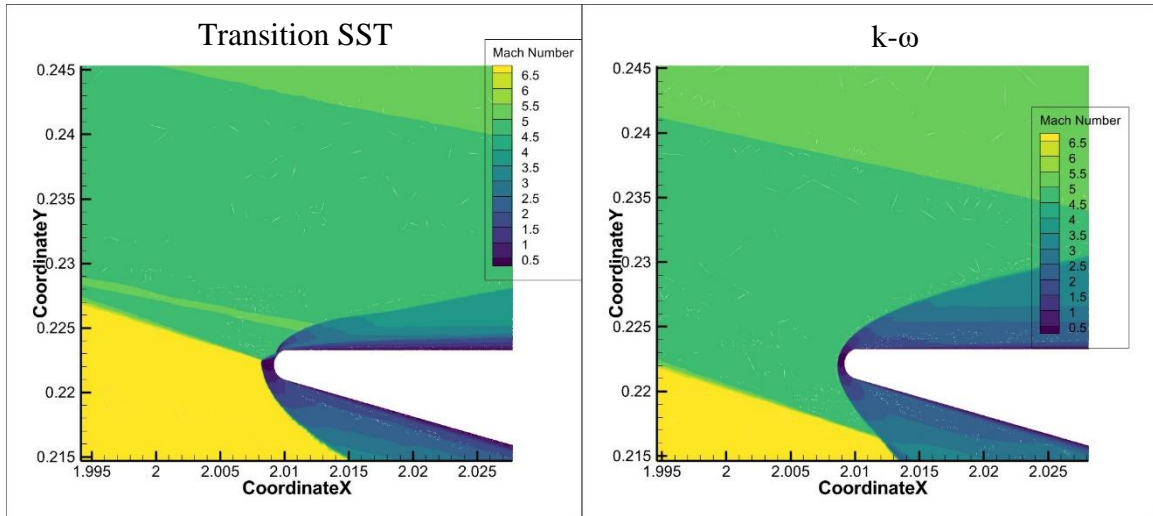


Figure 3.22 Mach contour at 0 degrees angle of attack comparing the results of Transition SST (left) to k- $\omega$  SST (right).

Figure 3.22 reveals a significant deviation in results as the k- $\omega$  SST model causes the bow shock to bypass the lower cowl entirely and travel beneath it. This prompted further investigation with additional viscous solvers, this time using the same freestream conditions as the HAST facility. As illustrated in Figure 3.23, using the previously determined optimal location of 2008 mm for the 0 degree angle of attack case, the Spalart-Allmaras and k- $\epsilon$  models exhibited notable variations and were removed from consideration. Surprisingly, the Transition SST model and the k- $\omega$  model yielded identical results in this instance, unlike their divergent outcomes in the previous case. The cause of this is unknown, but may be connected to a difference in freestream conditions between the two cases. Despite the unresolved discrepancy between the two models, the more intricate Transition SST model was selected for subsequent analyses over the faster k- $\omega$  model.

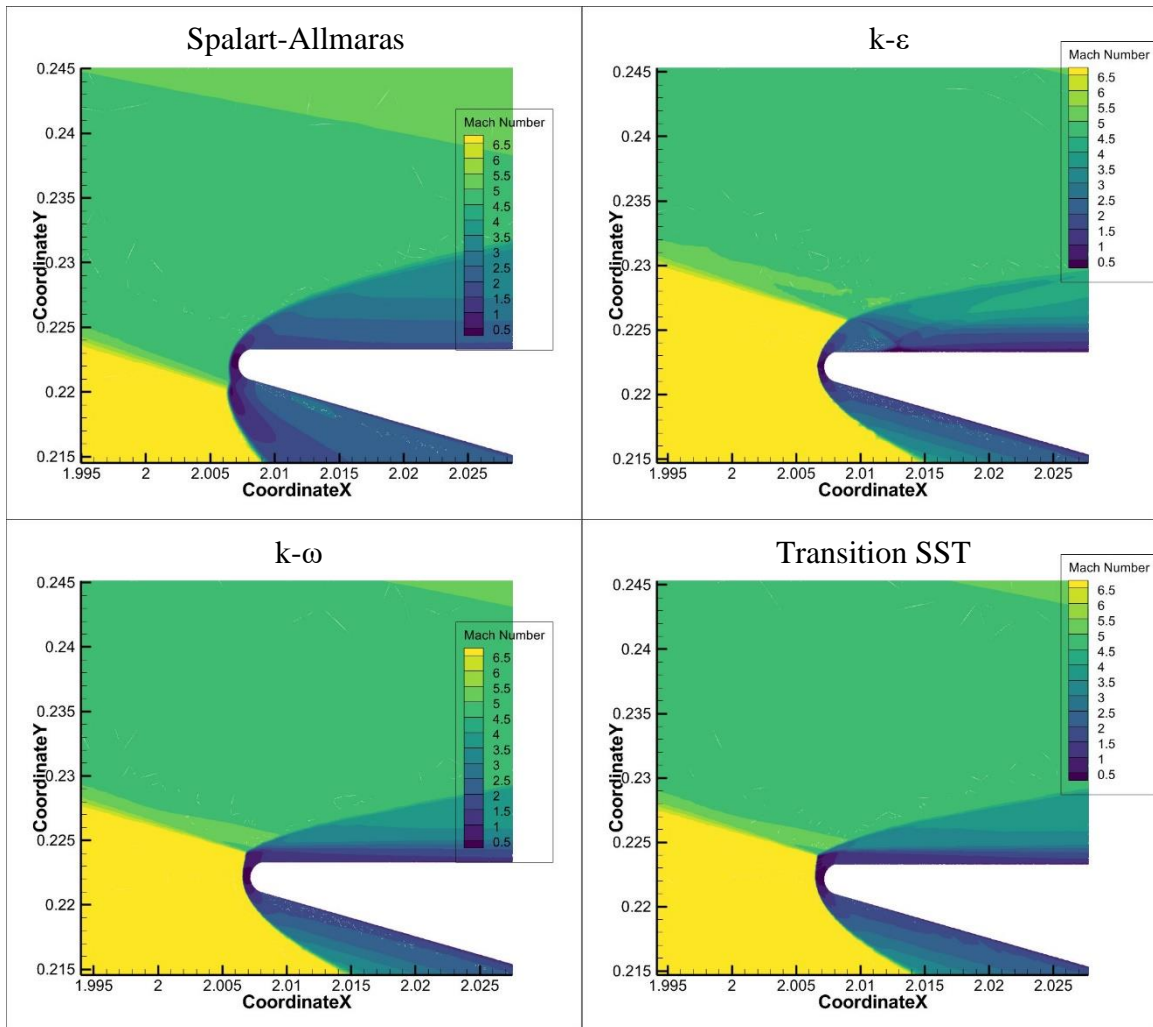


Figure 3.23 Comparison of four different viscous solvers at 0 degrees angle of attack for the 2008 mm lower cowl location.

With the validation of the mesh, determination of ideal lower cowl locations for various angles of attack, and finalization of CFD settings, the foundational basis for the current work has been laid and experimentation with porous bleeder implementation can commence.

## **4 Porous Bleeder Implementation Results & Discussion**

In this chapter, the porous bleeder is finally integrated into the scramjet engine model. Slight modifications were made to the previously validated mesh to accommodate the bleeder, and a series of simulations were conducted across varying angles of attack, each comprising five cases with differing bleed amounts. A qualitative examination of airflow dynamics within the isolator follows, showcasing the fundamental impact of the bleeder. Delving into quantitative analysis, a method is developed to discern bleeder effectiveness for different angles of attack and bleeder conditions.

Further experimentation explores unstart prevention. Using the mechanical blockage method, additional cases were conducted at 0, 4, and 8 degrees angle of attack, each subjected to varying levels of increased back pressure in an effort to force unstart to occur. This process showcased key features of the unstart phenomenon but also assessed the bleeders' potential in mitigating such scenarios.

### **4.1 Porous Modeling**

In preparation for the experiments involving porous bleeders, a decision was necessary regarding the modeling approach for their implementation. Initially, deliberation centered on the selection of a suitable porous bleeder boundary condition. Despite various options available from prior research, they were ultimately dismissed for several reasons. Firstly, the primary objective of the current work focused on controlling specific mass flow rates through the bleeder to analyze their impact on flow dynamics, rather than precisely replicating real world bleeders. The adoption and alteration of more intricate porous conditions that are more stringent in their modeling could have introduced implementation challenges and heightened the risk of computational instability.

Given overarching concerns regarding computational stability throughout the simulations, unnecessary complications were circumvented if possible.

Additionally, the porous conditions under consideration were tested at supersonic speeds, falling below the hypersonic range relevant to the present work. Although prior studies had demonstrated promising outcomes at lower speeds, uncertainties persisted regarding their viability under hypersonic conditions.

The location chosen for the porous bleeder was along the lower wall of the isolator, precisely where the reflected shock elevated the static pressure to its peak within the isolator. The porous bleeder, discussed in the following paragraph regarding its boundary condition modeling, was positioned at the point of highest static pressure and assessed at 0 degrees angle of attack. Three different sizes of the porous bleeder were trialed: 40mm, 80mm, and 200mm. However, it became evident that the 80mm size was optimal. The 40mm bleeder demonstrated negligible effect on reducing static pressure along the lower wall, while the 200mm bleeder extracted an excessive amount of air from the isolator, rendering it unsuitable.

Initially, attempts were made to regulate the mass flow exiting the bleeder using a mass flow outlet boundary condition and a pressure outlet with a targeted mass flow rate. However, it was soon discovered that neither of these approaches were effective, as flow over the bleeder during regular isolator operating conditions remained supersonic at all times. This resulted in runtime errors, as Fluent was unable to establish an external pressure on the boundary for backward extrapolation—a scenario impossible in supersonic flow.

Subsequently, Fluent's built-in porous jump boundary condition was implemented. This condition defines the pressure change using a modified form of the Darcy's Law equation, as illustrated in Eq. 4.1.

$$\Delta p = -\left(\frac{\mu}{\alpha} v + C_2 \frac{1}{2} \rho v^2\right) \Delta m \quad (4.1)$$

In this equation,  $\mu$  represents the laminar fluid viscosity,  $\alpha$  denotes the permeability of the medium,  $v$  stands for the velocity normal to the porous face,  $C_2$  signifies the pressure jump coefficient, and  $\Delta m$  indicates the thickness of the medium. Fluent's default settings for the porous jump condition established  $\alpha$  to an arbitrarily high value to nullify the first term, which remained unaltered for the experimental cases. Various test cases were conducted which altered the value of  $\alpha$  to smaller and smaller values in an attempt to reintroduce the effects of this first term, but no discernable change was noticeable in any of these tests.

For all simulations using a porous boundary condition,  $\Delta m$  was designated as 1 inch, equivalent to 0.0254 m. This parameter rendered the pressure change, and subsequently the mass flow rate through the bleeder, solely reliant on the pressure jump coefficient  $C_2$ . Adjusting  $C_2$  provided control over the amount of air extracted from the isolator.

Following numerous iterations, five distinct  $C_2$  values were selected for testing at every angle of attack: 0, 100, 250, 500, and 1,000. These choices aimed to provide a broad spectrum of mass flow rates, although the range was constrained by practical considerations. For instance, a  $C_2$  coefficient of 0 implies a non-existent porous condition akin to a pressure outlet, thereby limiting the maximum mass flow rate solely by the bleeder size at each angle of attack.

Conversely, while theoretically, the pressure jump coefficient could be further elevated to reduce mass flow rates, a  $C_2$  of 1,000 already approached the upper bounds of reasonability. Notably, several instances tested with a  $C_2$  of 1,000 resulted in numerical instability which necessitated active adjustments during runs, such as Courant number variations, to manage. Even post-convergence these cases exhibited higher percentage errors compared to runs with lower

pressure jump coefficients, thus imposing limitations on the minimum mass flow rate through the bleeder.

The mass flow rate outcomes for all tested cases are summarized in Table 4.1. Calculated percent errors, derived from contrasting the bleeder flow rate against the disparity in flow rates between the inlet and outlet, generally fell within acceptable thresholds, with three exceptions noted previously. The lowest bleed amount was 10.67%, which was higher than predicted for a minimum value.

As the angle of attack rose, the static pressure along the lower wall correspondingly increased, as evident in Figure 4.1. To compensate for this trend, the length of the porous bleeder was adjusted to encompass the segment along the lower wall surpassing 80,000 Pascals of pressure. Details regarding the porous bleeder sizes for all angles of attack are presented in Table 4.2.

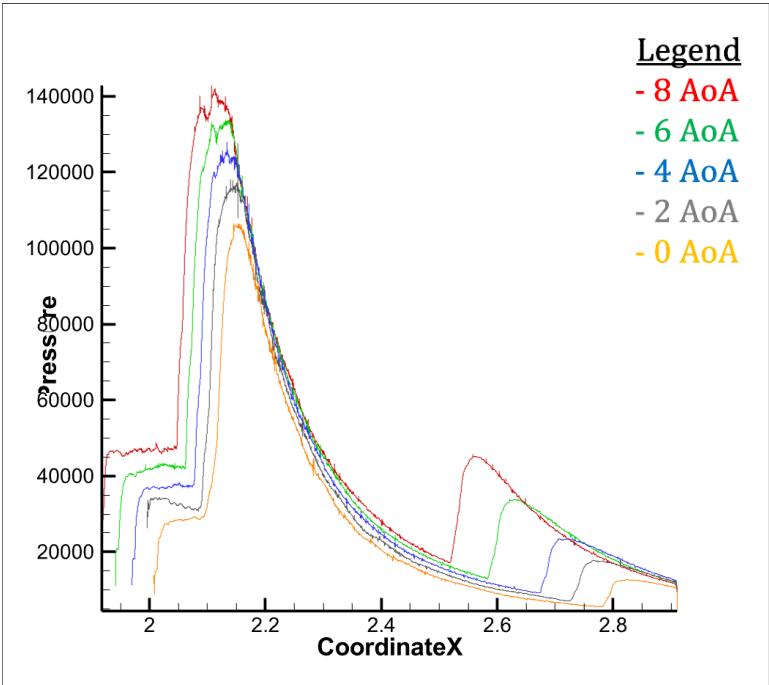


Figure 4.1 Lower wall static pressure at all angles of attack.

Table 4.1 Mass flow rate readings for all cases tested with porous bleeders.

AoA	C2	Inlet	Outlet	Bleeder	%Error	Bleed%
0	0	24.963	19.373	5.615	0.447	22.49
	100	24.970	20.450	4.521	0.022	18.11
	250	24.979	21.158	3.820	0.026	15.29
	500	24.982	21.697	3.256	0.883	13.03
	1000	24.953	22.282	2.662	0.337	10.67
AoA	C2	Inlet	Outlet	Bleeder	%Error	Bleed%
2	0	28.110	21.582	6.542	0.214	23.27
	100	28.116	22.912	5.239	0.673	18.63
	250	28.148	23.698	4.468	0.404	15.87
	500	28.102	24.293	3.794	0.394	13.50
	1000	28.100	24.944	3.151	0.158	11.21
AoA	C2	Inlet	Outlet	Bleeder	%Error	Bleed%
4	0	31.173	22.372	8.804	0.034	28.24
	100	31.173	24.110	7.052	0.156	22.62
	250	31.189	25.113	6.058	0.296	19.42
	500	31.181	26.009	5.223	0.986	16.75
	1000	31.181	27.281	4.004	2.667	12.84
AoA	C2	Inlet	Outlet	Bleeder	%Error	Bleed%
6	0	34.044	23.874	10.261	0.895	30.14
	100	34.023	25.834	8.201	0.147	24.10
	250	34.074	27.026	7.083	0.497	20.79
	500	34.132	27.979	6.098	0.894	17.87
	1000	34.121	29.104	5.103	1.714	14.96
AoA	C2	Inlet	Outlet	Bleeder	%Error	Bleed%
8	0	36.899	25.677	11.188	0.303	30.32
	100	36.886	27.854	9.000	0.354	24.40
	250	36.888	29.094	7.783	0.141	21.10
	500	36.895	30.109	6.739	0.693	18.27
	1000	37.113	31.269	5.628	3.696	15.16

*Table 4.2* Porous bleeder start and end locations for all angles of attack.

AoA	Bleeder Start Location (mm)	Bleeder End Location (mm)
0	2120	2200
2	2110	2200
4	2090	2210
6	2070	2210
8	2060	2210

As anticipated, elevating the angle of attack results in a higher intake of air into the isolator which increases the porous bleed air. However, as depicted in Figure 4.2, normalizing the bleed air by the incoming inlet air reveals that the overall proportion of air vented through the porous bleeder escalates with increasing angles of attack for each designated pressure jump coefficient. This is an expected outcome of increasing the porous bleeder size with angle of attack and explains the non-linearity in the increase in bleed percentage. Nevertheless, this effect did not lead to a reduction in the airflow passing through the isolator compared to equivalent pressure jump coefficients at lower angles of attack. Overall, increasing the angle of attack induces a greater airflow through the isolator for a given porous boundary condition, provided unstart does not occur.

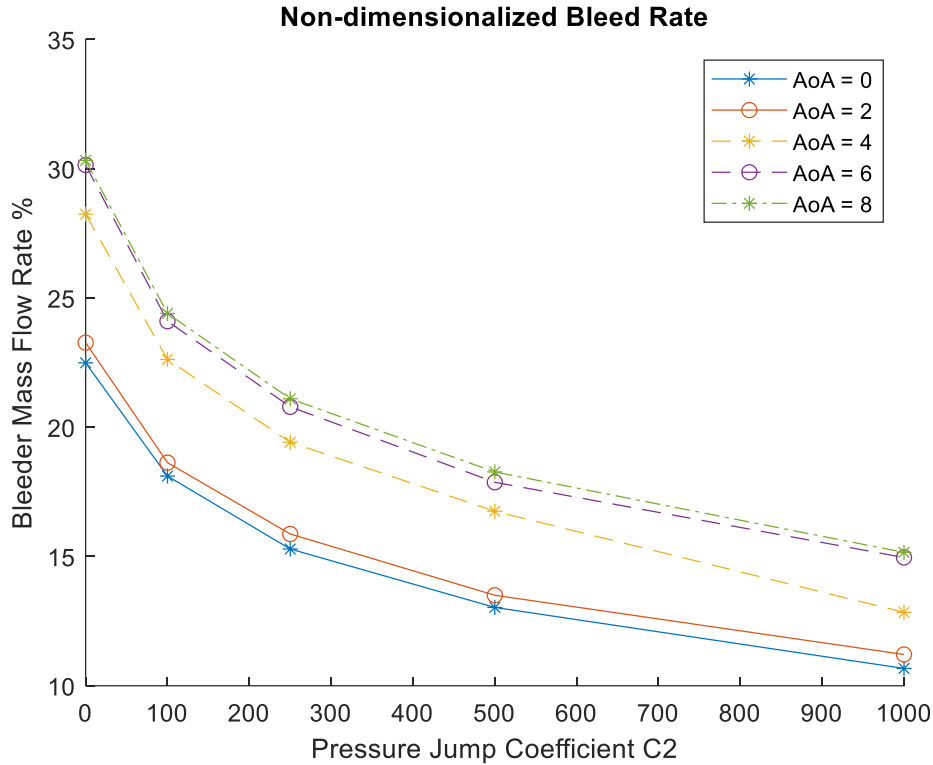
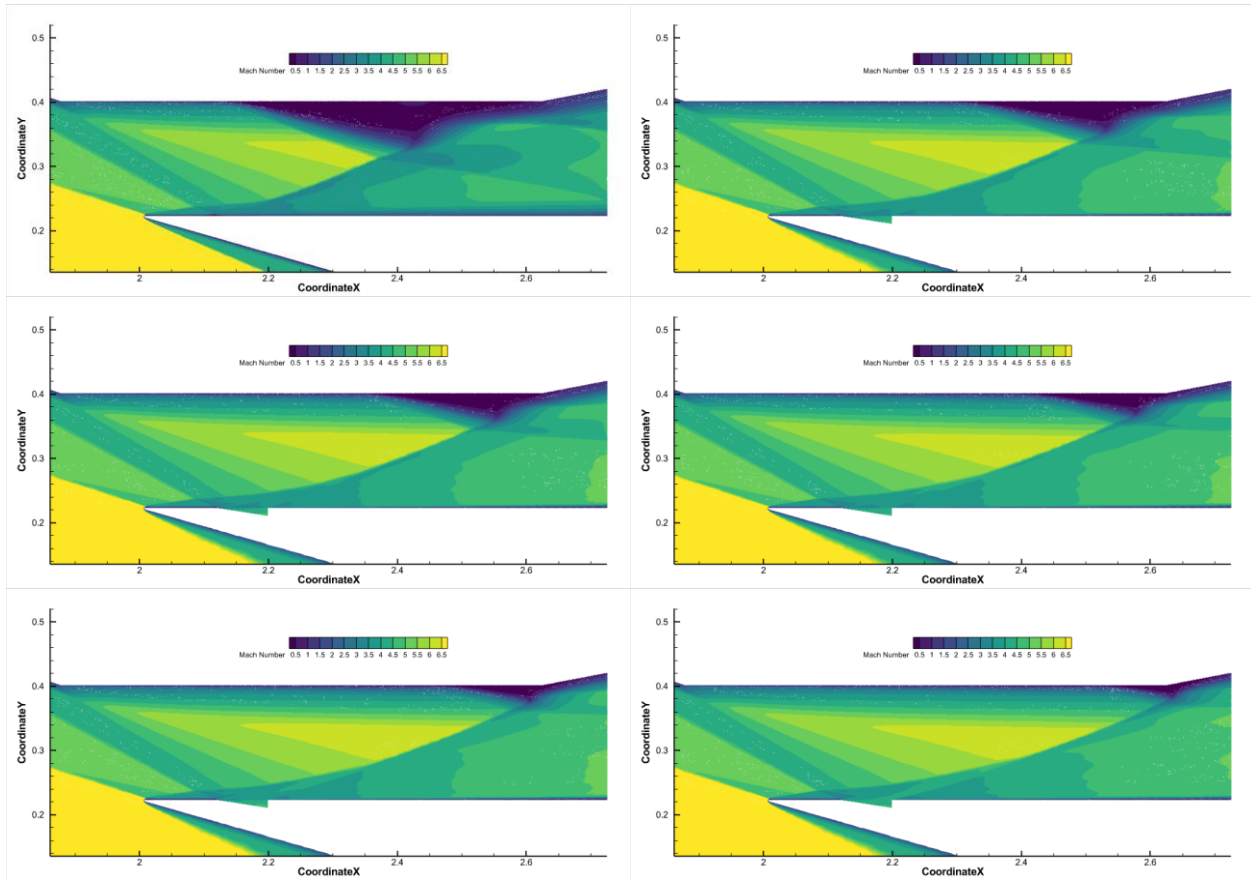


Figure 4.2 The non-dimensionalized bleed rate always increases when angle of attack is increased.

#### 4.2 Isolator Airflow Examination

In Figure 4.3, the Mach contours for the 0 degree angle of attack cases offer a detailed view of the isolator's flow dynamics. Similar results for angles of 2, 4, 6, and 8 degrees can be found in APPENDIX A. As the pressure jump coefficient decreases and more air is vented through the porous boundary, flow stabilization improves, delaying flow separation and reducing the subsonic region. In the C0 case, akin to a pressure outlet condition, the subsonic region nearly vanishes. Various factors contribute to this effect, all stemming from the incorporation of the porous bleeder.



*Figure 4.3* Mach contour in the isolator at 0 degrees angle of attack for all porous cases. Shown are no bleed (top-left), C1000 (top-right), C500 (middle-left), C250 (middle-right), C100 (bottom-left), and C0 (bottom-right). The C values represent the porous bleeder pressure jump coefficient values, described in text.

A significant aspect of the isolator's flow dynamics is the presence of the reflected shock the porous bleeder is placed beneath. Without the bleeder, this shock is more intense and possesses a higher beta value (oblique shock angle), resulting in elevated pressure beyond the shock, as evidenced by lower Mach numbers past the shock in the case without a porous bleeder.

Additionally, the tip of the reflected shock transitions into a normal shock instead of reflecting as an oblique shock upon encountering the high-pressure subsonic region along the upper wall. This phenomenon is accentuated by flow separation and the heightened adverse pressure gradient caused by a stronger reflected shock in cases without bleeding.

Introducing a porous bleeder reduces the effective beta of the reflected shock, as observed in Figure 4.3 by the increased Mach number beyond the reflected oblique shock, resulting in a diminished adverse pressure gradient near the upper wall. The beta angle for the wall case was measured at about 19 degrees, whereas for the C100 case the beta angle was measured at approximately 12 degrees. This 7 degree beta reduction indicates a substantial weakening of the reflected shock. Moreover, bleeding air through the porous boundary reduces the mass flow through the isolator and alleviates the effect of flow choking. As more air is bled out of the bleeder, the adverse pressure gradient decreases and less air has to flow through the gradient, and flow separation diminishes.

Quantitative analysis in Figure 4.4 illustrates the static pressure distribution along the upper wall, highlighting the increased pressure attributed to the subsonic region and the location of flow separation in each case. Notably, even beyond the subsonic region, pressure along the wall remains substantially higher than upstream, indicating that the adverse pressure gradient is responsible for flow separation. In fact, this downstream back pressure contributes to the growth and movement of the subsonic region upstream. Although not immediately evident, this relationship will become clearer when this topic is revisited in Section 4.4 Unstart Prevention.

Lastly, it is hypothesized the introduction of a porous bleeder delays the transition of the boundary layer from laminar to turbulent, slowing its growth rate. If this effect is not occurring, then the bleeder may be “resetting” the boundary layer and reducing the size of the boundary layer by removing the boundary layer air. Though the exact reason or combination of reasons is unknown, the thinning of the boundary layer is evident in Figure 4.3, where the boundary layer in the case without the porous bleeder is visible but becomes significantly thinner after the

implementation of the bleeder. Although a minor effect, reducing the size of the boundary layer increases the average airflow through the isolator.

Figure 4.4 further illustrates that the pressure distribution along the lower wall of the isolator remains unchanged with the introduction of the porous bleeder, except at the bleeder location itself. This is attributed to the minimal alterations in flow dynamics along the lower wall, where the boundary layer, albeit thinner, maintains a consistent pressure.

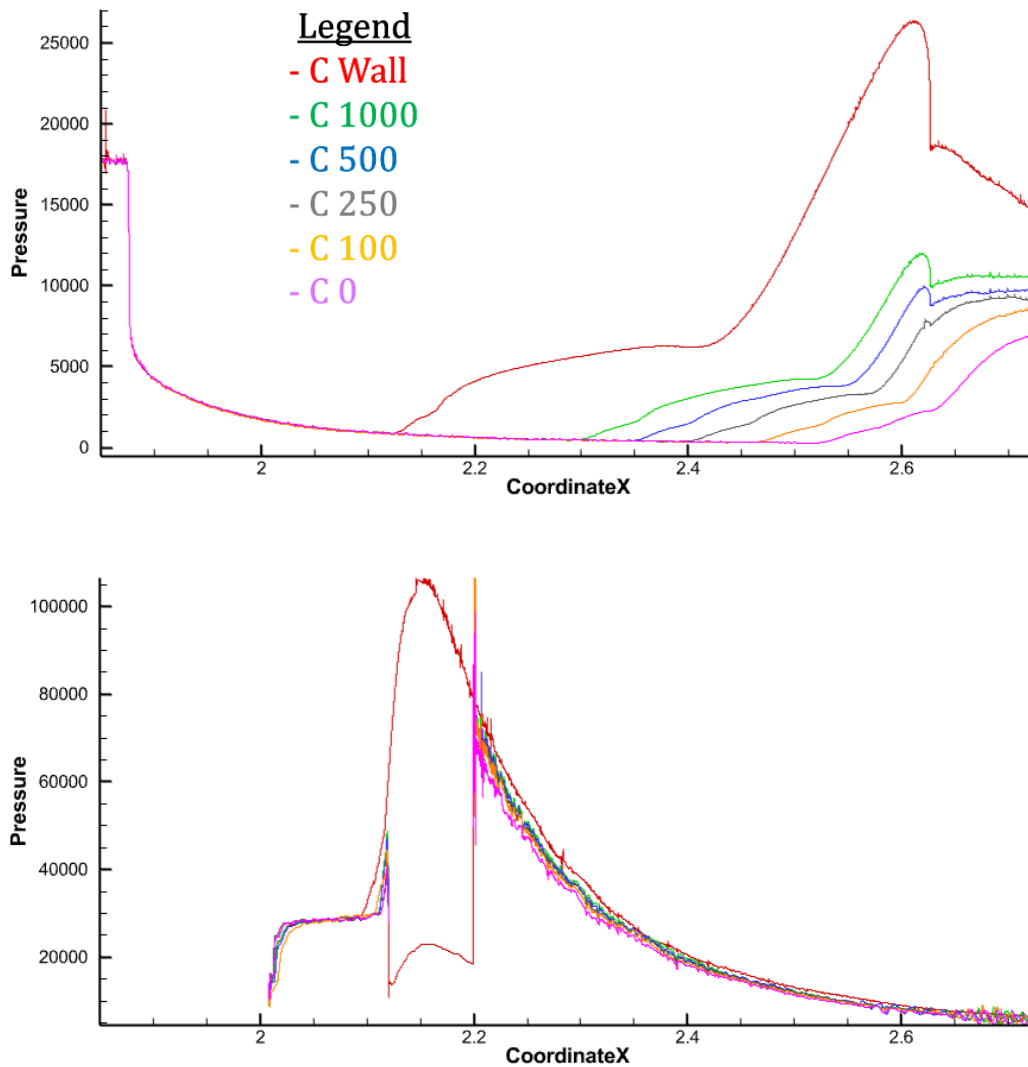


Figure 4.4 Static pressure distribution comparison along the upper (top) and lower (bottom) wall of the isolator at every pressure jump coefficient value for 0 degrees angle of attack.

### 4.3 Porous Effectiveness Measurement

In order to accurately assess the effectiveness of the isolators with and without porous bleeders, a one-dimensional approach was employed to simplify the flow dynamics. Various methods, such as area-weighted or mass-weighted averages, could have been used for data extraction. However, for increased accuracy, an in-house CMES (conserved mass/energy/entropy) MatLab code was employed. This code, derived from the methodology outlined by Baurle and Gaffney [34], primarily employs mass flux averaged values and entropy changes to compute essential parameters. Additionally, it accommodates variable specific heats, crucial for high-temperature hypersonic flows where a constant specific heat assumption would be inadequate. It should be noted that CMES conserves these values along the cross-section in which it is averaging data, not throughout the airflow, as conserving entropy in that regard would be impossible.

CMES proved particularly valuable in determining total pressure at the inlet and outlet of the isolator. While Fluent provides accurate absolute pressure values, it does not compute total pressure during runtime. Instead, total pressure values are derived during data export, which can result in discrepancies. To validate CMES, a basic test case inducing a normal shock was conducted across various freestream Mach numbers. CMES consistently yielded highly accurate total pressure values, closely matching analytical predictions for both freestream and post-shock conditions at all Mach numbers. In contrast, Fluent's reported total pressure values often deviated by 10-15%. Therefore, CMES was validated and chosen for total pressure recovery measurements.

The total pressure ratio across the compression system is defined as the total pressure at the compressor entrance divided by the freestream total pressure. For subsonic and supersonic engines, it is universally accepted as the standard method of measuring engine compression systems, in this case the inlet/isolator efficiency. In hypersonic engines, the total pressure becomes

complicated as stagnating the flow excites chemical effects [35]. Nevertheless, total pressure recovery is still a useful measurement of compression systems as the loss of stagnation pressure is of fundamental interest [2].

Alternative parameters for assessing compression efficiency, such as dimensionless entropy increase and kinetic energy efficiency, were considered. Kinetic energy efficiency is defined as the ratio of the square of the velocity that the compression component flow would achieve if it were isentropically expanded to freestream static pressure to the square of the freestream velocity [35].

An adaptation of kinetic energy efficiency, proposed in APPENDIX B to gauge efficiency relative to potential thrust outputs, was initially considered for porous bleeder effectiveness assessment. However, it was discarded for two primary reasons. Firstly, as noted by Heiser and Pratt [35], kinetic energy efficiency is very nearly 1, particularly at high freestream Mach numbers. In the Mach 7 case studied, all efficiency values surpassed 99%, rendering distinctions negligible unless studied at the third decimal level. Secondly, an issue arose with the CMES code. While it accurately calculated freestream static and total temperatures, it occasionally generated incorrect temperature values post normal shock in test cases. The cause of this inconsistency remains unclear, as total pressure values remained accurate. Although CMES produced reasonable temperature results for all of the current study's cases, the decision was made to solely rely on validated total pressure values, disregarding other efficiency measurements requiring temperature data.

Figure 4.5 illustrates the total pressure recovery for the "Wall" cases, where the porous bleeder was not employed, across all angles of attack. As anticipated, the total pressure recovery

at both the isolator entrance and exit, relative to freestream total pressure, decreases with increasing angle of attack.

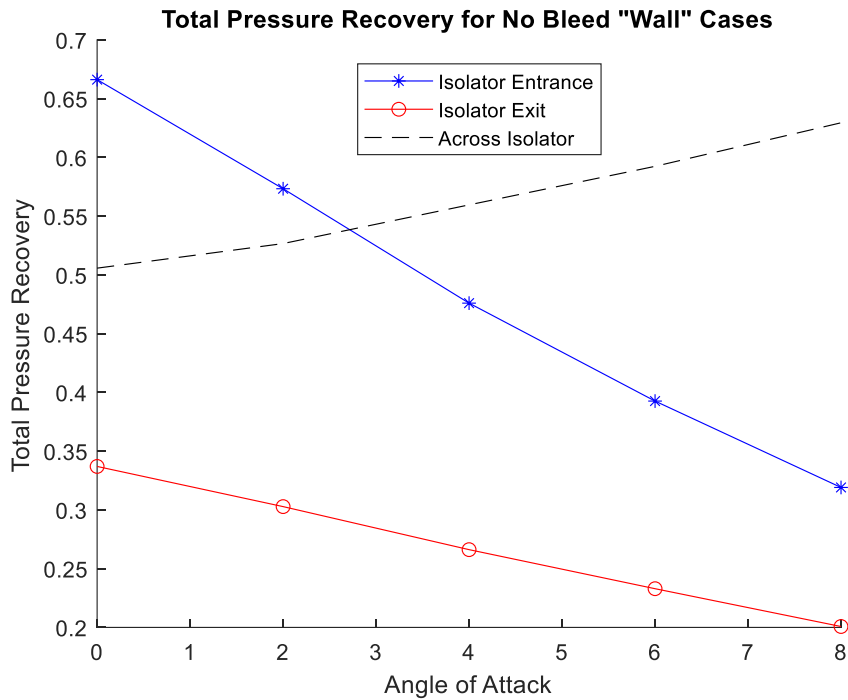


*Figure 4.5* The total pressure at both the isolator entrance and exit decrease with increasing angle of attack, but the ratio between the two increase.

However, the total pressure at the isolator entrance is solely influenced by the external compression system and the angle of attack. As a result, the presence of the porous bleeder within the isolator will not impact the entrance total pressure, as information cannot propagate backward in supersonic scenarios. Hence, a more pertinent metric is to evaluate the total pressure ratio across the isolator by comparing the exit total pressure to the entrance total pressure, as indicated by the dashed line in Figure 4.5. Interestingly, while both entrance and exit total pressures decrease with increasing angle of attack, the entrance total pressure diminishes more rapidly. Therefore, the total pressure recovery ratio across the isolator actually increases as the angle of attack rises. Going

forward, it's essential to consider this distinction; all "total pressure recovery" values will denote the total pressure recovered at the isolator exit relative to the isolator entrance for a given angle of attack, rather than comparing to the freestream.

Introducing the porous bleeder into the isolator immediately shows promise. While the wall cases had a total pressure recovery range from around 0.5 to 0.65, Figure 4.6 shows that the implementation of the porous bleeders has increased the range by 20-30%. Interestingly, despite the observations made about the shrinking subsonic region in the visual results section, the total pressure recovery is not maximized with the unimpeded ( $C_2 = 0$ ) porous bleeder, though it can be seen that gradually increasing the pressure jump coefficient does indeed reduce the total pressure recovery. However, increasing the pressure jump coefficient and reducing the mass flow through the bleeder also increases the mass flow into the combustor, which would lead to better engine performance. Thus, understanding which of these counteracting effects takes precedence is crucial.

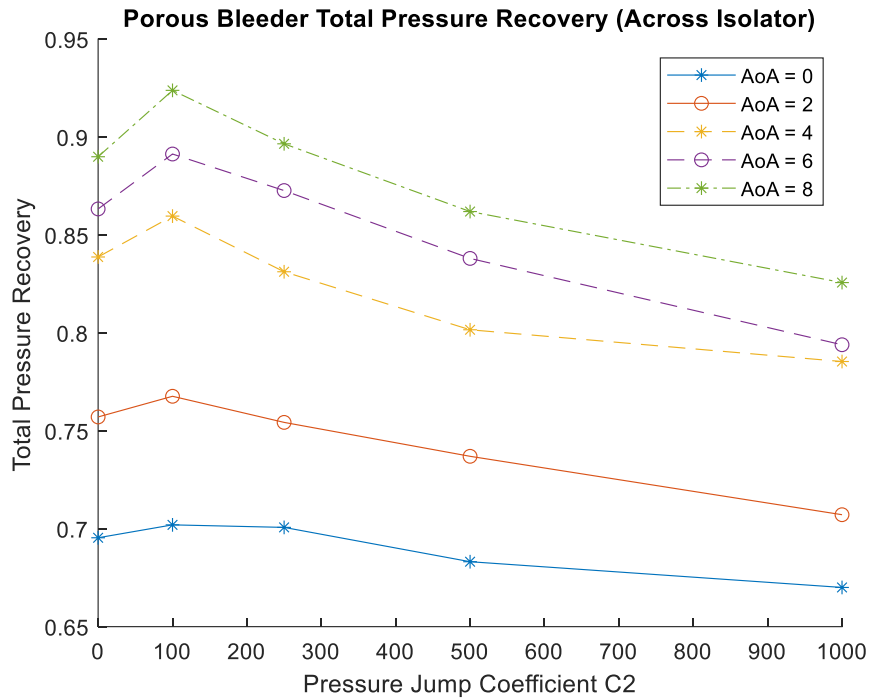


Figure 4.6 The total pressure recovery across the isolator is higher with the addition of a porous bleeder for all cases.

Rearranging the porous bleeder total pressure recovery data in terms of angle of attack yields Figure 4.7, indicating that for all angles of attack, a pressure jump coefficient of 100 returned the highest total pressure recovery. While the pattern of increasing total pressure recovery with decreasing pressure jump coefficient was expected, it was surprising that the unimpeded porous bleeder did not return the highest total pressure recovery.

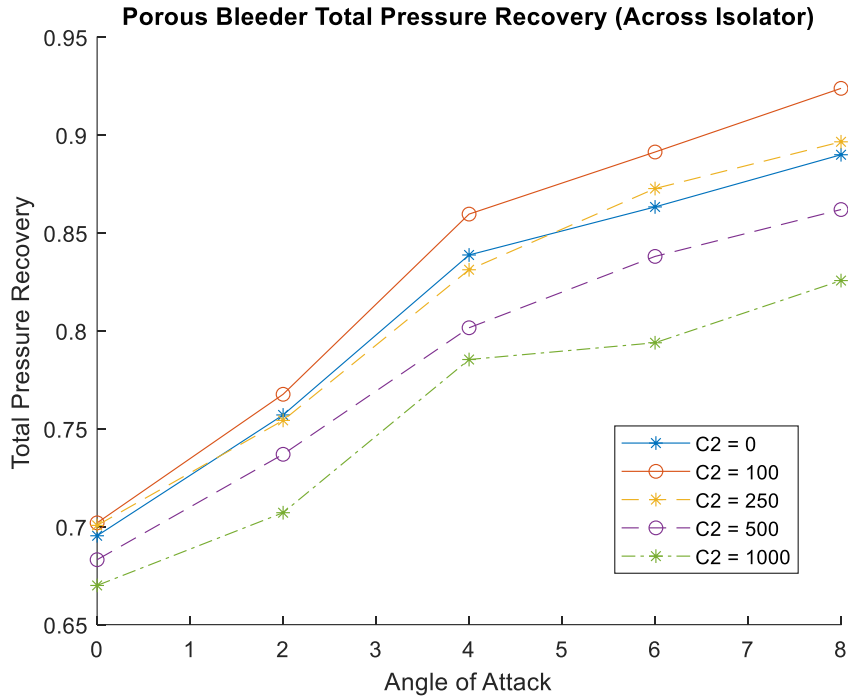


Figure 4.7 Total pressure recovery across the isolator increases with angle of attack, and further increases with decreasing pressure jump coefficient. A notable exception to this pattern is the unimpeded porous bleeder, which did not yield the highest total pressure recovery.

While reducing the pressure jump coefficient to increase airflow through the bleeder enhanced total pressure recovery, it concurrently diminished the mass flow entering the combustor, reducing overall engine performance. Therefore, for a proper assessment of porous bleeder effectiveness relative to cases without a bleeder, the mass flow rate must be factored in. Thus, the total pressure recovery was multiplied by the mass flow percentage entering the combustor (or one minus the mass flow percentage through the bleeder depicted in Figure 4.2), denoting it as the bleeder effectiveness in subsequent analyses. This effectiveness is displayed in Figure 4.8.

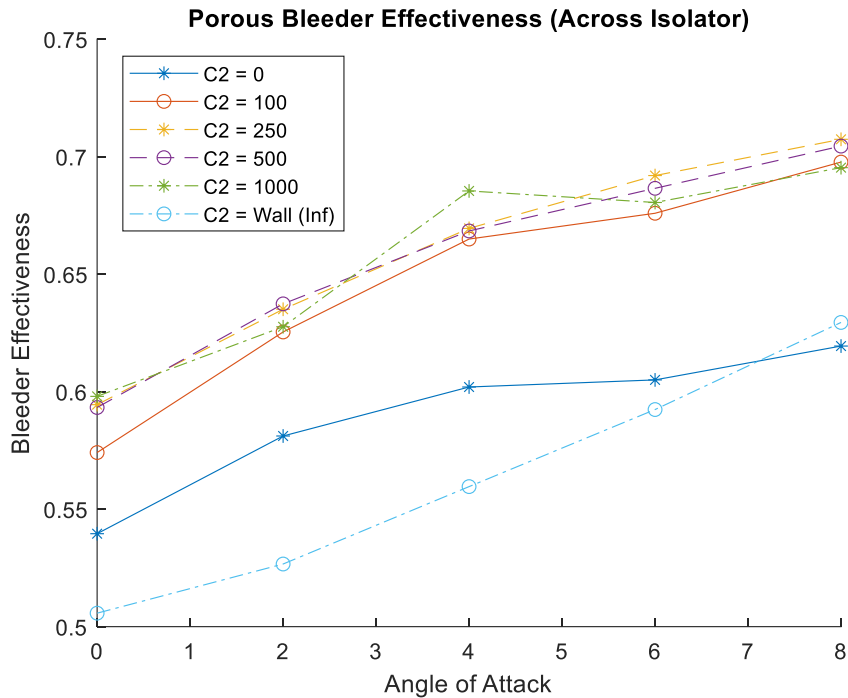


Figure 4.8 Porous bleeder cases showed a higher effectiveness compared to the wall case.

The findings depicted in Figure 4.8 reveal that even when the reduced mass flow rate is factored in, cases featuring porous bleeders consistently demonstrated superior isolator effectiveness compared to the wall case. The unimpeded porous bleeder case, previously not maximizing total pressure recovery, now displays the lowest bleeder effectiveness when mass flow is considered.

Remarkably, the remaining bleeder cases appear to have nearly standardized, as evidenced by their overlapping data points. The exact reasons for this finding are unclear, but the results seem to suggest that, using this metric to measure effectiveness, the individual bleeder settings are less important than their mere inclusion. However, in real world situations it is still likely that a tighter porous bleeder leading to a higher mass flow into the combustor would be more desired as to minimally impact thrust loss, so long as unstart does not occur.

#### 4.4 Unstart Prevention

In addressing the matter of engine unstart mitigation, it's essential to recognize that engine efficiency becomes irrelevant if unstart occurs, leading to engine failure. Surprisingly, none of the tested cases experienced unstart on their own, even under extreme conditions such as a 12 degree angle of attack case, highlighting the robustness of the wedge design. However, in a practical engine scenario, back pressure generated by the combustor could elevate the risk of unstart. To simulate this condition, the mechanical blockage method was employed to introduce increased back pressure. By using a mechanical throat to obstruct varying percentages of the exit area, corresponding to increasing back pressure, the potential of porous bleeder implementation in preventing unstart was tested. These experiments were conducted across different angles of attack (0, 4, and 8 degrees) and pressure jump coefficients (0, 100, and 250), including a non-porous "Wall" case for comparison. The blockage amount was systematically adjusted to obstruct half, two-thirds, and three-quarters of the exit area in the conducted experiments.

In the experimental setup, three distinct outcomes were observed. Only under the half-area blockage condition did the flow remain stable. However, in two cases in the three-quarter-area blockage scenario, full unstart occurred, characterized by the development of a permanent shock in front of the entrance. The most common outcome observed across multiple cases was "oscillatory" unstart, where the flow alternated between entering and exiting the isolator.

This transient phenomenon arises due to excessive back pressure, which impedes the flow of incoming air. Consequently, high-pressure air accumulates at the isolator exit and begins to propagate upstream. In cases without heightened back pressure, the flow stabilizes once the high-pressure region moves sufficiently upstream, as evidenced by the presence of the subsonic region causing flow separation (refer to Figure 4.3).

However, under conditions of excessive back pressure, the high-pressure air continues to accumulate in the combustor and move upstream unabated, as illustrated in Figure 4.9. Once unstart occurs, high-pressure subsonic air accumulates within the isolator and begins moving upstream, contrary to its intended direction. As the unstart wave progresses upstream, it interacts with the porous bleeder, which endeavors to extract as much high-pressure air from the isolator as feasible. This dynamic is illustrated in Figure 4.10.

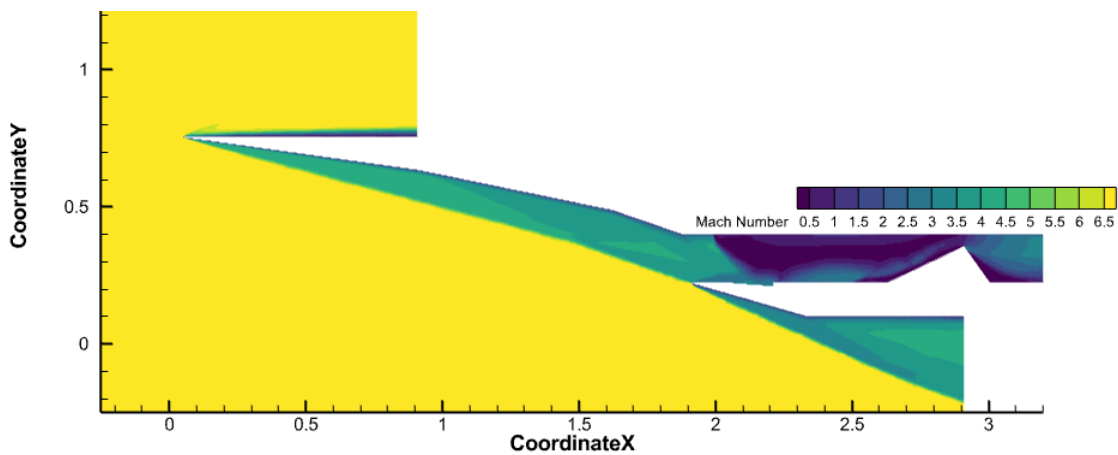


*Figure 4.9* The high pressure region starts along the upper wall of the isolator near the exit, but moves upstream as high pressure air builds up.

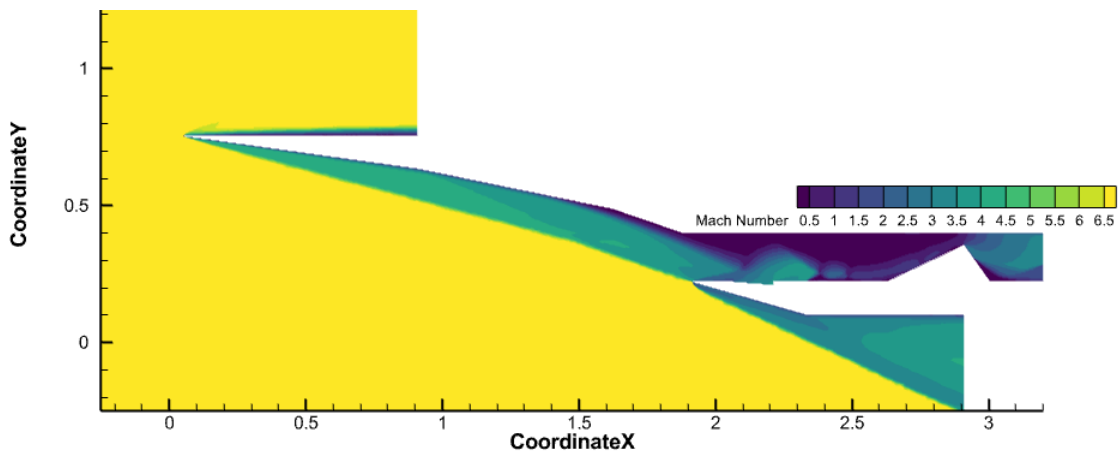


*Figure 4.10* The high pressure unstarting flow has now reached the porous bleeder, which begins to remove the stagnant air. Some flow spillage is visible.

While the porous bleeder aids in extracting stagnant air during unstart, it is insufficient to resolve the excessively high pressure within the isolator during oscillatory unstart scenarios. Figure 4.11 juxtaposes the static pressure distribution along the upper isolator wall during oscillatory unstart, at the same timestep as shown in Figure 4.10, with the static pressure distribution of a steady case for the identical angle of attack and pressure jump coefficient. The pressure in an unstarted case far surpasses that in a steady case, by several orders of magnitude.

Eventually, the high-pressure air reaches the lower cowl lip, leading to flow spillage as depicted in Figure 4.12. In fully unstarted cases, the isolator remains in this state. However, in oscillatory unstart scenarios, the high-pressure air can remove itself from the isolator through flow spillage, allowing air to re-enter the isolator. While the presence of a porous bleeder is not mandatory for this process, it expedites air re-entry by extracting much of the stagnant high-pressure air flooding the isolator. Periods of increased mass flow through the porous bleeder, indicative of this process, are evident in Figure 4.13.

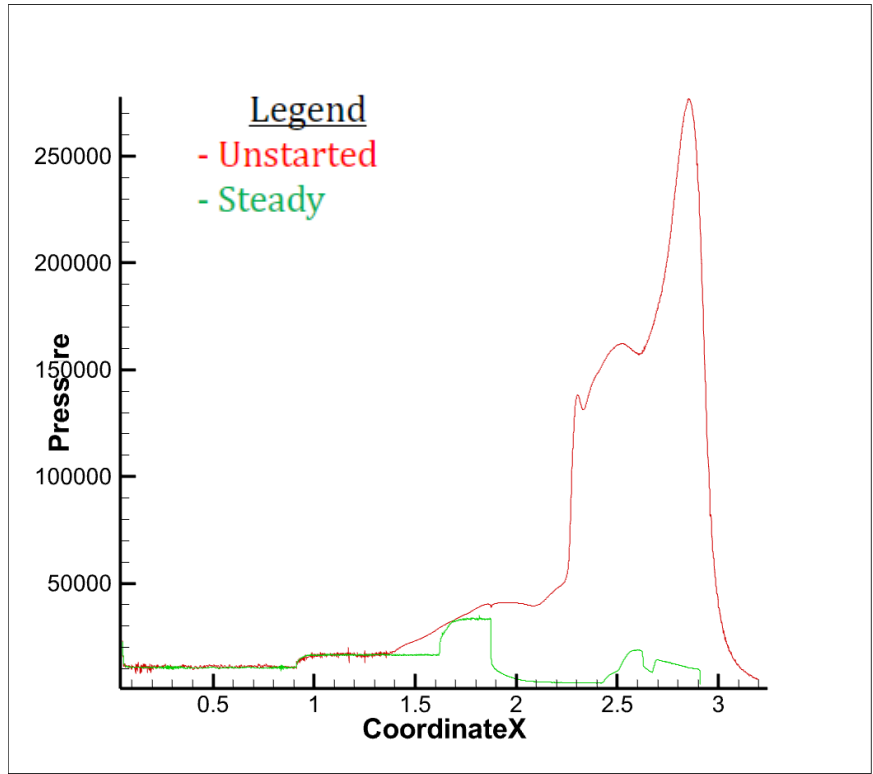


Figure 4.11 The static pressure distribution along the upper isolator wall at 8 degrees angle of attack and a pressure jump coefficient of 0. Displayed is an unstarted case caused by three-quarters blockage compared to the steady case.

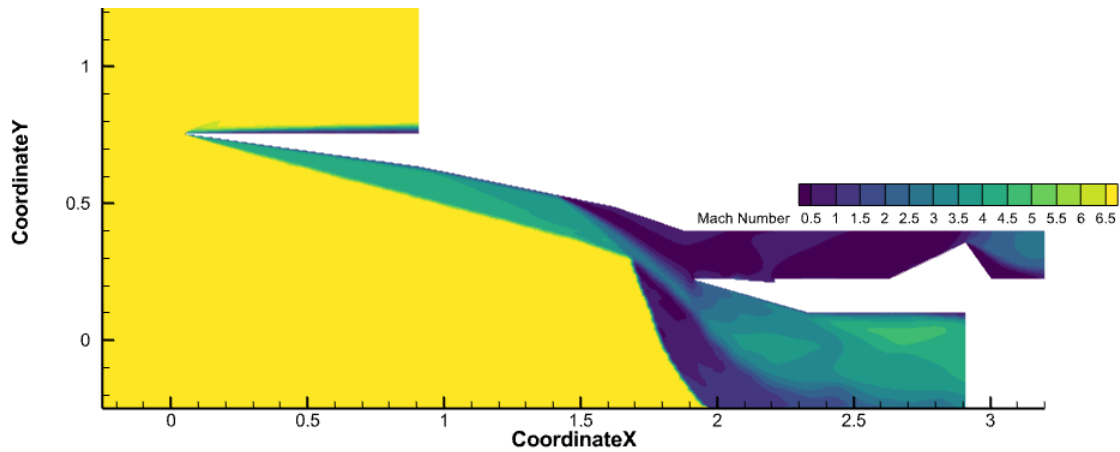
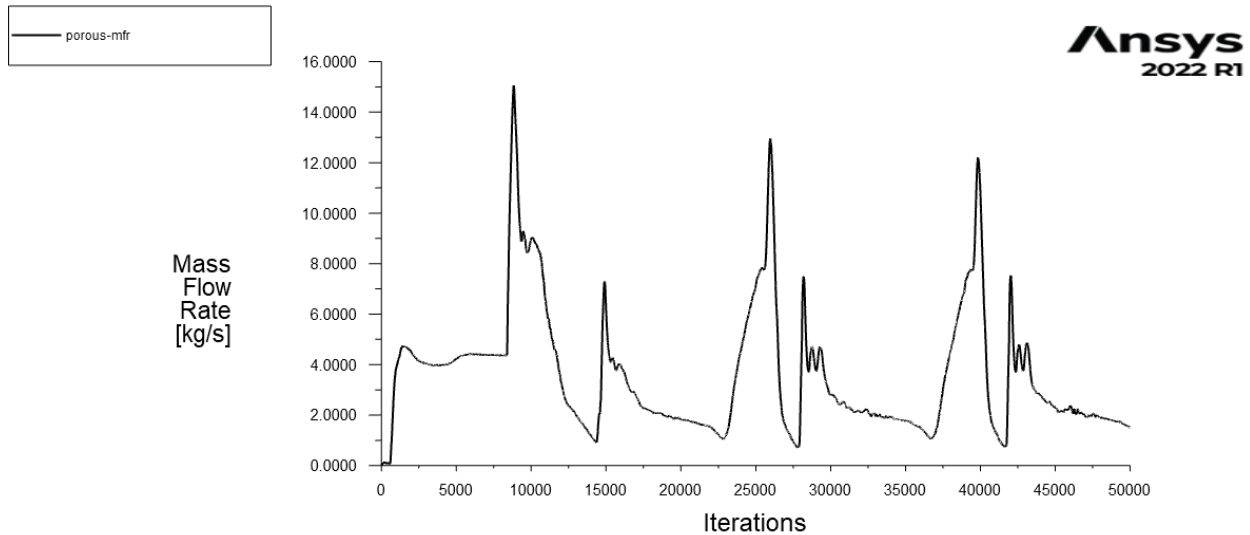


Figure 4.12 Flow spillage has occurred and the inlet is in an unstarted state, but it can be alleviated with the help of a porous bleeder.

The dynamic adjustment to airflow provided by the porous bleeder aids in reverting the unstarted state, albeit temporarily. Without other active adjustments, such as reducing the mass flow into the combustor or decreasing the combustor pressure, the flow will encounter the same issues that initiated unstart, leading to a recurring cycle.



*Figure 4.13* Mass flow rate through a porous bleeder during oscillatory unstart; the increase in mass flow due to high pressure air coming into contact with the porous bleeder are visible.

It was investigated whether these unstarted cases would eventually stabilize or persist in oscillatory behavior. Additional cases were simulated for a significantly higher number of iterations to observe any potential convergence towards steadiness. While Figure 4.13, illustrating the mass flow rate through the porous bleeder, distinctly portrays oscillatory patterns, this cyclic behavior becomes even more apparent in Figure 4.14. This figure displays the mass flow rate through the throat for two cases simulated for 150,000 iterations. Despite some initial iterations resolving the unstarted state, once oscillatory unstart initiates, it persists forever.

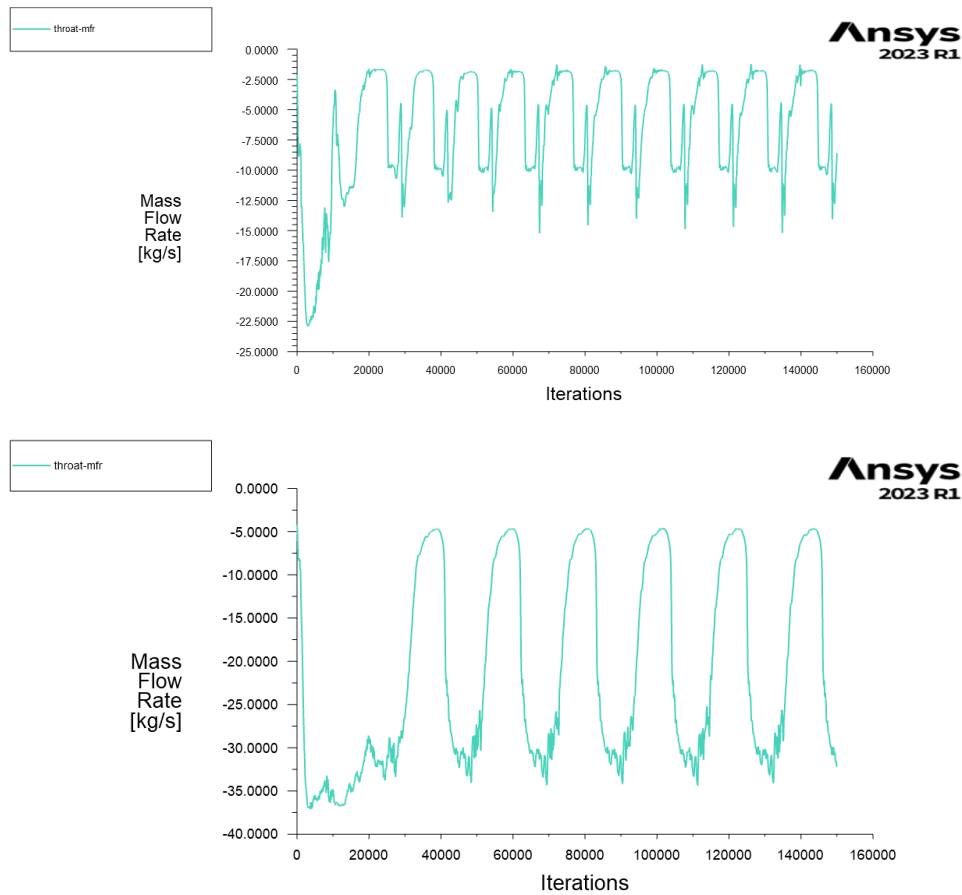


*Figure 4.14* Oscillatory unstart persists for many iterations and has no indication of stabilizing once initiated.

Having investigated oscillatory unstart, the impact of porous bleeders on unstarted cases continues. While the assessment of isolator effectiveness is unfeasible in unstarted scenarios, other metrics such as oscillation period and magnitude can be analyzed. Despite oscillatory unstart being an unstable transient phenomenon and the CFD cases being solved with steady-state solvers, analyzing these aspects might yield usable data. Therefore, the magnitude of the oscillations normalized by the mass flow rate for each angle of attack and the period of the oscillations were recorded for the three-quarter and two-thirds blockage scenarios.

In the examination of the three-quarter area blockage scenario depicted in Figure 4.15, all cases exhibited oscillatory unstart except for two instances: the wall cases at 4 and 8 degrees angles

of attack, both of which experienced full unstart. This suggests that the implementation of a porous bleeder effectively prevented full unstart, as no instances of full unstart occurred with a porous bleeder.

Continuing to the analysis of the period and magnitude of oscillations, although not strictly consistent, there is a general trend of increasing magnitude as the porous bleed amount decreases. The period, however, did not exhibit a clear overall pattern. Notably, the magnitude and period of oscillations for the 0 degree wall case were significantly higher compared to other cases. Given that the wall cases at other angles of attack experienced full unstart in this back pressure scenario, this increase could signal a trend towards potential full unstart.

Furthermore, the presence of a porous bleeder was deemed essential in these cases to dynamically adjust airflow and prevent full unstart. Although oscillatory unstart remains undesirable compared to steady flow, it represents an improvement over full unstart as it indicates the potential of porous bleeders as a remedy for unstarted flow conditions.

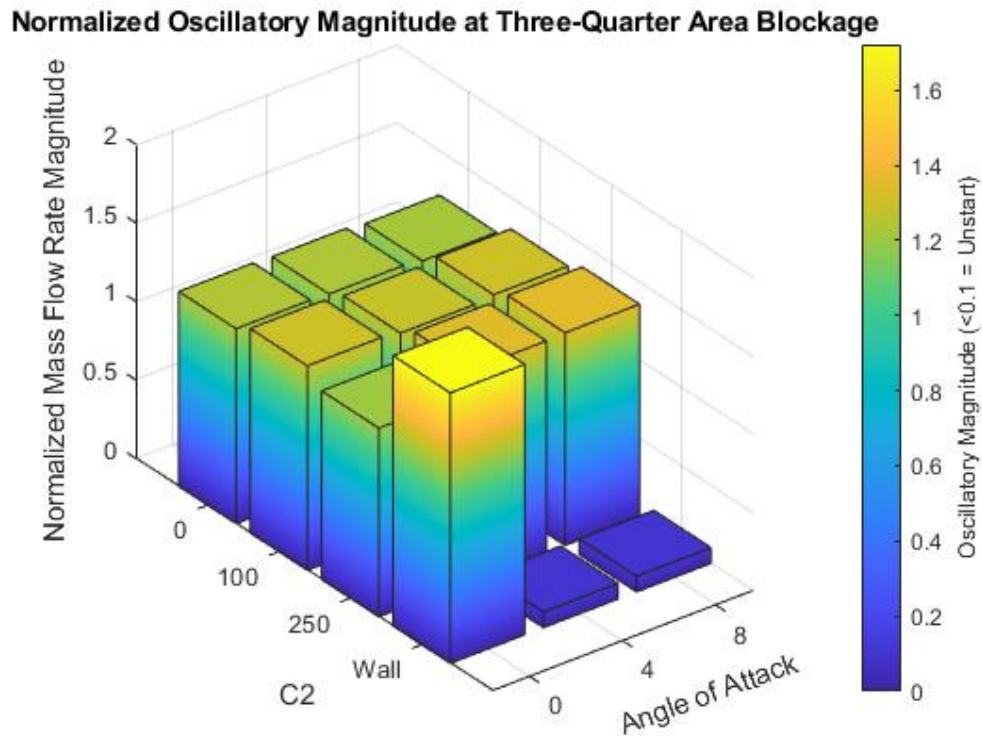
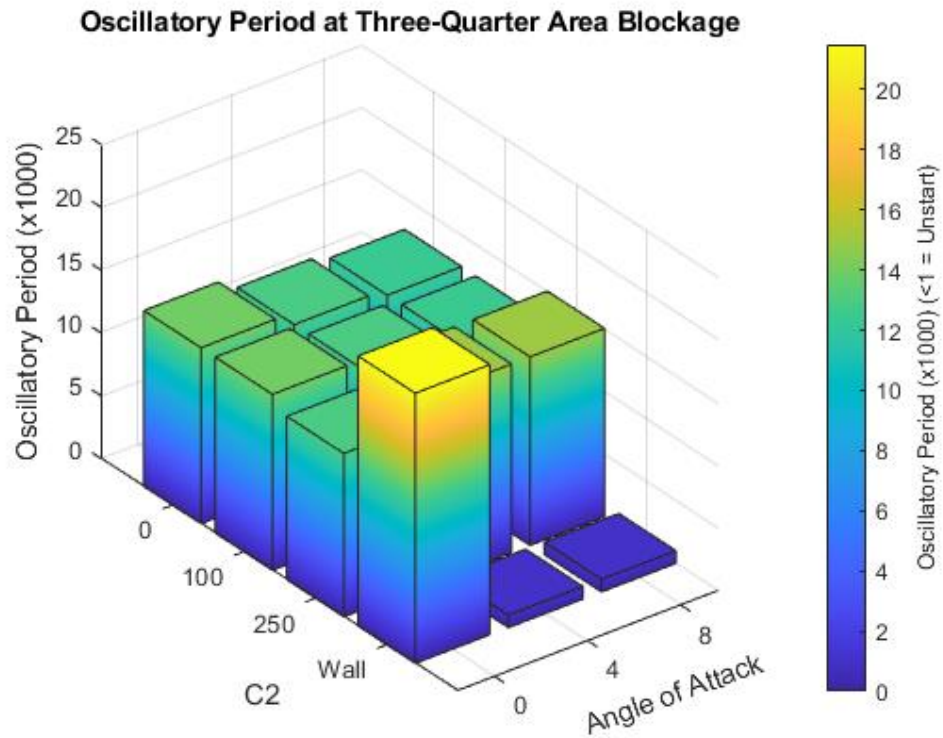


Figure 4.15 Oscillatory period and magnitude for all cases in the three-quarter area blockage back pressure scenario.

Continuing with the analysis of the two-thirds area blockage scenario illustrated in Figure 4.16, all cases manifested oscillatory unstart. As anticipated, the wall cases, lacking a porous bleeder for post-unstart airflow adjustment, exhibited elevated oscillatory periods and magnitudes. Generally, an increase in angle of attack corresponded with heightened period and magnitude, with one exception: the notably higher period observed in the 0 degree wall case remains unexplained.

While the incorporation of a porous bleeder represents an improvement over the wall cases, no consistent discernible distinction was observed among the various bleeder pressure jump coefficient cases in the context of oscillatory unstart.

Lastly, in the half-area blockage scenario, predominantly steady cases were observed, allowing for the use of the metric established earlier to assess porous bleeder effectiveness. As depicted in Figure 4.17, consistent with the findings in Figure 4.8, the unimpeded porous bleeder with a pressure jump coefficient of 0 exhibited reduced effectiveness along with the wall cases. The two porous bleed cases showed increased effectiveness, but as was discovered earlier, it is indiscernible which bleeder was objectively superior.

Notably, however, the 8 degree wall case exhibited oscillatory unstart, contrasting with the steady behavior observed in the porous bleeder cases at 8 degrees for this scenario. While Figure 4.15 highlighted how porous bleeders can rectify fully unstarted flows by actively removing high pressure stagnant air, Figure 4.17 underscores their potential to prevent oscillatory unstart altogether in select cases by reducing mass flow and increasing total pressure entering the combustor.

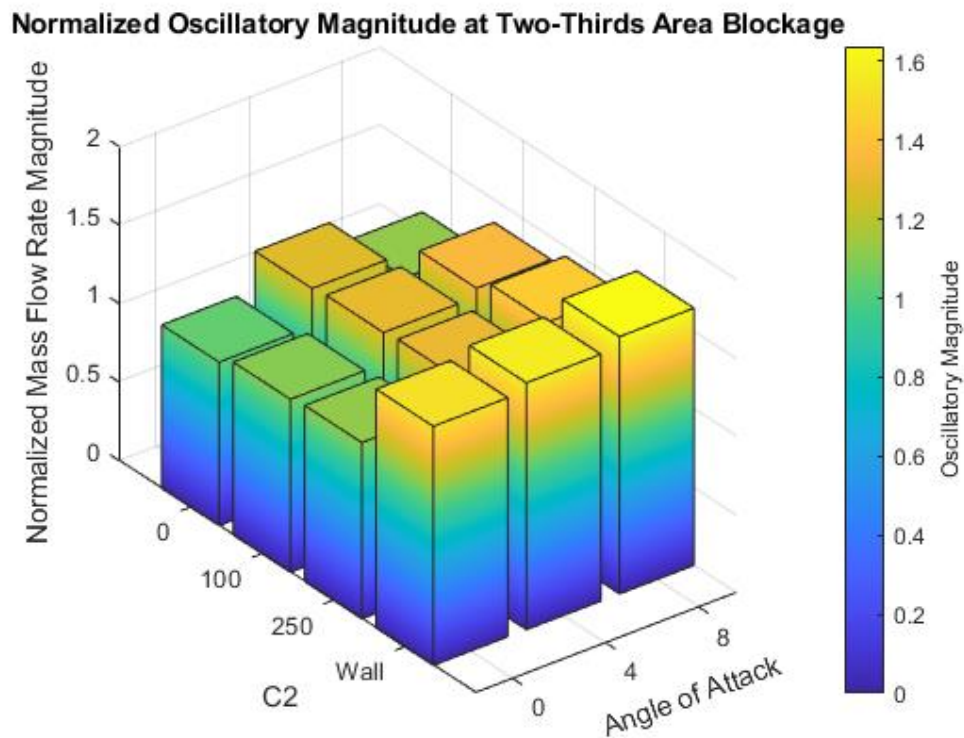
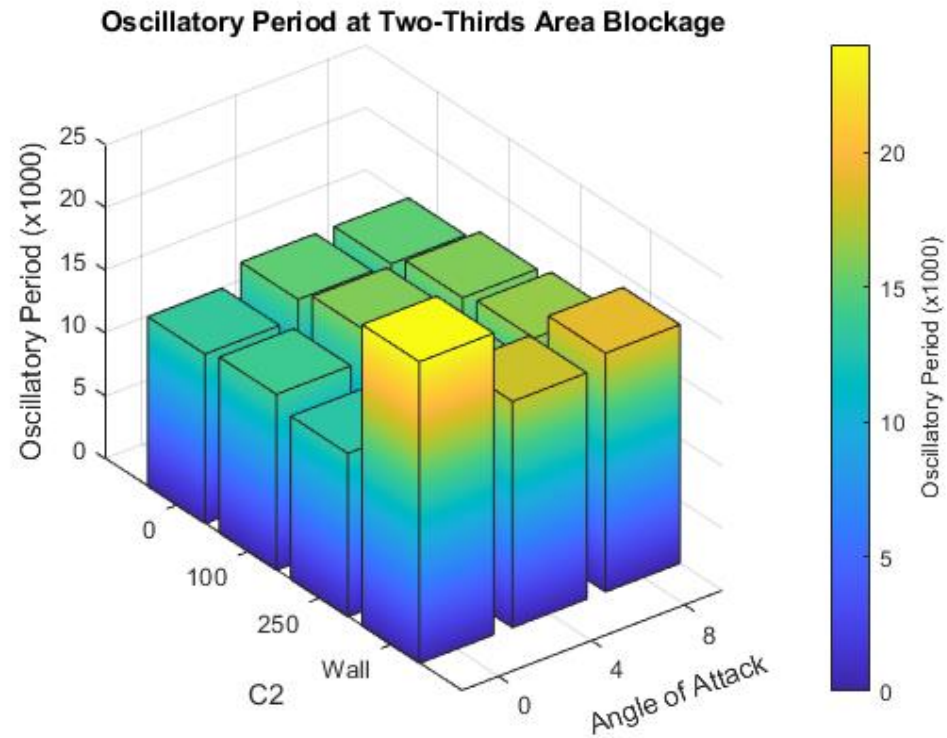
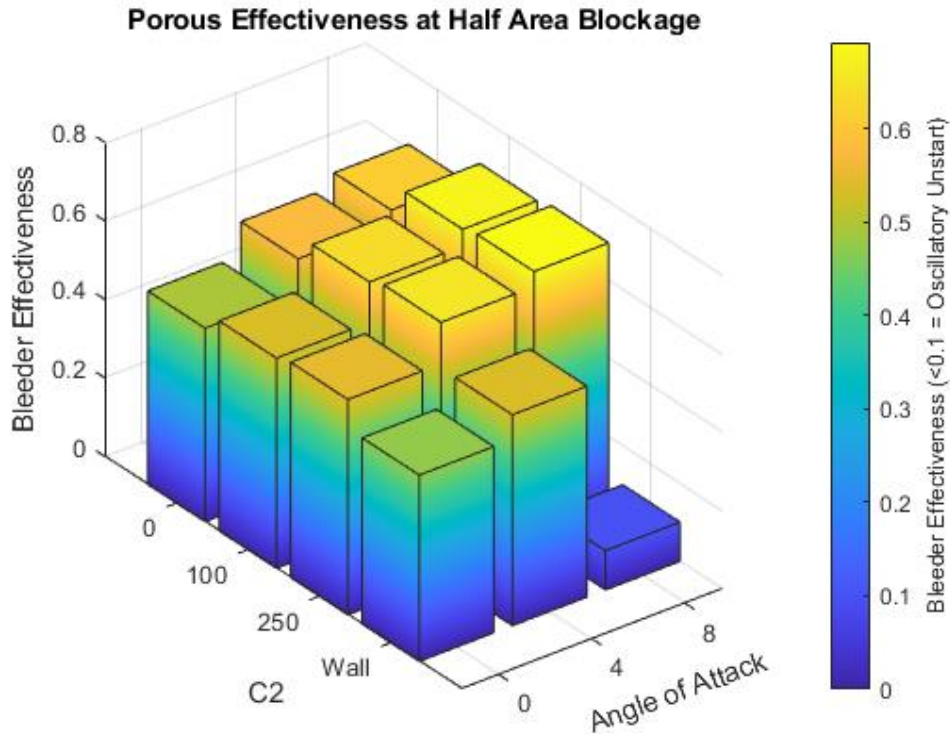


Figure 4.16 Oscillatory period and magnitude for all cases in the two-thirds area blockage back pressure scenario.



*Figure 4.17* Isolator effectiveness for all cases in the half-area blockage back pressure scenario. All cases are stable, except for the wall case at 8 degrees angle of attack.

Figure 4.8 illustrated that once a porous bleeder, excluding the unimpeded variant, is employed, the effectiveness of the remaining porous bleeders tends to stabilize. This observation is reaffirmed in Figure 4.17, where the effectiveness of the porous bleeders with pressure jump coefficient values of 100 and 250 were nearly identical, despite increased back pressure.

Given that the unimpeded porous bleeder essentially functions as a pressure outlet condition, akin to an open vent, these results indicate a well-placed porous bleeder's effectiveness in maintaining optimal isolator airflow compared to both walls and pressure outlets.

## 5 Conclusions and Recommendations

This research investigated the effects of implementing porous bleeders within the isolator of hypersonic scramjets. The study began with the establishment of the airflow dynamics within a control case isolator without bleeders at five angles of attack. Porous bleeders at five different bleed levels were implemented at each angle of attack to study the change in airflow dynamics. Various aspects of porous bleeder implementation were explored, ranging from the determination of optimal bleed conditions to the examination of their effectiveness in preventing unstart.

The results have shown that porous bleeders can indeed influence airflow dynamics within the isolator. By adjusting parameters such as pressure jump coefficient and bleed area, it was possible to increase total pressure recovery and mitigate undesirable effects such as a heightened adverse pressure gradient and the flow separation it caused. Furthermore, the study discovered porous bleeders were capable of actively adjusting airflow post-unstart by removing high pressure stagnant air trapped within the isolator, thus reverting catastrophic failure and ensuring engine operability.

Additionally, by reducing the mass flow into a combustor with heightened back pressure and increasing the total pressure of the airflow, porous bleeders were found to be able to prevent unstart in a case where unstart would have otherwise occurred. The product of the mass flow percentage entering the combustor and the total pressure recovery ratio across the isolator for each of the bleed cases was higher than the wall and unimpeded bleeder, or pressure outlet, cases. However, the effectiveness of the different bleeders measured by this metric seem to not differ from each other at all angles of attack. It is hypothesized that the most optimal bleeder condition, then, would be the one that retains as much mass flow as possible without causing unstart for the scenario the isolator finds itself in.

As bleeder cases displayed a heightened effectiveness compared to pressure outlet cases, a porous bleeder may yield better engine efficiency if implemented instead of an open vent controlled by a movable door. A possible concept to replace movable doors is to have two identical porous bleeder plates layered on top of one another. By adjusting the location of one of the plates relative to the other, bleed rates could be smoothly controlled from no bleed to max bleed. Although a promising idea, further research into this concept is required before implementation can occur, and will likely require transient solvers.

While all cases in this research were solved using steady-state solvers, employing transient solvers would provide a more accurate understanding of the complex and unstable oscillatory unstart phenomenon. Additionally, incorporating a hybrid RANS-LES solver would strengthen result accuracy, as this study solely relied on RANS simulations. Alternatively, using LES or DES solvers in select cases could validate RANS results and ensure precision is maintained.

The geometry selected for this study was chosen for its planar symmetry, allowing for a 2D assumption. However, with the emergence of 3D compression inlets, a realistic 3D case could significantly alter flow dynamics, potentially impacting the effectiveness of porous bleeder implementation.

While computationally demanding, conducting this research ideally would entail a 3D case using a hybrid RANS-LES approach and a transient solver for oscillatory unstart cases, coupled with an improved bleeder condition. Moreover, transient simulations could investigate porous effectiveness under dynamically varying angles of attack, rather than static conditions. Ultimately, advancing research in this area would greatly benefit from time-accurate transient simulations.

## REFERENCES

- [1] Anderson, J. D., Hypersonic and high-temperature gas dynamics, Reston, VA: American Institute of Aeronautics and Astronautics, Inc., 2019.  
<https://doi.org/10.2514/4.105142>
- [2] Curran, E. T., and B., M. S. N., Scramjet Propulsion editors: E.T. Curran and S.N.B. Murthy, Reston: American Institute of Aeronautics and Astronautics, 2000.  
<https://doi.org/10.2514/4.866609>
- [3] Graham, R. H., The complete book of the SR-71 Blackbird: The illustrated profile of every aircraft, crew, and breakthrough of the world's fastest stealth jet, Minneapolis, MN: Zenith Press, 2015.
- [4] McClinton, C., "X-43 - scramjet power breaks the hypersonic barrier: Dryden Lectureship in research for 2006," *44th AIAA Aerospace Sciences Meeting and Exhibit*, Jan. 2006.  
<https://doi.org/10.2514/6.2006-1>
- [5] Urzay, J., "Supersonic combustion in air-breathing propulsion systems for hypersonic flight," *Annual Review of Fluid Mechanics*, vol. 50, Jan. 2018, pp. 593–627.  
<https://doi.org/10.1146/annurev-fluid-122316-045217>
- [6] Rasmussen, M., and Stevens, D., "On Waverider shapes applied to aero-space plane forebody configurations," 5th Applied Aerodynamics Conference, Aug. 1987.  
<https://doi.org/10.2514/6.1987-2550>
- [7] Tuttle, S. G., Carter, C. D., and Hsu, K.-Y., "Particle image velocimetry in a nonreacting and reacting high-speed cavity," *Journal of Propulsion and Power*, vol. 30, Jan. 2014, pp. 576–591.  
<https://doi.org/10.2514/1.b34974>
- [8] Seleznev, R. K., Surzhikov, S. T., and Shang, J. S., "A review of the Scramjet Experimental Data Base," *Progress in Aerospace Sciences*, vol. 106, Apr. 2019, pp. 43–70.  
<https://doi.org/10.1016/j.paerosci.2019.02.001>
- [9] Bornhoft, B. J., Peterson, D. M., Eymann, T. A., Hassan, E. A., Hagenmaier, M., and Baurle, R. A., "Reacting rans simulations of a dual-mode ramjet combustor: A code credibility study," *AIAA Scitech 2020 Forum*, Jan. 2020.  
<https://doi.org/10.2514/6.2020-0651>
- [10] Huebner, L. D., Rock, K. E., Ruf, E. G., Witte, D. W., and Andrews, E. H., "Hyper-X flight engine ground testing for Flight Risk Reduction," *Journal of Spacecraft and Rockets*, vol. 38, Nov. 2001, pp. 844–852.  
<https://doi.org/10.2514/2.3774>

- [11] Fry, R. S., “A century of Ramjet Propulsion Technology evolution,” *Journal of Propulsion and Power*, vol. 20, Jan. 2004, pp. 27–58.  
<https://doi.org/10.2514/1.9178>
- [12] Donohue, J. M., “Dual-mode scramjet flameholding operability measurements,” *Journal of Propulsion and Power*, vol. 30, Apr. 2014, pp. 592–603.  
<https://doi.org/10.2514/1.b35016>
- [13] Im, S., and Do, H., “Unstart phenomena induced by flow choking in scramjet inlet-isolators,” *Progress in Aerospace Sciences*, vol. 97, Feb. 2018, pp. 1–21.  
<https://doi.org/10.1016/j.paerosci.2017.12.001>
- [14] Bao, W., Hu, J., Zong, Y., Yang, Q., Chang, J., Wu, M., and Yu, D., “Ignition characteristics of a liquid-kerosene-fueled scramjet during air throttling combined with a gas generator,” *Journal of Aerospace Engineering*, vol. 27, Sep. 2014.  
[https://doi.org/10.1061/\(asce\)as.1943-5525.0000329](https://doi.org/10.1061/(asce)as.1943-5525.0000329)
- [15] Snider, J., Engblom, W., Vedam, A. J., and Slater, J. W., “Numerical evaluation of hypersonic inward-turning inlets at off-design mach number,” *AIAA SCITECH 2023 Forum*, Jan. 2023.  
<https://doi.org/10.2514/6.2023-0710>
- [16] Drummond, J. P., Bouchez, M., & McClinton, C. R. (2006). Overview of NATO Background on Scramjet Technology.
- [17] McClinton, C. R., Rausch, V. L., Nguyen, L. T., and Sitz, J. R., “Preliminary X-43 flight test results,” *Acta Astronautica*, vol. 57, Jul. 2005, pp. 266–276.  
<https://doi.org/10.1016/j.actaastro.2005.03.060>
- [18] Volland, R. T., Huebner, L. D., and McClinton, C. R., “X-43A Hypersonic Vehicle Technology Development,” *Acta Astronautica*, vol. 59, Jul. 2006, pp. 181–191.  
<https://doi.org/10.1016/j.actaastro.2006.02.021>
- [19] McClinton, C., Hunt, J., Ricketts, R., Reukauf, P., and Peddie, C., “Airbreathing Hypersonic Technology Vision Vehicles and Development Dreams,” *9th International Space Planes and Hypersonic Systems and Technologies Conference*, Aug. 1999.  
<https://doi.org/10.2514/6.1999-4978>
- [20] McClinton, C., Rausch, D., Sitz, J., and Reukauf, P., “Hyper-X program status,” *10th AIAA/NAL-NASDA-ISAS International Space Planes and Hypersonic Systems and Technologies Conference*, Apr. 2001.  
<https://doi.org/10.2514/6.2001-1910>

- [21] McClinton, C. R., Rausch, V. L., Shaw, R. J., Metha, U., and Naftel, C., “Hyper-X: Foundation for future hypersonic launch vehicles,” *Acta Astronautica*, vol. 57, Jul. 2005, pp. 614–622.  
<https://doi.org/10.1016/j.actaastro.2005.03.061>
- [22] Rausch, V. L., McClinton, C. R., Sitz, J., & Reukauf, P. (2000). NASA’s Hyper-X Program.
- [23] Bertin, J. J., and Cummings, R. M., “Critical hypersonic aerothermodynamic phenomena,” *Annual Review of Fluid Mechanics*, vol. 38, Jan. 2006, pp. 129–157.  
<https://doi.org/10.1146/annurev.fluid.38.050304.092041>
- [24] Khankhasaeva, Y. V., Borisov, V. E., and Lutsky, A. E., “Influence of energy input on the flow past hypersonic aircraft X-43,” *Journal of Physics: Conference Series*, vol. 815, Feb. 2017, p. 012018.  
<https://doi.org/10.1088/1742-6596/815/1/012018>
- [25] Kazmar, R., “Airbreathing hypersonic propulsion at Pratt & Whitney - Overview,” *AIAA/CIRA 13th International Space Planes and Hypersonics Systems and Technologies Conference*, May 2005.  
<https://doi.org/10.2514/6.2005-3256>
- [26] Berry, S. A., Auslender, A. H., Dilley, A. D., and Calleja, J. F., “Hypersonic boundary-layer trip development for hyper-X,” *Journal of Spacecraft and Rockets*, vol. 38, Nov. 2001, pp. 853–864.  
<https://doi.org/10.2514/2.3775>
- [27] Kotov, M. A., Ruleva, L. B., Solodovnikov, S. I., and Surzhikov, S. T., “Preliminary experimental assessment of supersonic airflow behavior over ExoMars and X-43 inlet models using multiple flow regime shock tube,” *Journal of Physics: Conference Series*, vol. 1009, Apr. 2018, p. 012038.  
<https://doi.org/10.1088/1742-6596/1009/1/012038>
- [28] Kotov, M. A., Kryukov, I. A., Ruleva, L. B., & Solodovnikov, S. I. (2017). The Investigation of Shock-Wave Interaction with Aerodynamic Models. 55th AIAA Aerospace Sciences Meeting.  
<https://doi.org/10.2514/6.2017-0262>
- [29] Slater, J., “Improvements in modeling 90-degree bleed holes for supersonic inlets,” 47th AIAA Aerospace Sciences Meeting including The New Horizons Forum and Aerospace Exposition, Jan. 2009.  
<https://doi.org/10.2514/6.2009-710>
- [30] Autodesk. (2024, February 27). Autodesk. <https://www.autodesk.com/>

- [31] Pointwise for computational fluid dynamics meshing. (n.d.). [https://www.cadence.com/en\\_US/home/tools/system-analysis/computational-fluid-dynamics/pointwise.html](https://www.cadence.com/en_US/home/tools/system-analysis/computational-fluid-dynamics/pointwise.html)
- [32] Ansys fluent | Fluid Simulation Software. Ansys Fluent. (n.d.). <https://www.ansys.com/products/fluids/ansys-fluent>
- [33] Converge CFD Software. Convergent Science Press. (n.d.). <https://convergecf.com/>
- [34] Baurle, R. A., and Gaffney, R. L., “Extraction of one-dimensional flow properties from multidimensional data sets,” *Journal of Propulsion and Power*, vol. 24, Jul. 2008, pp. 704–714.  
<https://doi.org/10.2514/1.32074>
- [35] Heiser, W. H., and Pratt, D. T., *Hypersonic airbreathing propulsion*, Washington, D.C.: American Institute of Aeronautics and Astronautics, 1994.  
<https://doi.org/10.2514/4.470356>

## APPENDIX A – Additional Porous Bleed Cases

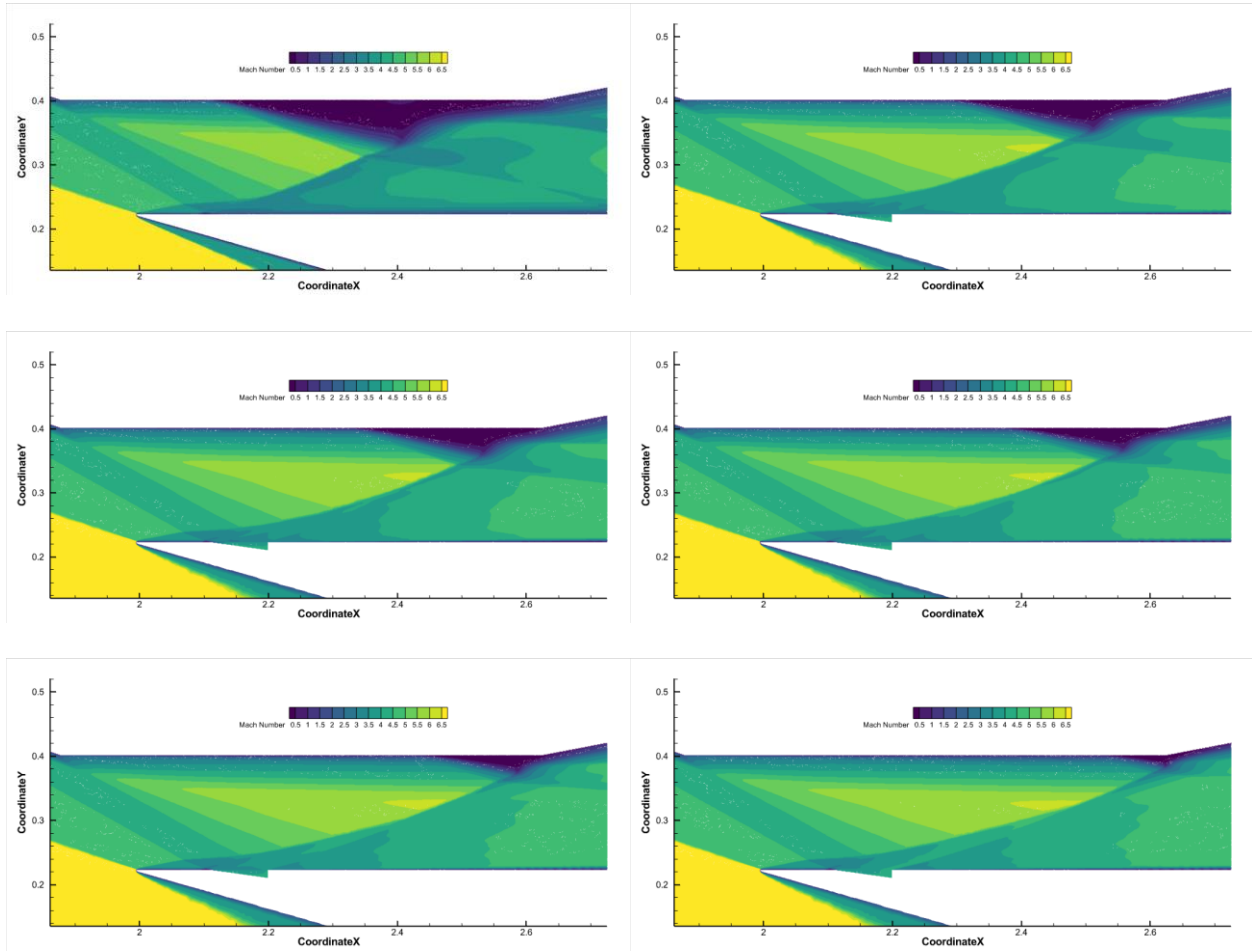


*Figure A.1* Mach contour in the isolator at 2 degrees angle of attack for all porous cases. Shown are no bleed (top-left), C1000 (top-right), C500 (middle-left), C250 (middle-right), C100 (bottom-left), and C0 (bottom-right).

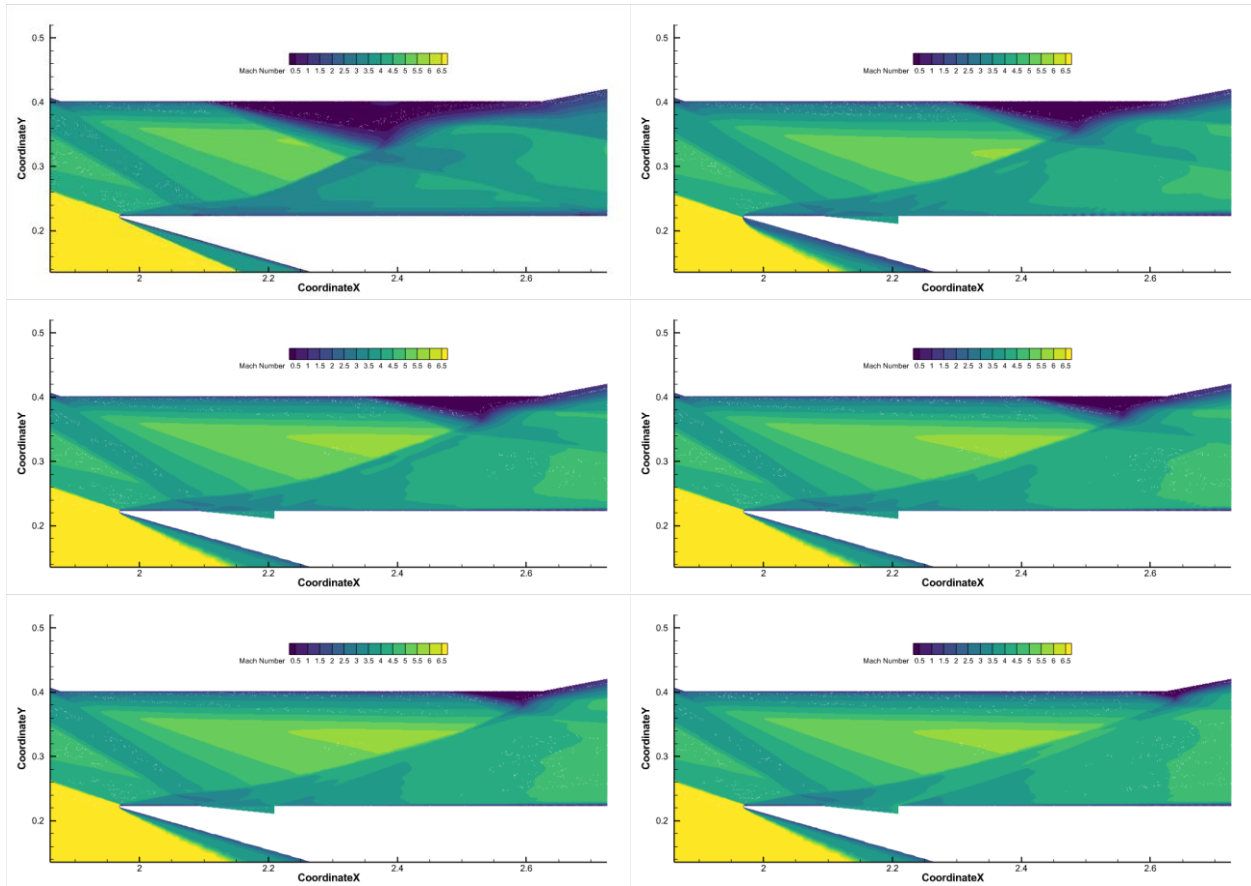


*Figure A.2* Mach contour in the isolator at 4 degrees angle of attack for all porous cases. Shown are no bleed (top-left), C1000 (top-right), C500 (middle-left), C250 (middle-right), C100 (bottom-left), and C0 (bottom-right).

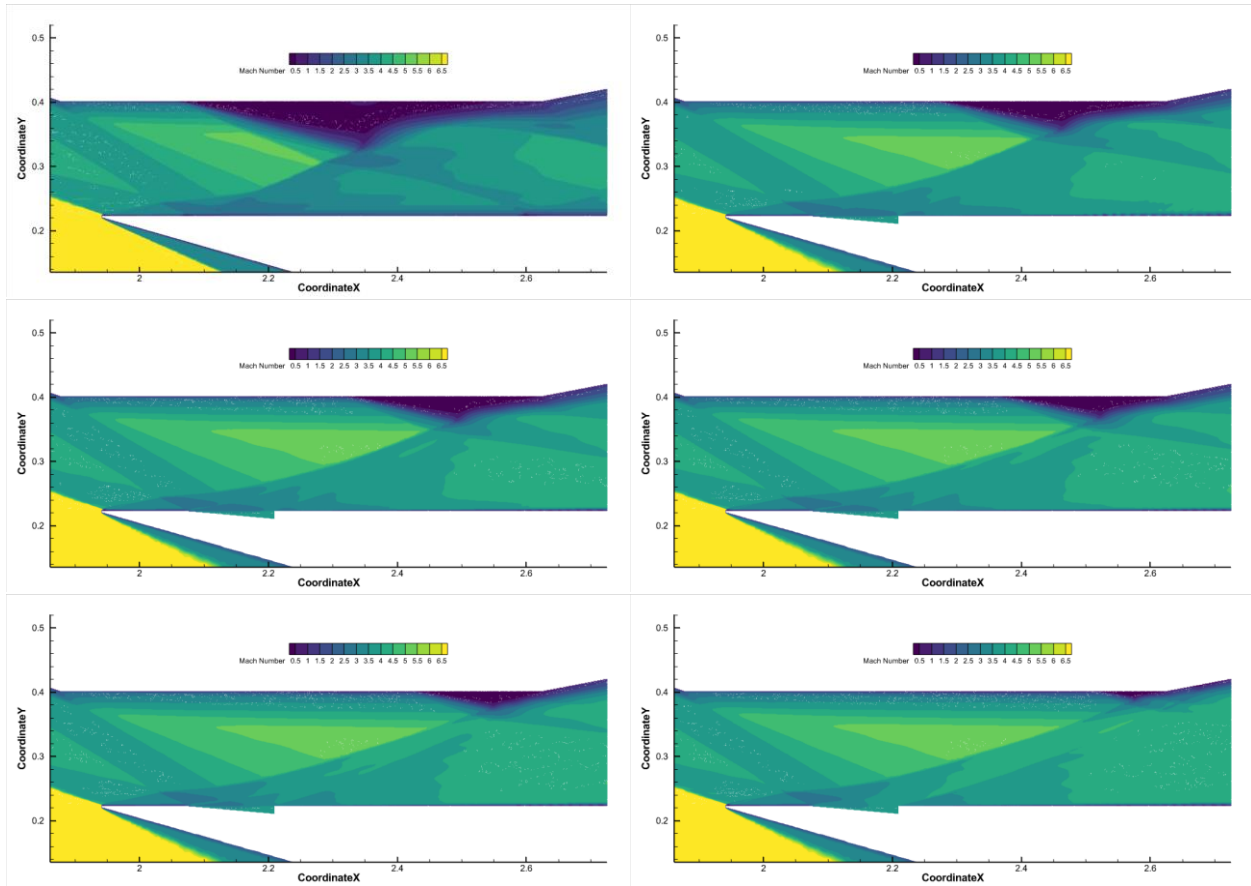


*Figure A.3* Mach contour in the isolator at 6 degrees angle of attack for all porous cases. Shown are no bleed (top-left), C1000 (top-right), C500 (middle-left), C250 (middle-right), C100 (bottom-left), and C0 (bottom-right).

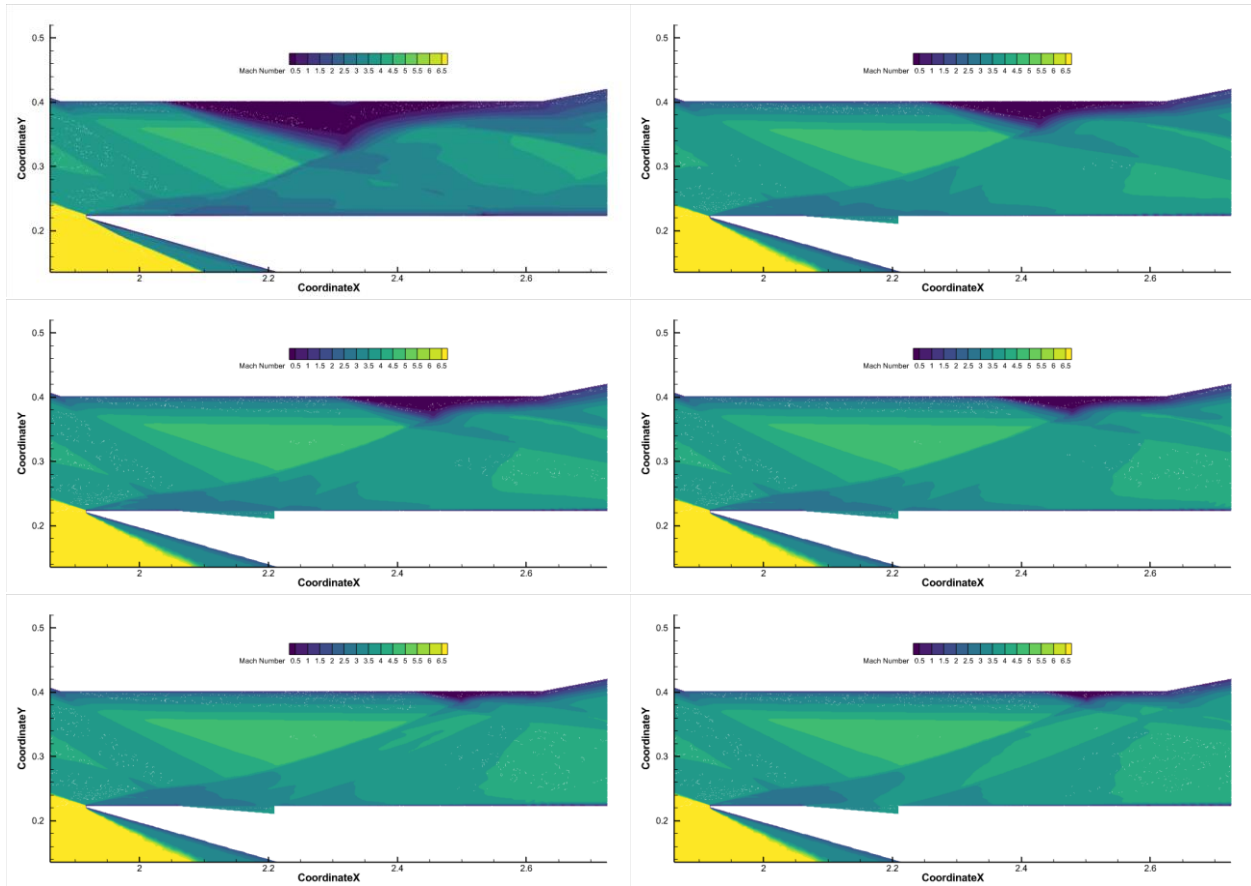


Figure A.4 Mach contour in the isolator at 8 degrees angle of attack for all porous cases. Shown are no bleed (top-left), C1000 (top-right), C500 (middle-left), C250 (middle-right), C100 (bottom-left), and C0 (bottom-right).

## APPENDIX B – Porous Isolator Efficiency Derivation

Start from isentropic equations and the Mach number equation, then rewrite to find velocity in terms of pressure ratio, where  $P_0$  is total pressure,  $P_s$  is static pressure,  $T_0$  is total temperature,  $T_s$  is static temperature,  $M$  is mach number,  $v$  is velocity, and  $\gamma$  is the specific heat ratio, in this case considered to be constant.

$$\frac{P_0}{P_s} = \left(1 + \frac{\gamma - 1}{2} M^2\right)^{\frac{\gamma}{\gamma - 1}} \quad (\text{A.1})$$

$$M = v / \sqrt{\gamma R T_s} \quad (\text{A.2})$$

$$\frac{P_0^{\frac{\gamma - 1}{\gamma}}}{P_s} - 1 = \frac{\gamma - 1}{2} \frac{v^2}{\gamma R T_s} \quad (\text{A.3})$$

$$\left[ \frac{P_0^{\frac{\gamma - 1}{\gamma}}}{P_s} - 1 \right] \left( \frac{2\gamma R T_s}{\gamma - 1} \right) = v^2 \quad (\text{A.4})$$

$$v = \sqrt{\left[ \frac{P_0^{\frac{\gamma - 1}{\gamma}}}{P_s} - 1 \right] \left( \frac{2\gamma R T_s}{\gamma - 1} \right)} \quad (\text{A.5})$$

This velocity denotes the theoretical maximum exit velocity at an ideally expanded, isentropic exhaust if the total pressure were maintained (since static pressure will equal ambient pressure and remain constant). Next, find static temperature in terms of total temperature using isentropic pressure ratio relations.

$$\frac{T_0}{T_s} = 1 + \frac{\gamma - 1}{2} M^2 \quad (\text{A.6})$$

$$\frac{T_0}{T_s} = \frac{P_0^{\frac{\gamma - 1}{\gamma}}}{P_s} \quad (\text{A.7})$$

$$T_s = \frac{T_0}{\frac{P_0}{P_s}^{\frac{\gamma-1}{\gamma}}} \quad (\text{A.8})$$

$$v = \sqrt{\left[ \frac{P_0}{P_s}^{\frac{\gamma-1}{\gamma}} - 1 \right] \left( \frac{2\gamma R}{\gamma-1} \right) \left( \frac{T_0}{\frac{P_0}{P_s}^{\frac{\gamma-1}{\gamma}}} \right)} \quad (\text{A.9})$$

$$v = \sqrt{\left( \frac{2\gamma R}{\gamma-1} \right) \left( T_0 - \frac{T_0}{\frac{P_0}{P_s}^{\frac{\gamma-1}{\gamma}}} \right)} \quad (\text{A.10})$$

Now that the potential exit velocity has been derived in terms of total temperature and total pressure, the ratio between the potential exit velocity using total pressure and temperature at the end of the isolator and beginning of the isolator can be compared. It is important to note that this ratio defines a comparison between two locations within the isolator, and not a comparison versus the freestream total pressure and temperature conditions.

$$\eta_v = \frac{\dot{m}_{out} v_{out}}{\dot{m}_{in} v_{in}} = \frac{\dot{m}_{out}}{\dot{m}_{in}} \frac{\sqrt{\left( \frac{2\gamma R}{\gamma-1} \right) \left( T_{0,out} - \frac{T_{0,out}}{\frac{P_{0,out}}{P_s}^{\frac{\gamma-1}{\gamma}}} \right)}}{\sqrt{\left( \frac{2\gamma R}{\gamma-1} \right) \left( T_{0,in} - \frac{T_{0,in}}{\frac{P_{0,in}}{P_s}^{\frac{\gamma-1}{\gamma}}} \right)}} \quad (\text{A.11})$$

Constant values can be removed and simplified to arrive at a final expression.

$$\eta_v = \frac{\dot{m}_{out}}{\dot{m}_{in}} \frac{\sqrt{T_{0\_out} - \left[ T_{0\_out} / \left( \frac{P_{0\_out}}{P_s} \right)^{\frac{\gamma-1}{\gamma}} \right]}}{\sqrt{T_{0\_in} - \left[ T_{0\_in} / \left( \frac{P_{0\_in}}{P_s} \right)^{\frac{\gamma-1}{\gamma}} \right]}} \quad (\text{A.12})$$